Numerical and Experimental Investigation of the Disintegration of Polymer Melts in an Ultrasonic Standing Wave Atomizer

Von der Fakultät für Naturwissenschaften
der Universität Paderborn
zur Erlangung des Grades eines
Doktors der Naturwissenschaften

-Dr. rer. nat.-

genehmigte Dissertation

von
Nils Lessmann
aus
Lage/Lippe

Paderborn, Dezember 2004

Die vorliegende Arbeit wurde in der Zeit von April 2002 bis Oktober 2004 im Fachgebiet Technische Chemie und Chemische Verfahrenstechnik des Department Chemie der Universität Paderborn angefertigt.

Referent:	Prof. Dr.-Ing. H.-J. Warnecke Universität Paderborn Fakultät für Naturwissenschaften - Department Chemie Fachgebiet für Technische Chemie und Chemische Verfahrenstechnik
Korreferent:	HD Dr. rer. nat. D. Bothe Universität Paderborn Fakultät für Naturwissenschaften - Department Chemie Fachgebiet für Technische Chemie und Chemische Verfahrenstechnik

Datum der Abgabe:	11. Oktober 2004
Datum der mündlichen Prüfung:	17. Dezember 2004

The following work was performed at the Faculty of Natural Sciences in the Department of Chemistry, Chemical Engineering, at the University of Paderborn during my post-graduate studies in the research group *Computational Fluid Dynamics* as part of the Chemical Engineering Division.

During this time the following papers and publications have been published:

Lessmann, N., Bothe, D. & Warnecke, H.-J. 2003 Modelling and simulation of the disintegration process in an ultrasonic standing wave atomizer. *2nd Conf. on Computational Fluid and Solid Mechanics, Boston (MIT)*, Compilation of abstracts p. 125.

Lessmann, N., Bothe, D. & Warnecke, H.-J. 2003 Modellierung und Simulation des Zerstäubungsprozesses in einem Ultraschall-Stehwellenfeld. *Meeting of the GVC-Technical Committee "Mehrphasenströmungen"*, March 5-7, Baden-Baden.

Lessmann, N., Bothe, D. & Warnecke, H.-J. 2003 Disintegration of polymer melts in ultrasonic standing wave fields: process modelling and computation of particle size distribution. *In Proc. of 4th European Congress in Chemical Engineering*, ECCE 9.2-0047.

Bothe, D., Lessmann, N., Reipschläger, O. & Warnecke, H.-J. 2004 Numerical and experimental investigation of the disintegration of polymer melts in an ultrasonic standing wave. *J. of Fluid Mech.* (under consideration for publication).

At this point I like to thank all those people who supported me during the last couple of years morally as well as technically and, therefore, had a strong influence to let this work succeed.

I especially like to express my gratitude to the following people:

Prof. Dr.-Ing. H.-J. Warnecke, for serving as my advisor, providing me with this challenging subject and his confidence in me which gave me the opportunity to freely put this thesis into practice,

HD Dr. rer. nat. D. Bothe, for his willingness to serve as my co-adviser and especially for his valuable support in solving numerical problems and the development of the mathematical model,

Dipl.-Math. Kerstin Wielage, for her support according *FS3D*, her friendly and consistent help about all problems concerning the computer cluster, and the useful suggestions derived in endless talks,

the *Ministerium für Schule, Wissenschaft und Forschung* (MSWF) of the country of Nordrhein-Westfalen within the scope of the research network program VerMoS for their financial support,

Prof. Dr. B. Weigand and Dr. M. Rieber from Stuttgart University for the original VOF-code on which these developments are based,

the Paderborn Center for Parallel Computing (PC^2) for the provided computational time,

and all of my scientific, technical, and administrative co-workers at the chemical engineering department for their assistance and the great working atmosphere who participated in letting this thesis succeed.

My family

"A high level of education is proved
by the ability to explain complicated
matters in a simple way."
Georg Bernhard Shaw (1856-1950)

Contents

Nomenclature

Latin Symbols

Symbol	Dimension	Denotation
A	[m^2]	area
A	[Pa]	sound field amplitude
c	[m/s]	velocity of sound
c_p	[J/kg K]	specific heat capacity (at const. pressure)
c_v	[J/kg K]	specific heat capacity (at const. volume)
C	[m]	curve
D	[1/s]	rate of deformation
D	[m]	sonotrode diameter
d	[m]	diameter
d_{32}	[m]	Sauter diameter
d_{RRSB}	[m]	diameter according to Rosin & Rammler (1933)
$d_{v.0.5}$	[μm]	volume median diameter
$d_{50,\dot{3}}$	[μm]	mass median diameter
F	[m]	focal length
f	[-]	volume fraction
f	[1/s]	frequency
F,f	[N]	force
G	[-]	area
g	[m/s^2]	body forces (e.g., acceleration of gravity)
h	[J/kg]	total enthalpy
h_{st}	[J/kg]	static (thermodynamic) enthalpy
I	[-]	identity tensor
I	[Ns]	momentum
J	[kg/m^2s]	flux
K	[m^2]	lamella parameter
K	[-]	fluid consistency index of viscosity model
L	[m]	length
L_r	[m]	resonant distance

Symbol	Dimension	Denotation
k	[1/m]	wave number
k	[J/m s K]	conductivity coefficient
N_K	[-]	number of pressure nodes
M	[kg/mol]	molar mass
$\mathbf{n}$	[-]	unit normal
n	[-]	flow index of viscosity of model
$\mathbf{P}$	[N/m^2]	momentum flux
p	[N/m^2]	pressure
P	[N/m^2]	characteristic pressure
R	[m]	radius
R	[J/kg K]	gas constant
R_c	[m]	radius of curvature
$R*$	[-]	non-dimensional radius
$\mathbf{s}$	[m]	line element
$\mathbf{S}$	[N/m^2]	viscosity stress tensor
T	[s]	period (time)
T	[K]	temperature
$\mathbf{T}$	[N/m^2]	stress tensor
$\mathbf{u}$	[m/s]	velocity vector
U	[m/s]	characteristic velocity
u, v, w	[m/s]	components of velocity vector
V	[m^3]	volume
X	[m]	sonotrode distance
X_i	[m]	inner sonotrode distance
X_l	[m]	distance of the lamella from the nozzle
$\mathbf{x}$	[m]	position vector
x, y, z	[m]	coordiante of $\mathbf{x} = (x,y,z)$
Y	[m]	oscillation amplitude

Greek Symbols

Symbol	Dimension	Denotation
α	[°]	angle
Γ	[m^2]	interface, phase boundary
λ	[kg/ms]	bulk viscosity
λ	[m]	wave length
μ	[kg/ms]	dynamic viscosity
μ_0	[kg/ms]	dynamic zero shear rate viscosity
ν	[m^2/s]	kinematic viscosity
ρ	[kg/m^3]	density
$\Re$	[-]	real part
σ	[N/m]	surface tension
ω	[1/s]	angular frequency
κ	[1/m]	curvature
κ	[-]	isentropic exponent
ϕ	[-]	value of a quantity
ψ	[-]	physical quantity
χ	[-]	lamella number
δ	[m]	lamella thickness
Ω	[-]	subdomain
$\dot{\gamma}$	[1/s]	shear rate
φ	[-]	velocity potential

Subscripts

$\sim$	deviation from the mean value
$i,\ j,\ k$	cell indices in (x,y,z)-direction
d	droplet / disperse phase
g	gas
l	lamella
max	maximal
n	nozzle
opt	optimal
p	particle
pc	parasite current
r	resonant
rel	relative
s	spherical
st	surface tension
str	strand
t	time

Dimensionless Numbers

Ba	=	$A^2 R_s/(\sigma\rho c^2)$	acoustic Bond number
Ca	=	$\mu\lvert\mathbf{u}\rvert/\sigma$	Capillary number
Fr	=	$U/\sqrt{L\lvert\lvert g\rvert\rvert}$	Froude number
La	=	$\sigma\rho R/\mu^2$	Laplace number
Ma	=	u_{max}/c_0	Mach number
Oh	=	$\mu_d/\sqrt{\sigma\rho_d\, d}$	Ohnesorg number
Re	=	$\rho U\, L/\mu$	Reynolds number
Re_{pc}	=	$\mathrm{u_{pc}} R/\nu$	Reynolds number (Lafaurie *et al.*, 1994)
We	=	$\rho_g u_{rel}^2 d/\sigma$	Gas-Weber number
We_{Lierke}	=	$8p_B/p_\sigma = (\kappa/\sigma)\cdot d_{tr,0}\, P_0\, Ma^2$	Weber number (Lierke, 1998)

Abbreviations

DNS	-	direct numerical simulation
LD	-	laser diffraction
PSD	-	particle size distribution
PSA	-	particle size analyze
rms	-	root mean square
SWA	-	standing wave atomizer
SWL	-	standing wave levitator
SPL	-	sound pressure level
VOF	-	volume of fluid

Summary

Powder coatings are used in many different areas and are gaining increasing importance because of the neglectable emission potential concerning volatile components. The production of powder coatings by disintegration using an ultrasonic standing wave atomizer (SWA) avoids disadvantages of other techniques, but still needs intensification to reach industrial standards.
Therefore, the goal of our research is to achieve a better understanding of the polymer strand disintegration in an ultrasonic wave field. This is done by means of numerical simulations based on continuum mechanical modeling and well-defined experiments for validation. The simulations employ a one-way coupling, where the commercial *Computational Fluid Dynamic*-tools *Fluent* and *CFX*, respectively, are used to compute the nonlinear acoustic field. The calculated acoustic forces are incorporated in the Volume of Fluid-code *FS3D* to compute the disintegration process. These ultrasonic forces acting on the liquid's surface are modeled as appropriate momentum fluxes, approximating the real gas-liquid jump conditions. The model is validated by comparing droplet breakup in levitator experiments and numerical simulations of the atomization process.

The simulations allow a qualitative description of droplet deformation and atomization in a single axis standing wave levitator (SWL). Taking into account back-effects of a droplet on the ultrasonic field, quantitative predictions of droplet radii with respect to sonotrode amplitude are possible, mirroring the real behavior very well. Because of the much higher complexity, numerical simulation of liquid strand disintegration in an SWA cannot take into account effects of the liquid phase on the ultrasonic field. Therefore, so far simulations only allow for a qualitative description of the disintegration process. Nevertheless, significant trends in strand disintegration can be observed as it is demonstrated by particle size distributions. The latter are important for industrial use, reflecting the correlation between variations in operational parameters, material properties, and particle sizes. Therefore, based on these results optimizations of our laboratory plant and the process itself are now possible.

1. Introduction

Polymer particles with size distributions in the range of 5 to 50 μm are gaining increasing importance in industrial production processes and technological applications. Huge amounts of such particles are required in powder coating technology due to more rigid environmental standards. Powder coatings as a solvent-free alternative with almost no thinner emission exceed other types of coatings in terms of conservation. Additional applications include the production of pigments or toners. So far, the production of powder coatings is done by energy-costly milling of polymers, which leads to sharp-edged particles of irregular shape. This reduces product quality and thus, has a negative environmental effect. Therefore, new innovative production methods have to be developed. However, the industrial development of new markets and applications for powder coatings strongly depends on the properties of the polymer particles as well as their manufacturing process. The properties and quality of powder coatings are not only given by their chemical formation, but also depend on particle shape and particle size distribution, hence, on the manufacturing technique. Especially fine properties are found for coatings made of spherical particles with narrow particle size distribution.

A novel advantageous technique for the production of polymer particles is the disintegration of polymer melts in an ultrasonic standing wave atomizer (SWA). Here, particles are created by means of ultrasonic forces acting on the liquid surface and leading to its disintegration. For this purpose, an ultrasonic standing wave field is generated by two sonotrodes, driven by piezo ceramic, with frequencies of about 20 kHz. To improve this system, a booster is placed between transducer and a sonotrode. Thereby, amplitudes of up to 125 μm are generated at the sonotrode's end face. The distance between the transducers is adjusted to an odd multiple of half the acoustic wave length to achieve resonance with usually three or five pressure nodes. Due to resonance phenomena, amplitudes of the resulting velocity and

pressure fields are very high and of strong nonlinear nature.

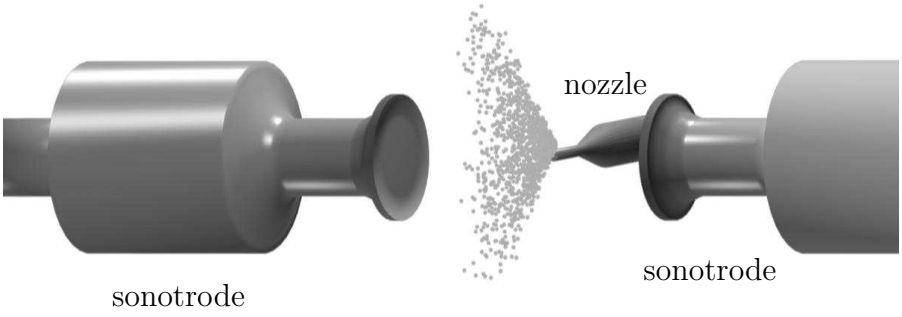

Figure 1.1.: Schema of a pilot plant

To produce spherical polymer particles, molten polymer is continuously injected via a nozzle into the central pressure node of the ultrasonic standing wave field (cf. Figure 1.1). The polymer strand disintegrates due to the acoustic forces acting on it. Thereby, discrete droplets with a particle size distribution in the range of 5 to 100 μm are generated. Due to surface tension, the shapes of these droplets become almost spherical. Particles solidify during their movement and are presorted by a subsequent cyclone. This spherical shape has advantage over irregular-shaped particles in terms of ability of maintaining static electric charges, important for direct application, and surface smoothness of coating. This process is especially interesting in the context of thermo-mechanically sensitive materials.

1.1. Problem Description

Powder coatings are manufactured by processing a main constituent resin to coarse crushing, dry blending with a hardener and various additives, and then subjecting the dry blend to extrusion, cooling, a second crushing process, and classification. Compared with solvent based paints, the manufacturing process is long and complex, and consequently the problem arises of increased process cost especially when thin film powders are considered.

Currently, the great majority of binders constituting most powder compositions are based on amorphous resins. To avoid negative side effects of the binder,

they are formed by a semi-cristalline polyester being used alone or as a mixture with amorphous resins. These semi-cristalline polyesters have a high melting point and a low transition temperature. Consequently, the melt viscosity is much lower than that of the amorphous polyester, which is commonly used in powder composition. This means that powder coating compositions based on semi-cristalline polyester exhibit better fluidity of the coating film and provide outstanding mechanical properties. Beside the many advantages especially grinding of the semi-cristalline extrudate is critical. Due to the fact that the semi-cristallinity already implies some mechanical strength of the extrudate, the enormous dissipation of heat created by the grinding process often causes partial melting of the powder during manufacturing and thus, blocking of the grinding equipment. Hence, disintegration of the melt in an ultrasonic field is the best opportunity to process this advantageous resins.

So far, equipment used for the disintegration of polymer melts in an SWA is based on the ultrasonic welding technique. Therefore, transducers applied for the atomization process are not build and optimized for this kind of application. Previous optimization of the ultrasonic field yielding preferably small particles has mainly be done empirically. The aim of these efforts was to generate particles of about 10 - 50 μm having a small particle size distribution at mass flow rates of about 300 mL/min. Because of various parameters effecting the disintegration process like frequencies and amplitudes of the sonotrodes, the geometry of the sonotrode's end face, the distance and angle of the sonotrodes to each other, and the liquid properties, empirical optimization of the whole process is too time-consuming. Experimental investigations having done so far give an idea of qualitative and partially quantitative effects of parameter variations on the disintegration process, but are still limited on the specific geometry of the employed sonotrodes. Therefore, a transfer of results related to this specific plant to other sonotrode configurations with modified geometry is not possible.

Further more, the process of atomization of liquids in an ultrasonic field itself is still not totally understood. The phenomena causing a fragmentation of the liquids surface and mechanisms proceeding near the interface are too complex to be described in total. This fundamental understanding of the SWA is necessary to

further improve the disintegration process.

1.2. Aim of the Study

The ultimate goal of our research in this field is to optimize the disintegration process in an ultrasonic standing wave atomizer in terms of energy requirements, product quality, flow rate, narrow particle distribution, and total cost. To gain maximum efficiency from this technique, a fundamental understanding of the mechanisms of disintegration, the determination of all relevant parameters, and a quantitative description of their effects is required. So far, optimization of this process is mainly done empirically. This requires time-consuming and expensive experimental work such as screening of the pressure field between the transducers and its dependency on different surface plate forms, transducer orientations as well as variations of frequency and geometrical parameters.

In Reipschläger *et al.* (2001, 2002) and Reipschläger (2002), a novel approach based on continuum mechanical modeling and numerical simulations has been initiated that allows for process optimization. This method is able to describe the disintegration process as a free surface flow in which acoustic forces act on the liquid surface. Since the phase boundary undergoes highly nonlinear changes during the disintegration process with frequent changes of its topology, the interface has to be captured implicitly. The previously applied Volume of Fluid (VOF) code used for surface capturing has been extended by new subroutines in order to determine the disintegration process quantitatively. Subsequently, numerical simulations of the disintegration of polymer strands have been performed under variation of geometrical, operational, and material properties. This allows to characterize their effects on the disintegration process quantitatively. However, in order to perform a large number of simulations for different parameters, highly efficient computational techniques are required. To validate these numerical simulations, experimental measurements have also been done.

2. Mathematical Treatment of Two-Phase Flows

The disintegration of a liquid in an ultrasonic field is a highly complex two-phase flow with compressible gas phase. On the microscopic level each fluid is discrete with its properties fluctuating violently. However, considering problems in which the dimensions of interest are very large compared to molecular scales, one may ignore the molecular structure and endow the fluid with a continuous distribution of matter. This is the continuum hypothesis valid as a statistical average of the corresponding molecular property of a large number of molecules. The fluid properties can then be treated to vary smoothly in space and time. Therefore, physical quantities such as mass and momentum associated with the matter contained within a given small volume will be regarded as being spread uniformly over this domain instead of being concentrated in a small fraction of it. Thus, all macroscopic quantities are treated as piecewise continuously functions of their location. The extensive quantities are then additive to mass, allowing for the balancing of the system on a continuum mechanical level.

Two-phase flow systems in particular are characterized by all physical quantities being continuous in each phase with at least one of these variables making a jump at the interface. In addition, two-phase systems are determined by its boundary properties. In general, the phase boundary is treated as a thin, massless layer which is considered as a piecewise smooth surface throughout mathematical modeling. The following derivations of the balance equations for two-phase flows are based on Bothe (2002). For more details about continuum mechanical modeling of two-phase flows see Ishii (1975), Silhavy (1997) and Slattery (1999).

2.1. Integral Balance

The basic approach for modeling two-phase flows are the balance equations for mass, momentum and energy in their integral form. These extensive quantities are valid over the whole calculation domain including the phase boundary.

In the following we observe the motion of two fluids which are immiscible on a molecular level. The fluids occupy an arbitrary subdomain $\Omega^-(t)$ and $\Omega^+(t)$, respectively, at time t in an arbitrary set $G \subset \mathbb{R}^3$ with $G = \Omega^- \cup \Omega^+$. The fluid flow transports the values of ϕ^- and ϕ^+ within its motion (cf. Figure 2.1). Thereby, the phase boundary $\Gamma(t)$ moves with the velocity of $\mathbf{u}_\Gamma$. Here, the unit normal vector $\mathbf{n}_\Gamma$ on $\Gamma(t)$ points in the direction of $\Omega^+(t)$. For balancing the fluid flow the ball volume $B_r := B_r(\mathbf{x}_0)$ is used. Under these assumptions the Navier-Stokes equations are derived from the conservation laws for mass and momentum.

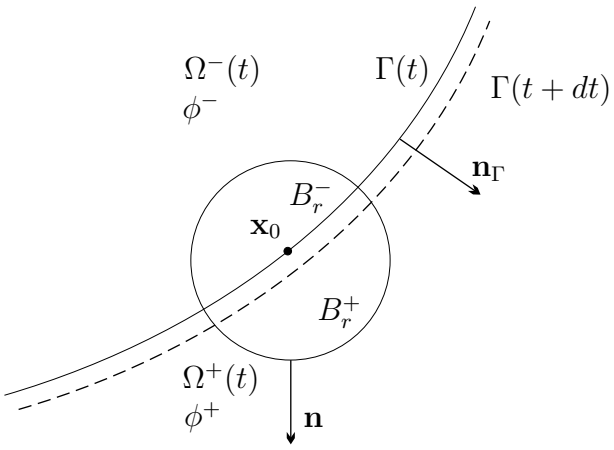

Figure 2.1.: Region ϕ^- and ϕ^+ of a two-phase system including its interface $\Gamma(t)$.

Mass Balance

To setup the balance of mass, consider a closed surface A whose position is fixed relatively to the coordinate axes, and which encloses a volume $V \subset G$ totally occupied by fluid. The mass of fluid enclosed by the surface at any distance is $\int_V \rho(\mathbf{x}, t)\, dV$, where ρ is the density of the fluid at a position $\mathbf{x}$ and time t. The net rate at which mass is flowing outwards across the surface is then $\int \rho \mathbf{u} \cdot \mathbf{n}\, dA$. Here, dV and dA are elements of the enclosed volume and area of the surrounding

surface, with the latter having the unit outward normal vector $\mathbf{n}$. Therefore, for a massless boundary layer the mass change inside the volume V will become

$$\frac{d}{dt}\int_V \rho\, dV = -\int_{\partial V} \rho\mathbf{u}\cdot\mathbf{n}\, dA\ , \tag{2.1}$$

$$\frac{d}{dt}\int_V \rho\, dV + \int_{\partial V} \mathbf{J}\cdot\mathbf{n}\, dA = 0 \quad \text{with } \mathbf{J} = \rho\mathbf{u}\ .$$

Here, the density flux $\mathbf{J}$ of the liquid will point towards the flow direction. Its magnitude represents the fluid value per time which flows through a surface unit perpendicularly to the velocity.

Momentum Balance

In general, the momentum of a body is the product of its mass with its velocity. Since in case of a fluid the velocity may vary with its position, the momentum of a substantial fluid volume $V(t)$ transported by fluid motion is expressed by the integral

$$\mathbf{I}(t) = \int_{V(t)} \rho\mathbf{u}\, dV\ .$$

According to Newton's second law, the rate of change of (linear) momentum is equal to the sum of the forces acting on the fluid:

$$\frac{d}{dt}\,\mathbf{I}(\mathrm{t}) = \sum_{\mathrm{i}} \mathbf{F}_{\mathrm{i}}$$

Two types of forces are distinguished:

- *body forces* of external fields with a given force density $\mathbf{f}$ per unit volume (e.g., gravity, Coriolis force, magnetic force),
  and
- *surface forces* $\mathbf{S}_{\partial V(t)}$ (e.g., pressure and internal friction).

Thus, Newton's law for fluids reads as

$$\frac{d}{dt}\int_{V(t)} \rho\mathbf{u}\, dV = \mathbf{S}_{\partial V(t)} + \int_{V(t)} \rho\mathbf{f}\, dV\ .$$

The correlation between $\mathbf{S}_{\partial V(t)}$ and the remaining fluid quantities has to be established by constitutive equations. When modeling an ideal fluid, internal friction is

neglected. Therefore, for a single-phase system the tension on the surface of a fluid volume V is solely determined by the pressure $p\,(x,t)$. Thus, the force $-p\mathbf{n}\,dA$ acts on the enclosed surface element dA of the surface dV:

$$\mathbf{S}_{\partial V(t)} = -\int_{\partial V(t)} p\mathbf{n}\,dA\ .$$

Instead, for real fluids in a two-phase system the previous balance equation needs to be extended by the impact of surface tension and interfacial forces:

$$\frac{d}{dt}\int_{V(t)} \rho\mathbf{u}\,dV = \int_{V(t)} \rho\mathbf{f}\,dV + \int_{\partial V(t)} \mathbf{T}\cdot\mathbf{n}\,dA + \mathbf{F}_\Gamma(t)\ .$$

Here, the stress tensor $\mathbf{T}$ is given as $\mathbf{T} = -p\mathbf{I} + \mathbf{S}$ with $\mathbf{I}$ denoting the identity tensor and $\mathbf{S}$ the viscous part of the stress tensor. This viscosity stress tensor $\mathbf{S}$ describes the tension in a fluid caused by internal friction. $\mathbf{F}_\Gamma(t)$ refers to the force on the boundary layer $\Gamma(t)\cap V(t)$ due to surface tension. This term derives from the force $\mathbf{F}_A$ acting on the area $A = V\cap\Gamma(t)$ of the phase boundary enclosed by the control volume V.

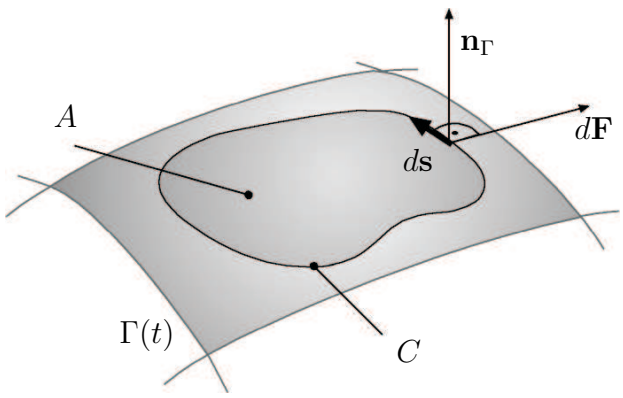

Figure 2.2.: Force on a line element $d\mathbf{s}$ on the interface $\Gamma(t)$.

Such state is pictured in Figure 2.2. Located on the phase boundary $\Gamma(t)$ is the enclosed area A with its boundary curve C. As a result of the surrounding interface, the force $d\mathbf{F}$ acts on the line element $d\mathbf{s}$ of the curve C tangential to the boundary layer $\Gamma(t)$. It is perpendicular to $d\mathbf{s}$ with an absolute value of $|\sigma d\mathbf{s}|$. Hence, the surface tension $\sigma(\mathbf{x},t)$ onto a line element of the length $|d\mathbf{s}|$ results in a force $d\mathbf{F} = \sigma d\mathbf{s}\times\mathbf{n}_\Gamma$. Thus, the integral along the boundary leads to the force onto the

area A,

$$\mathbf{F}_A(t) = \oint_C \sigma(d\mathbf{s} \times \mathbf{n}_\Gamma) = \oint_C d\mathbf{s} \times \sigma\mathbf{n}_\Gamma \,, \tag{2.2}$$

pointing opposite to the area A. For the special case of a vector product eq. (2.2) as a line integral can be transformed into a surface force by applying Stoke's theorem (Appendix A.1):

$$\mathbf{F}_A(t) = \int_A (\mathbf{n}_\Gamma \times \nabla) \times \sigma\mathbf{n}_\Gamma \, dA \,.$$

The term $(\mathbf{n}_\Gamma \times \nabla) \times \sigma\mathbf{n}_\Gamma$ denotes the surface density of the surface tension (force) $\mathbf{f}_\Gamma(\mathbf{x}, t)$. By transformation it results

$$\mathbf{f}_\Gamma = \nabla\sigma - \mathbf{n}_\Gamma(\mathbf{n}_\Gamma \cdot \nabla\sigma) + \sigma\mathbf{n}_\Gamma \cdot \nabla\mathbf{n}_\Gamma - \sigma\mathbf{n}_\Gamma(\nabla \cdot \mathbf{n}_\Gamma) \,. \tag{2.3}$$

By subtracting the normal part of the gradient with respect to the normal $(\mathbf{n}_\Gamma(\mathbf{n}_\Gamma \cdot \nabla\sigma))$ from the surface tension gradient $(\nabla\sigma)$, the two terms yield the surface gradient $\nabla_\Gamma\sigma$ of σ. If the surface tension σ is constant, these two parts vanish acting perpendicular to the surface. This does not mirror the typical condition since surface tension especially depends on temperature and the concentration of surface active substances ($\sigma = \sigma(T, c_\Gamma)$). Therefore, the significance of this term may increase with the occurrence of temperature or concentration gradients at the interface. The influence of these gradients on σ is known as Marangoni effect.

Taking into account that the third addend of eq. (2.3) equals zero, the equation simplifies to

$$\mathbf{f}_\Gamma = \nabla_\Gamma\sigma - \sigma\mathbf{n}_\Gamma(\nabla \cdot \mathbf{n}_\Gamma) \,.$$

Including the curvature

$$\kappa_\Gamma(\mathbf{x}, t) = -\nabla \cdot \mathbf{n}_\Gamma(\mathbf{x}, t) \,,$$

the surface force results in

$$\mathbf{F}_\Gamma(t) = \int_A \mathbf{f}_\Gamma \, dA \quad \text{with} \quad \mathbf{f}_\Gamma = \nabla_\Gamma\sigma + \sigma\kappa_\Gamma\mathbf{n}_\Gamma \,.$$

Therefore, the momentum balance for a fixed volume element V determines as

$$\frac{d}{dt}\int_V \rho\mathbf{u} \, dV + \int_{\partial V} \mathbf{J} \cdot \mathbf{n} \, dA = \int_V \rho\mathbf{f} \, dV + \int_{V\cap\Gamma(t)} \mathbf{f}_\Gamma \, dA \tag{2.4}$$

with the momentum flux $\mathbf{J} = \rho\mathbf{u} \otimes \mathbf{u} - \mathbf{T}$.

2.2. Differential Balance

Based on the integral balance for a fixed volume element, the corresponding differential balance equation and jump conditions can be derived by localization. In a first step, the surface integrals over the boundary ∂V need to be transformed to volume integrals using the Gaussian divergence theorem (Appendix A.2). Subsequently, the interior of the phase is divided by the absolute value $|V|$ of the balanced volume $V = B_r(\mathbf{x}_0)$ and the ball B_r is constricted towards the point $\mathbf{x}_0$ ($r \to 0+$). For the derivation of the jump conditions on $\Gamma(t)$ the particular volume integral is divided into its phase fractions, in order to complete the missing areas of the boundary layer. At this point the differential balance equations are applied to both phases. Further, the jump conditions are achieved by division of the area $|\Gamma_r|$ inside the balance domain and contraction of the ball to $r \to 0+$. Whereas the differential balance equations are restricted to the interior of the particular phase, the jump conditions describe the actual state at the interface. Further, these need to be supplemented by constitutive equations.

Mass Balance

The flux of a quantity outwards across a surface A due to fluid motion is expressed by the conservation law of eq. (2.1). Using the Gaussian divergence theorem on the right hand side of this equation transfers the surface integral into a volume integral. The requirement that the previous statement has to be valid for all choices of the volume V bounded by A then gives the differential equation

$$\frac{\partial}{\partial t}\,\rho + \mathrm{div}(\rho\mathbf{u}) = 0\,. \tag{2.5}$$

For the special case of an incompressible fluid the following equation system results:

$$\mathrm{div}\mathbf{u} = 0 \quad \text{and} \quad \frac{\partial}{\partial \mathrm{t}}\,\rho + \mathbf{u}\cdot\nabla\rho = 0\,.$$

If there are no density variation in time or space, i.e. , $\rho(\mathbf{x},t) = \rho_\infty = \text{const.}$, this results in the continuity equation for isochore fluids with

$$\mathrm{div}\mathbf{u} = 0\,. \tag{2.6}$$

Momentum Balance

In the same way as the differential equation for the conservation of mass, the equation of motion is developed. If there is only gravity as the solely body force acting in negative direction along the z-achses, the momentum balance becomes

$$\frac{\partial}{\partial t}(\rho\mathbf{u}) + \mathrm{div}(\rho\mathbf{u}\otimes\mathbf{u} - \mathbf{T}) = -\rho g\mathbf{e}_z \,, \tag{2.7}$$

with the stress tensor $\mathbf{T} = -p\mathbf{I} + \mathbf{S}$. For Newton fluids the viscosity stress tensor $\mathbf{S}$ is given by

$$\mathbf{S} = \lambda(\mathrm{div}\mathbf{u})\mathbf{I} + \mu\left(\nabla\mathbf{u} + (\nabla\mathbf{u})^{\mathrm{T}}\right) \,. \tag{2.8}$$

Here, λ denotes the bulk viscosity and μ the dynamic viscosity. For fluids of constant density ($\rho(\mathbf{x},t) = \rho_\infty = \text{const.}$) and arbitrary body forces $\mathbf{g}$ the momentum balance can be rewritten as

$$\frac{\partial}{\partial t}\mathbf{u} + \nabla\cdot(\mathbf{u}\otimes\mathbf{u}) = -\frac{1}{\rho}\nabla p + \frac{\mu}{\rho}\Delta\mathbf{u} + \mathbf{g} \,. \tag{2.9}$$

The quotient of $\mu/\rho = \nu$ is called the kinematic viscosity. If further internal friction of the fluid (viscosity) characterized by energy dissipation is neglected, the *Euler* equation results:

$$\frac{\partial}{\partial t}\mathbf{u} + \nabla\cdot(\mathbf{u}\otimes\mathbf{u}) = -\frac{1}{\rho}\nabla p \,.$$

The equation of motion (2.9) in connection with the conservation of mass (2.6) for the special case of incompressible fluids are called the *Navier-Stokes* equations.

2.3. Dimensionless Form of the Navier-Stokes Equations

Information of the flow is contained in the parameter characterizing it like the dynamic viscosity μ and the density ρ, and the characteristic values for the length L and the velocity U. Furthermore, by L and U a characteristic time scale is determined as $T = L/U$. If these parameters are combined in a suitable way to yield dimensionless quantities, then these enable the comparison of different flow conditions or the similarity of flows, respectively. Therefore, dimensionless quantities are formed by their dimensional counterparts:

$$\mathbf{x}' := \frac{\mathbf{x}}{L} \,, \quad \mathbf{u}' := \frac{\mathbf{u}}{U} \,, \quad t' := \frac{U\,t}{L} \,, \quad p' := \frac{p-P}{\rho U^2} \,, \tag{2.10}$$

with given scalar constants L, ρ, U, P.

Recasting eq. (2.9) by inserting the variables of eq. (2.10) leads to the equation

$$\frac{\partial}{\partial t'}\mathbf{u}' + \mathbf{u}' \cdot \nabla' \mathbf{u}' = -\nabla' p' + \frac{\mu}{\rho U L}\Delta' \mathbf{u}' + \frac{L}{U^2}\mathbf{g} \,,$$

where the operators ∇' and Δ' are those with respect to the dimensionless position vector $\mathbf{x}'$. Concluding, flows will be dynamically similar, if their parameters $\mu, U, \rho, L, \mathbf{g}$ are similar as well or the dimensionless quantities

$$Re := \frac{\rho U\, L}{\mu} \quad \text{(Reynolds number)} \quad \text{and}$$

$$Fr := \frac{U}{\sqrt{L\,||\mathbf{g}||}} \quad \text{(Froude number)}$$

of the flows coincidence.

Both, the dimensionless Reynolds number as well as the Froude number describe properties of the fluid flow. The Reynolds number characterizes the relative magnitude of inertial and viscous forces. Therefore, it gives an idea about the impact of viscose effects ($1/Re \nabla \mathbf{u}$) on fluid motion. It further needs to be considered that low $1/Re$ still has a huge influence on the flow field. This is because it increases the order of the equation to two and especially changes the boundary conditions. For huge $1/Re$ (creeping flow) most likely the Stokes flow is employed as an approximation. Thus, the convective fraction $(\mathbf{u} \cdot \nabla \mathbf{u})$ is neglected. Therefore, a linear problem results. Instead, the Froude number represents the ratio of inertial to gravitational forces.

The dimensionless form of the continuity equation displayed by eq. (2.6) simply becomes

$$\nabla' \cdot \mathbf{u}' = 0.$$

2.4. Jump Conditions

For the derivation of the jump conditions the integral balance equation (2.4) for a fixed volume is used. This equation is applied on the volume of a ball $B_r := B_r(\mathbf{x}_0)$ with $\Gamma_r := \Gamma \cap B_r$ (cf. Figure 2.2). Since the interface is free to move, $\Gamma_r = \Gamma_r(t)$

and, therefore, even $B_r^{\pm} = B_r^{\pm}(t)$. The integrals are separated into their fractions of B_r^+ and B_r^-. Thereon the differential balance equations are used.

As a result of this approach, boundary conditions for each phase can be derived. In case of conservation of mass the jump condition at the interface between the phase ϕ^+ and ϕ^- becomes

$$[\rho(\mathbf{u} - \mathbf{u}_\Gamma)] \cdot \mathbf{n}_\Gamma = 0 \,, \tag{2.11}$$

where $\mathbf{u}_\Gamma$ is the interfacial velocity. Here, $\mathbf{n}_\Gamma$ is the unit normal vector on the interface directed into the gas phase and the symbol

$$[\psi(x)] := \lim_{h \to 0+} \psi(x + h\mathbf{n}_\Gamma) - \lim_{h \to 0+} \psi(x - h\mathbf{n}_\Gamma)$$

stands for the jump of a physical quantity ψ across the interface.

Similarly, the equation for momentum conservation across the interface is expressed:

$$[\rho\mathbf{u} \otimes (\mathbf{u} - \mathbf{u}_\Gamma) + p\mathbf{I} - \mathbf{S}] \cdot \mathbf{n}_\Gamma = \nabla_\Gamma \sigma + \sigma\kappa_\Gamma \mathbf{n}_\Gamma \,, \tag{2.12}$$

where $\nabla_\Gamma \sigma$ denotes the surface gradient of the surface tension and $\kappa_\Gamma = -\nabla \cdot \mathbf{n}_\Gamma$ is the sum of the local (principal) curvatures of the interface.

In the present work it is assumed that the two-phase system under consideration does not endure phase changes like evaporation or condensation. Consequently, there are no convective fluxes across the interface, i.e. the normal components of the fluid velocities are continuous at the phase boundary and equal to the surface's normal velocity. Finally, we assume no-slip conditions at the interface as well as constant surface tension. Then the jump conditions (2.11), (2.12) simply become

$$[\mathbf{u}] = 0, \qquad [p\,\mathbf{I} - \mathbf{S}] \cdot \mathbf{n}_\Gamma = \sigma\kappa_\Gamma \mathbf{n}_\Gamma \,. \tag{2.13}$$

By neglecting the viscosity stress tensor $\mathbf{S}$, the right part of eq. (2.13) becomes the *Young-Laplace* equation:

$$\Delta p = \sigma\kappa_\Gamma = \sigma \left(\frac{1}{R_1} + \frac{1}{R_2} \right) , \tag{2.14}$$

where R_1 and R_2 denote the principal radii of curvature. For stagnant fluids $\mathbf{u} = 0$ and consequently $\mathbf{S}$ equals zero as well. In this case *Young-Laplace* is an exact solution of the flow system. For more details about the derivation of jump conditions for two-phase flow see Reipschläger (2002).

3. Numerical Approach

The disintegration of a liquid in an ultrasonic field is a highly complex two-phase flow with compressible gas phase. Any numerical description of this process that aims in the prediction of particle size distributions has to take into account the strong nonlinear behavior which appears during the formation of complex topologies of the disperse phase such as liquid lamellae, ligaments, and droplets of different sizes. Thus, modeling and simulation of the mechanisms of liquid disintegration in an ultrasonic standing wave field requires a numerical method which allows for the computation of the dynamics and topology of the free phase boundary.

The mechanisms of disintegration can vary according to the type of atomization process. Hence, simplifying models that do not account for the interface dynamics but still describe atomization in a general setting seem to be out of reach. Therefore, the principal aim here is to compute the two-phase flow without such simplifications. Difficulties occur because of the different length- and time-scales associated with ultrasonic sound field and droplet dynamics phenomena. On the one hand, the nonlinear oscillations within the ultrasonic sound field take place on a time scale of about 50 μs, while the relevant length scale is the distance between the two sonotrodes of about 50 mm. On the other hand, droplet breakup requires a much longer period of about 5 -20 ms due to inertia of the liquid, but proceeds on a decade of smaller length scales from a few millimeters down to a few μm. A so-called Direct Numerical Simulation (DNS) of such a two-phase flow with full resolution of the interfacial dynamics on all relevant length- and time-scales, therefore, requires extreme numerical efforts and is not possible with today's computer technology. While commercial Computational Fluid Dynamics (CFD) software is in principle able to calculate compressible transient two-phase flow, systems of this complexity cannot be handled. Furthermore, process optimization requires a large number of variations of relevant material and operational properties. Hence, DNS would be

much too expensive and time-consuming. For this reason a partial decoupling into the compressible single phase gas flow corresponding to the resonant sound field and the droplet dynamics given by the free surface flow is done. The effect of the compressible gas phase onto the liquid surface is taken into account by means of additional interfacial source terms within the momentum jump conditions, leading to a one-way coupling. The dynamics of the liquid flow are captured by means of transient three-dimensional simulations with a two-phase Navier-Stokes solver employing a volume tracking method to capture the disperse phase. With this overall approach, the full disintegration process is split into two parts which are solved separately using a specialized numerical method that fits its particular needs.

3.1. The Numerical Method

The study of moving interfaces is one of the most important areas in technological and engineering fields. Its application involves solid mechanics as material shaping processes and fluid mechanics like breakup of a jet, coalescence of liquid drops or wave breaking. For numerical modeling of these tasks different approaches have been developed to treat these two classes of problems. The finite element method combined with a Lagrangian description of the movement is generally applied for material shaping problems (Lock *et al.*, 1998). For the study of fluid-structure interactions a mixed description is found to be the most suitable one: Lagragian in solid and Eulerian in fluids with coupling at the interface. Finally, either the mixed description or the Eulerian one is most likely used for the treatment of two phase flows with fluid-fluid interaction. This approach can handle complex interface problems and is employed in numerical simulations of such problems (Hyman, 1984; Laskey *et al.*, 1987; Floryan & Rasmussen, 1989).

In case of droplet breakup and strand disintegration as conducted in this study particular complex shaped interfaces result. The difficulties in treating such flows can be attributed to

- the interface location,
- the interface topology, and

- the interfacial mechanism.

Most of the developed methods use the Eulerian approach to model the fluid flow and various techniques have been employed to track the interfaces through the fixed mesh. The two basic methods are surface tracking and volume tracking.

In surface tracking methods markers are initially placed on the fluid's interface and are subsequently followed within the flow. A disadvantage of this method is that coalescence cannot be easily treated with these techniques. Further, Osher & Sethian (1988) found that curvature effects cause another drawback of the marker-based method: For large and complex motion, particles come together in regions of high curvature causing numerical instability. Therefore, a regridding step has to be employed which usually contains diffusion-like errors. This effect can even dominate the real effect of curvature.

In the volume tracking method the interface is implicitly tracked. In this case markers are used to identify the fluid itself. These markers can be, e.g., one of the fluids properties or another function. Employing this method the fluid is identified in each cell of the computational domain, where it is present. The interface is located somewhere inside a cell which contain more than one fluid and is finally reassembled cell by cell. Two methods developed by this approach are the Marker-and-Cell (MAC) (Harlow & Welch, 1965; Welch *et al.*, 1966) and the Volume of Fluid (VOF) methods (Hirt & Nicols, 1981). The MAC technique employs massless particles as markers. This approach causes particles to accumulate in some parts of the mesh leading to an inaccuracy in locating the interface and, therefore, separating the particles. Instead, the VOF method defines a marker function f denoting the fraction of a cell volume that is occupied by one of the fluids. The function can adopt values between zero and unity, whereas a cell is either empty or filled, respectively, with a specific fluid. If f is between zero and unity, the interface of the fluid is located in that specific cell. The VOF technique was introduced by Hirt & Nicols (1981) for infinite difference structured meshes. Rectangular grids were required since the f value is determined using a donor-acceptor flux approximation of Rawshaw & Trapp (1976) which requires rectangular cells. The main advantage of this volume tracking method was that it can handle interfaces which undergo large deformations and treat multiple fronts. This basic approach of Hirt & Nicols

(1981) was extended over the years by, e.g., Kothe & Mjolsness (1992); Rider *et al.* (1995) and Rider & Kothe (1998) which is now applicable on arbitrary grids. Especially in this case the VOF technique is combined with the finite volume (FV) method for solving the partial differential equations that calculates the quantities of the variables averaged across the cell volume. This is due to the advantage of the finite volume method over the finite difference (FD) method that it does not require structured meshes. In addition, the finite volume method is preferable to other techniques since boundary conditions can be applied non invasively. This is true since the values of the conserved variables are located within the volume element and not at nodes or surfaces (Versteeg & Malalasekera, 1995).

Therefore, the VOF technique in combination with the finite volume method is widely used during the last couple of years to model complex shaped structures and highly flexible processes. These are flow phenomena as, e.g., disintegration or coalescence of fluid regions. Since the VOF method implicitly captures the shifting topology of such processes, no mechanisms need to be developed for the reconstruction of phase boundaries. Hence, the VOF method works without further approximation. Although the VOF technique is not restricted on structured grids, applications commonly used are based on such meshes. Therefore, these grids as used in *FS3D* do have the advantage of easy discretization of the calculation domain for parallelization. Additionally, since the calculation of the flow variables solely requires values of the adjacent cell layers, a good proportion between calculation cost and communication of the participating processors result. This is an advantage over other techniques since the calculation domain used for the simulation of the disintegration process is made of up to 16 million grid cells. Such high grid resolution is necessary in order to capture droplets down to a few μm generated during the disintegration process. Therefore, the simulation of such processes requires a massive parallelization of the numerical method. Finally, the VOF method as integrated into *FS3D* allows for easy implementation of impacts as, e.g., surface tension on the fluid surface. This is one of the main essential advantages used throughout this work: Additional source terms characterizing the momentum flux through the surface are incorporated into the VOF-code *FS3D*.

3.2. Decoupling of the Simulation Process

In the first step, oscillating pressure and velocity of the ultrasonic sound field are computed by solving the Navier-Stokes equations for compressible viscous flows (eq. 2.5 & 2.7). In addition to the mass and momentum balance, the energy equation is taken into account, since large sound intensities appearing in an SWA lead to high temperature fluctuations inside the gas phase. Due to the axial symmetry of the configurations, computations of the ultrasonic sound field are carried out in two-dimensions employing cylindrical coordinates. For numerical simulation of the ultrasonic sound field during the continuous disintegration process of polymer in a double oscillation unit, *CFX 4.4* (AEA Technology GmbH, 2001) is used. To investigate levitated droplets, the software tool *Fluent 6.1.18* (Fluent Inc., 2003) is chosen. Both CFD-codes have been extended by user-defined subroutines for the output of time-averaged pressure and velocity fields. *Fluent* is employed for the computation of ultrasonic sound fields with liquid-gas interactions, since it allows for easy patching of spherical liquid obstacles into the computational domain.

In the second step, transient DNS of the disintegration process are performed in 3-D with an advanced VOF method (Hirt & Nicols, 1981). This method is incorporated into the non-commercial VOF code *FS3D* (Free Surface 3D), developed at the "Institut für Thermodynamik der Luft- und Raumfahrt" (ITLR) Stuttgart (Rieber, 2004). Within the VOF method the Navier-Stokes equations for an incompressible time-dependent two-phase flow are solved. The validation of the code has been done based on multiple cases relevant in application. Thus numerical simulation and experimental validation was made for drop-wall as well as binary droplet collision (Rieber & Frohn, 1997), deformation of moving droplets (Rieber & Frohn, 1998; Rieber *et al.*, 2000) and the crown formation of a drop splashing on a liquid surface (Rieber & Frohn, 1999).

This programm was extended by Reipschläger *et al.* (2002) to incorporate pressure and velocity fields previously calculated in *CFX*. These are used as source terms to account for the influence of the ultrasonic field onto the liquid phase. During this project the interface was improved to automatically determine the geometries used in *CFX* and *Fluent*, respectively. Hence, the coordinates of the grid including its stream variables are read out and automatically transferred into the

setup of *FS3D*. Therefore, the *FS3D* grid is determined as well and compared to the ones from simulation of the sound field. Finally, the fluid data to be transferred are simultaneously averaged over divers acoustic cycles of the ultrasonic field.

Since numerical simulations of the ultrasonic field are done in 2-D with rotational symmetry, the data need to be transferred into cubic coordinates in 3-D of the VOF-code *FS3D*. Therefore, a rotation including an interpolation of the parametric field is necessary. This is done by a cubic spline interpolation (Akima, 1972) which maps the *CFX* and *Fluent* data, respectively, onto the *FS3D* geometry. The routine is further able to interpolate the stream parameters from a rough grid into a smoother subdivided one. This is necessary since the disintegration of continuous liquid strands requires much smoother grids than the ones for simulations of the ultrasonic field. Instead, the deformation of droplets demand a straight transfer of data from *Fluent* to *FS3D* to quantitatively determine droplet deformation. In this case both tools work with the same grid resolution and, therefore, a direct coupling without interpolation is necessary. For parallel computing of the VOF simulation a separation of the calculation domain and its scalar field is possible according to the number of computer nodes. Finally, the interface supports multiple conversion of data sets to create input files for time dependent import into *FS3D*. The overall progression of numerical simulations of the ultrasonic field to the simulations of the disintegration process including the data conversion is shown in Figure 3.1.

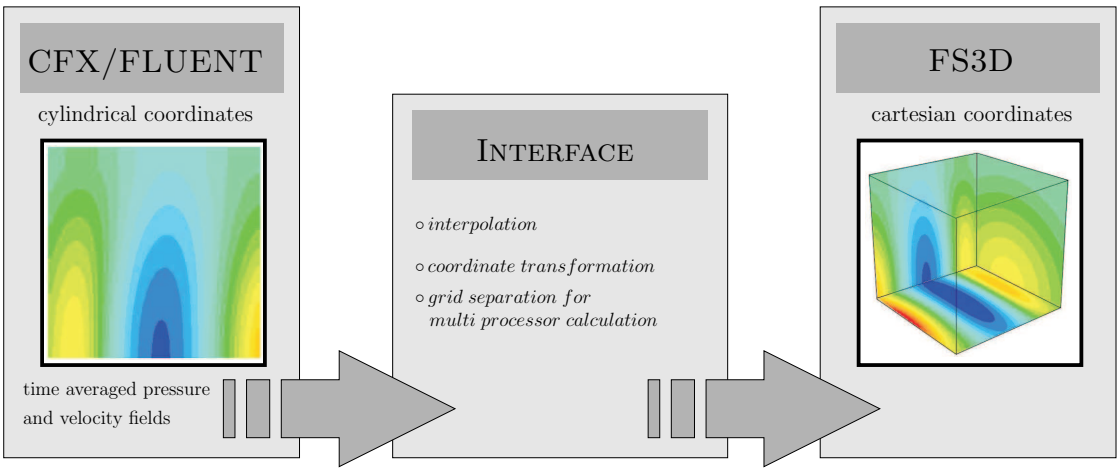

Figure 3.1.: Progression of numerical simulation and data conversion.

To visualize the results generated by *FS3D* a post-processor of the *Fluent Inc.* was used. Therefore, Reipschläger *et al.* (2002) developed a conversion tool to transform the data sets produced by *FS3D* during numerical simulation of the two-phase flow into the *universal*-format of FLPOST (Fluent Inc., 2000). An advantage of this programm is the highly advanced visualization technique including various ways of illuminating droplets and strands of polymer inside the calculation domain. Contrariwise the programm is restricted to a low number of data points to be visualized. For grid resolutions of more than 64^3 data points the programm becomes much too slow and, therefore, unfunctional. Further, newer versions of *Fluent* do not support FLPOST as an independent tool in addition to the FLUENT solver itself anymore.

In order to effectively visualize data sets of more than 64^3 data points PADVIZ was used. This tools is part of the CFD modeling tool $padfem^2$ developed at the Center for Parallel Computing (PC^2) at the Paderborn University. Especially because of the ability of parallel data processing and visualization it is able to handle huge data sets. Therefore, a conversion tool was programmed to enable the input of data sets from *FS3D* into PADVIZ and to transform the data with respect to the symmetry planes applied in *FS3D*.

3.3. Method for the Simulation of the Ultrasonic Field

The simulation of ultrasonic standing wave fields is done by means of the commercial CFD software package. For numerical simulation of the ultrasonic sound field during the continuous disintegration process of polymer in a twin-oscillation unit *CFX 4.4* (ANSYS) is used. To investigate levitated droplets the software tool *Fluent 6.1.18* (Fluent Inc.) is chosen. Both CFD-codes have been extended by user-defined subroutines for the output of time-averaged pressure and velocity fields. *Fluent* is employed for the computation of sound fields with liquid-gas interactions, since it allows for easy patching of spherical liquid obstacles into the computational domain.

In both cases the balance equations for compressible liquid flows are solved

with a finite volume approach based on block-structured grids. The **P**ressure-**I**mplicit with **S**plitting of **O**perators (PISO) algorithm is chosen to derive pressure fields from the continuity equation by using a relationship between velocity and pressure corrections during numerical simulation. The PISO pressure velocity coupling scheme is part of the SIMPLE family of algorithms. Such a SIMPLE algorithm uses a **S**emi-**I**mplicit **M**ethod for **P**ressure-**L**inked **E**quations (Patankar, 1980; Ferziger & Peric, 2002). As a second pressure-correction equation the PISO coupling is applied in order to improve the solution of the momentum equations while maintaining continuity.

Oscillating pressure and velocity of the ultrasonic sound field are then computed by solving the Navier-Stokes equations for compressible viscous flows. In addition to mass and momentum balance the total enthalpy is included to incorporate temperature variations since large sound intensities appearing in an SWA lead to high temperature fluctuations inside the gas phase:

$$\partial_t (\rho\, h) + \nabla \cdot (\rho \mathbf{u}\, h) - \nabla \cdot (k \nabla T) = \partial_t p \; . \tag{3.1}$$

Here, ρ denotes the density, $\mathbf{u}$ the velocity, p the pressure, k the conductivity coefficient, h the total enthalpy and T the temperature. Because of the significant impact of temperature variations on sound acoustics, it is investigated in more detail later on. Further remarks on that subject are found in Section 4.7.3.

Since the density of the compressible liquid gas flow depends on temperature and pressure, it is implicitly calculated inside the CFD-solver. Thereby, the gas phase is treated as an ideal gas and, therefore, calculates as

$$\rho_g = \frac{(p_{gauge} + p_{ref}) M_g}{RT}$$

with M_g denoting the molecular weight of the gas and R the universal gas constant. To avoid the problem of roundoff errors when computing pressure gradients, all pressures computed and reported by *CFX* and *Fluent*, respectively, are gauge pressure p_{gauge}. The gauge pressure simply derives by subtracting a fixed reference pressure p_{ref} from the absolute, thermodynamic pressure p. In general, this reference pressure is simply determined by the standard atmospheric pressure, $1.013 \cdot 10^5\,\mathrm{N/m^2}$.

Due to the axial symmetry of the configurations in an SWA and SWL, computations of the ultrasonic sound field are carried out in two dimensions employing cylindrical coordinates. To capture the movement of the sonotrode face, prescribed velocities at the inlet are used. The radial velocity component at the sonotrode's end face is taken to be zero ($v = 0$), while the axial component is given by $u = u_0 \sin \omega t$. Therefore, the movement of the sonotrodes' surface are treated as uniform over the whole area. This approach was justified during experimental investigations of the sonotrodes. Scans of the surface using a laser vibrometer showed a uniform, rotational symmetric oscillation over the whole sonotrode's face.

Simulations of droplet deformation as well as strand disintegration (Chapter 5 and Chapter 6) are carried out for sonotrodes with diameter of 35 mm assuming rotational symmetry and oscillation frequencies of about 20 kHz. More precisely, the two sonotrodes are slightly distorted by a difference of 230 Hz in frequency, resulting in a modulation of the ultrasonic field by superimposed oscillation of pressure and velocity amplitudes (cf. Figure 4.6). The computational domain encloses additional space up to a radius of 52.5 mm around the sonotrode axis with boundary conditions set to constant pressure. Because of different gradients of the ultrasonic field in axial and radial direction, respectively, the spatial grid resolution is chosen to a minimum cell length of 0.3 mm in axial and 0.875 mm in radial direction in case of an undisturbed ultrasonic field. For this and even smoother grids the numerically computed pressure fields are found to be independent from the grid resolution. Coarser meshed grids would fulfill the Courant-Friedrich-Levi (CFL) criterion (Griebel *et al.*, 1995) if the time step size is decreased simultaneously, but will cause gradients of the flow variables to be solved insufficiently. Instead, if the sound field is solved including a liquid obstacle using *Fluent*, much smoother grids are necessary to implicitly capture the liquid surface. Therefore, equally sized meshes of 0.078 mm around the liquid droplet are used to compute the ultrasonic field. On the one hand, this is because of limitation due to computer technology. Smoother grids would cause much longer computational times and, therefore, would exceed acceptable conditions. On the other hand, computed pressure and velocity fields are found to be independent from the grid resolution in case of a flattening droplet of 45 μL. Since meshes of 0.078 mm in diameter cannot resolve separating fragments from an atomizing droplet of that size, this

grid independence of sound fields is only valid in case of deforming droplets.

For the generation of geometries including their grids the software tool *Meshbuild* from *AEA Technology* is used in case of *CFX 4* and *Gambit* from the *Fluent Inc.* for the compilation of geometries used in *Fluent 6*. In both cases structured, the contour fitting, meshes are used for spatial discretization of the concave sonotrode geometry. Exemplarily, grids used for numerical simulation of an SWA and an SWL generated by GAMBIT are show in Figure 3.2.

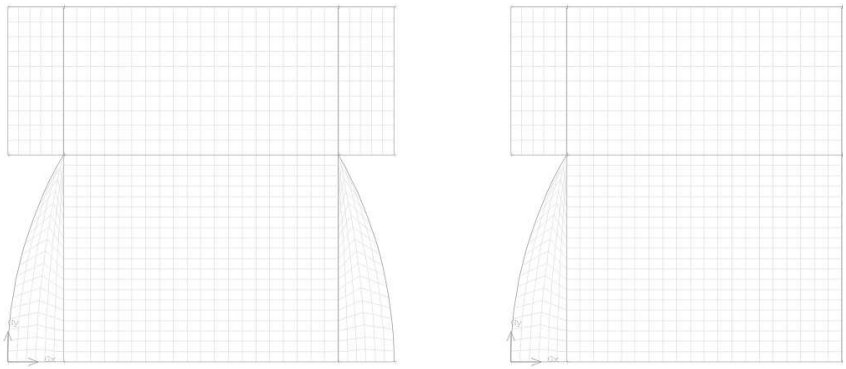

(a) atomizer (b) levitator

Figure 3.2.: Setup of the calculation domain and grid structure for numerical simulation.

During numerical simulation of the ultrasonic field each oscillation cycle is resolved in time by 250 time steps. Hence, for simulations of sound fields with an excitation frequency of 20 kHz the time step size results to be 0.2 μs. Thereby, the temporal discretization should satisfy the Nyquist criteria $f_{sample} \leq 2f_{max}$ (Broch, 1990). The criteria states that the reconstruction of a arbitrarily signal has to be performed with at least twice the maximum frequency of that signal.

3.4. Method for the Simulation of Free Fluid Surface

The deformation and breakup of droplets and strands in an ultrasonic standing wave fields involves various dynamic modifications of the liquid surface. Therefore, Hirt & Nicols (1981) introduced a Volume of Fluid (VOF) method to implicitly capture the residence region of two immiscible liquid flows. It was further presumed that these fluids are incompressible and of a huge density difference.

Based on phase-related balancing advection of the disperse phase is governed by an additional transport equation for the volume fraction f of this phase, i.e.

$$\partial_t f + \nabla \cdot (f\mathbf{u}) = 0 \tag{3.2}$$

determining the temporal propagation of the phase with respect to the flow field. Hence, the balance equations of mass, momentum and energy in addition to eq. (3.2) can be solved for both phases simultaneously. Using the VOF method the disperse liquid phase corresponds to regions where the f-function has the value 1, the continuous phase is characterized by $f = 0$, while the interface is located within grid cells for which $0 < f < 1$. Therefore, cells of $0 < f < 1$ comprise both phases. In case of droplet deformation and breakup cells with $f = 0$ characterize the surrounding gas phase and $f = 1$ denotes the droplet or liquid strand, respectively. Figure 3.3 represents a supposable distribution of the f-variable inside the calculation domain to clarify the approach.

0.15	**0.02**	**0**	**0**	**0**	**0**
1	**0.64**	**0.29**	**0**	**0**	**0**
1	**1**	**0.87**	**0.14**	**0**	**0**
1	**1**	**1**	**0.38**	**0**	**0**
1	**1**	**1**	**0.56**	**0**	**0**

Figure 3.3.: Cell occupation of a liquid drop ($f > 1$) in a surrounding gas phase ($f = 0$) based on the VOF-method with PLIC reconstruction of the interface.

Surface tension (cf. Section 3.4.1) is taken into account based on the conservative approximation of Lafaurie *et al.* (1994). For accurate approximation of the

free fluid surface spatial discretization of high resolution are necessary. This leads to computational grids having up to 16 million grid cells. Therefore, a massive parallelization of *FS3D* is essential here.

The VOF-code *FS3D* is based on a finite volume method which is used to discretize the transport equations for mass, momentum and volume fraction *f*. Thereby, the location of the volume fraction f is derived by determining the actual velocity field $\mathbf{u}$ and the corresponding value of the prior f-function. The Navier-Stokes equations are solved by a second-order projection method for incompressible liquid flows based on Godunov's conservative projection method (Bell *et al.*, 1989; Tau, 1994). The approach uses a MAC method to store the derived flow variables on a staggered grid and a split-explicit time differencing schema. Thus, the Navier-Stokes equations are split and successively solved. Finally, the remaining pressure field is calculated based on a cell-centralized discretization of the Poisson equation. Therefore, a multigrid method is applied which offers the robustness necessary to handle huge density ratios (Wesseling, 1992). For more details about *FS3D* and implemented numerical solutions see Rieber (2004).

After determining the volume fraction f at a distinct time t, the phase boundary needs to be reconstructed. This is necessary to solve the transport equation of the f-variable. Thus, the interface in a cell of interest is adjusted regarding it adjacent cells. The most ordinary way originally used by Hirt & Nicols (1981) is the **S**imple **L**ine **I**nterface **R**econstruction (SLIC) algorithm by Noh & Woodward (1976). It produces an interface consisting of line segments, constructed parallel to a grid face. Since this algorithm only uses line segments that are parallel to the coordinate axes, the resulting interfaces are generally discontinuous. An improvement to this method is the **P**iecewise **L**inear **I**nterface **R**econstruction (PLIC) algorithm such as the one from Youngs (1992) or Puckett *et al.* (1997). The method involves two steps for reconstruction. In a first step, the normal on the interface is calculated using the gradient of the volume fraction *f*. Second, the intercept of that interface is calculated such that it intersects the exact volume fraction in the cell of interest. Although the resulting interface is still discontinuous, the approach allows a more appropriate reconstruction of the liquid phase boundary. Nevertheless, it is still necessary to have at least on grid cell of $f = 0$ between to phase boundaries

to distinguish them as separated, independent droplets (Figure 6.7).

3.4.1. Surface Tension

The accurate computation of surface tension is a critical task throughout the simulation of free fluid boundaries. Since molecular forces are responsible for placing liquid surfaces in tension, the scale of that process in general is not solved in computational fluid dynamics. The resulting surface tension is incorporated in Laplace formula as a surface stress condition (Landau & Lifshitz, 1959). In recent models this computationally inconvenient description of the effect of surface tension is replaced by an equivalent volume force, which acts on a length scale comparable to the grid spacing rather than the thickness of the interface (Brackbill *et al.*, 1992; Lafaurie *et al.*, 1994; Truggvason *et al.*, 2001). Such an approach is necessary since there is no strict boundary layer numerically generated by the VOF method. Instead, a continuous transition area of thickness l exists expanding over several grid cells. Therefore, the curvature and the pressure jump at the interface have to be calculated accurately. These requirements were obtained first by Brackbill *et al.* (1992) on a VOF method. The Continuum Surface Force (CFL) model as a non-conservative approach expresses the area-related surface force $\mathbf{f}_\Gamma(\mathbf{x}_\Gamma)$ at the interface Γ in terms of a volume-related force $\mathbf{f}_{\Gamma,V}(\mathbf{x})$ inside a small transition area around the interface. If the thickness l of the continuous boundary layer declines against zero, both forces can be equated:

$$\int_A \mathbf{f}_\Gamma(\mathbf{x}_\Gamma) = \lim_{l\to 0} \int_V \mathbf{f}_{\Gamma,V}(\mathbf{x}) dV \ . \tag{3.3}$$

By using Dirac's delta distribution δ (Appendix A.3) on eq. (3.3) the surface integral can be transformed into a volume integral.

$$\int_A \mathbf{f}_\Gamma(\mathbf{x}_\Gamma) = \int_V \mathbf{f}_\Gamma(x)\ \delta[(\mathbf{x}-\mathbf{x}_\Gamma)\cdot\hat{\mathbf{n}}_\Gamma]$$

In case of the boundary thickness $l \to 0$ the Delta function can be expressed in terms of the norm of the gradient of the VOF function f:

$$\begin{aligned} f(x) &= H[(\mathbf{x}-\mathbf{x}_\Gamma)\cdot\hat{\mathbf{n}}_\Gamma] \\ \nabla f(x) &= \delta[(\mathbf{x}-\mathbf{x}_\Gamma)\cdot\hat{\mathbf{n}}_\Gamma]\cdot\hat{\mathbf{n}}_\Gamma \\ |\nabla f(x)| &= \delta[(\mathbf{x}-\mathbf{x}_\Gamma)\cdot\hat{\mathbf{n}}_\Gamma] \quad . \end{aligned}$$

Here, H is the Heaviside step function. Since the f-function requires to have a finite gradient in a distance l of the transition area, the function is artificially daubed during discretization over serval cells. Therefore, the volume force results as

$$\int_A \mathbf{f}_{\Gamma,V}(\mathbf{x}) dA = \sigma \kappa_\Gamma \nabla f(\mathbf{x}) \ , \tag{3.4}$$

with the local (principal) curvature of the interface given by $\kappa_\Gamma = -\nabla \cdot \hat{\mathbf{n}}_\Gamma$. Here, $\hat{\mathbf{n}}_\Gamma$ denotes the unit normal vector at the interface with $\hat{\mathbf{n}}_\Gamma = \mathbf{n}_\Gamma / |\mathbf{n}_\Gamma|$. Using the finite-difference-discretization of eq. (3.4) results in contributions from the boundary of the transition area of that interface. Since the values of the density are saved inside the cell's center, an indirect differentiation of the normal vector causes an improve in numerical approximation. For it, a transformation in calculating the curvature is necessary (with $\mathbf{n} = \mathbf{n}_\Gamma$):

$$\kappa = \frac{1}{|\mathbf{n}|} \left[\nabla \cdot \mathbf{n} - \left(\frac{\mathbf{n}}{|\mathbf{n}|} \cdot \nabla \right) |\mathbf{n}| \right] \ . \tag{3.5}$$

The main disadvantage of the CSF model described before is its non-conservative character. Due to this manner the conservation of momentum cannot be guaranteed, eventually causing non-physical effects during numerical simulation. Therefore, a conservative model has been developed by Lafaurie *et al.* (1994) eliminating such problems. The approach develops the discrete form of conservative capillary forces by applying the same approximation of ∇f to calculate the normal vector and the density of the boundary layer. Thus, the volume-specific capillary force $\mathbf{f}_{\mathrm{st}}$ result as:

$$\mathbf{f}_{\mathrm{st}} = -\sigma \nabla \cdot \left[\frac{\mathbf{n} \otimes \mathbf{n}}{|\mathbf{n}|} - \mathrm{I} \, |\mathbf{n}| \right] \ .$$

Using the quotient rule on this equation gives

$$\mathbf{f}_{\mathrm{st}} = -\sigma \ \left[\frac{\mathbf{n}}{|\mathbf{n}|} \left(\nabla \cdot \mathbf{n} - \left(\frac{\mathbf{n}}{|\mathbf{n}|} \cdot \nabla \right) |\mathbf{n}| \right) + \left(\frac{\mathbf{n}}{|\mathbf{n}|} \cdot \nabla \right) \mathbf{n} - \nabla |\mathbf{n}| \right] \ . \tag{3.6}$$

The latter conservative formulation of capillary forces differs from the non-conservative form of eq. (3.5) by the two additional terms in eq. (3.6). The numerical simulations of free surface flow with *FS3D* conducted throughout this project are carried out using the conservative approach of Lafaurie *et al.* (1994).

3.4.2. Numerical Implementation of the Surface Forces

As mentioned previously, the calculation of the flow variables inside the VOF code is based on the MAC method. Thus, the spatial discretization of these parameters occurs on a staggered grid inside each control volume. Therefore, the pressure p and the volume fraction f are saved in the cell's centroid, whereas the velocity components u,v,w are stored on the cell's face and the normal vector $\mathbf{n}$ at the corner of the volume element $dV = dx\,dy\,dz$ (cf. Figure 3.4).

Surface forces $\mathbf{f}_{\mathrm{st},i,j,k}$ are also calculated inside the cell centroid for the three directions in space. Therefor, a conservative model of Lafaurie *et al.* (1994) is applied solving the Navier-Stokes equations using staggered finite differences on a MAC grid for spatial discretization and a split-explicit time differencing schema. For it, normal vectors are necessary derived by averaging the normal vectors from the corners of the control volume. These normal vectors at the corners are calculated as $\mathbf{n} = \nabla f$ using the marker function f with respect to the 27 adjacent cells.

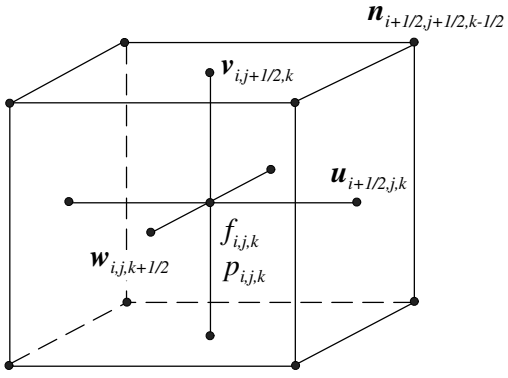

Figure 3.4.: Staggerd alignment of the flow variables according to the MAC method.

3.4.3. Parasite Currents

A problem during numerical calculation of free fluid surfaces are 'parasite currents'. These unavoidable flows are a result of the locality of the method of Brackbill *et al.* (1992) and Lafaurie *et al.* (1994) since curvature κ_Γ and normal vector $\mathbf{n}_\Gamma$ are calculated insufficient at the interface. Therefore, these imprecisions cause non-physical effects which may deform a bubble or even cause disintegration. Even a macro-

scopically static bubble is surrounded by a small amplitude velocity field due to the slight unbalance between the stresses at the sites in the interfacial region. Such parasitic currents are absent on flat interfaces parallel to the grid axes or make a 45° angle with them. However, they are found for a generic orientation of a flat interface with respect to grid direction inducing artificial swirls at the interface of the bubble. In general parasitic currents scale with surface tension and viscosity. As could be shown by, e.g., Lafaurie *et al.* (1994); Scardovelli & Zaleski (1999) using dimensionless analysis, the maximum velocity around a bubble of radius R is determined as $\mathbf{u}_{pc} = C\,\sigma/\eta_d$ with C being the dimensionless magnitude. Numerical experiments based on empirical approaches verify this law with $C \simeq 10^{-2}$. Lafaurie *et al.* (1994) further found a proportionality between the dimensionless radius R/R_v ($R_v = \rho_d \nu_d^2/\sigma$) and the Reynolds number based on parasitic current velocity and bubble size $\mathrm{Re}_{pc} = \mathbf{u}_{pc} R/\nu$. Here, R_v characterizes the capillary-viscous length scale of the fluid. With increasing Re_{pc} number the fluctuations of parasitic currents will increase as well eventually causing the interface to disintegrate. Instead, for very small values of R/R_v capillary effects should be negligible so that parasite currents cause little effect since the dynamics are controlled by viscous forces.

Lafaurie *et al.* (1994) were able attenuate parasite currents by smoothing the volume fraction *f*. The smoothing was realized by a repeated application of a Laplacian filter to finally reduce the amplitude of parasite currents by a factor of 2 or 4. Instead, *FS3D* uses a quadratic smoothing method to attenuate parasite currents. Furthermore it was found that even the grid resolution applied for numerical simulation of liquids strongly influences the magnitude of physical imprecisions. Reipschläger *et al.* (2002) and Koebe (2004) performed quantitative experiments investigating the temporal evolution of the kinetic energy inside the computational domain regarding the grid resolution. They were able to approve a relationship between parasite currents and grid resolution, but could not observe a specific trend. Concluding, a concrete prediction whether or not parasite currents scale with grid resolution is not possible.

In general, parasite currents appear for systems of high surface tension and high density discrepancies. This is especially significant for droplets of small radius, when the surface tension is large compared to its viscosity (Scardovelli &

Zaleski, 1999). In such cases either the capillary number $\mathrm{Ca} = \mu|\mathbf{u}|/\sigma$ is small or the Laplace number $\mathrm{La} = \sigma\rho R/\mu^2$ is large, respectively. According to numerical experiments there were no physical instabilities found for small Ca and moderate La. The only troublesome effect were parasite currents. Instead, if the La increased even parasite currents grow as well and could even become large enough to destroy the interface. This behavior is explained by the relationship between Re and La as

$$\mathrm{La} = 100\ \mathrm{Re}_{pc}\ .$$

In practice, parasite currents turned out to be significant in computation when $\mathrm{La} \sim 10^6$. This is approximately the value for droplets of 1 cm in diameter marking the minimum size of droplets to be accurately simulated. Since our study deals with droplets of about 2.2 cm and lamella of about 4 cm in diameter in numerical simulation of the disintegration process, parasite currents need to be rated by comparing surface tension and inertia. At small Weber numbers, $\mathrm{We} = \rho_g u_{rel}^2 d/\sigma$, capillary tension dominates inertial phenomena. Since this happens for smaller droplet diameter, parasite currents may have an influence on the deformation processes during simulation in an SWL. Here, the Weber number is less than $\mathrm{We} \leq 10$ (see Chapter 5.2). However, in case of an ultrasonic standing wave field the energy input of the ultrasonic field into the system is dominant. Especially for the disintegration of a continuous liquid strand, Weber numbers of $\mathrm{We} > 60$ are achieved, so that parasite current should be of no importance. For more details about parasite currents and possible solution see Rudman (1998); Jacqmin (1996); Meier *et al.* (2000) and Jamet *et al.* (2002).

3.5. Coupling of the Numerical Tools

To consider the force input of the ultrasonic field on the disperse phase, a coupling of the numerical simulation tools is necessary. Therefore, the VOF method for simulation of the free surface flow is extended by source terms. These source terms act on the liquid phase boundary modeling the momentum flux of the oscillating sound field on the disperse phase. The basic approach of modeling the surface forces are the jump conditions introduced in Chapter 2.4. The main assumption of this approach is that the acoustic forces solely act on the liquid surface because of the huge acoustic impedance between gas and disperse phase. Therefore, only

an insignificant amount of the ultrasonic field impinges into the liquid phase. This approach is proven by numerical simulation of pressure and velocity fields including a liquid obstacle. Finally, back-effects of the disperse phase onto the sound field are neglected in terms of the continuous strand disintegration. In case of the deformation of liquid droplets the interaction between drop and ultrasonic field could be studied using *Fluent*. Therefor, sound fields disturbed by a liquid obstacle are read into *FS3D*. Further interactions between sound field and disperse phase varying the ultrasonic field inside *FS3D* have not been realized so far.

3.5.1. Modeling of the Interfacial Source Terms

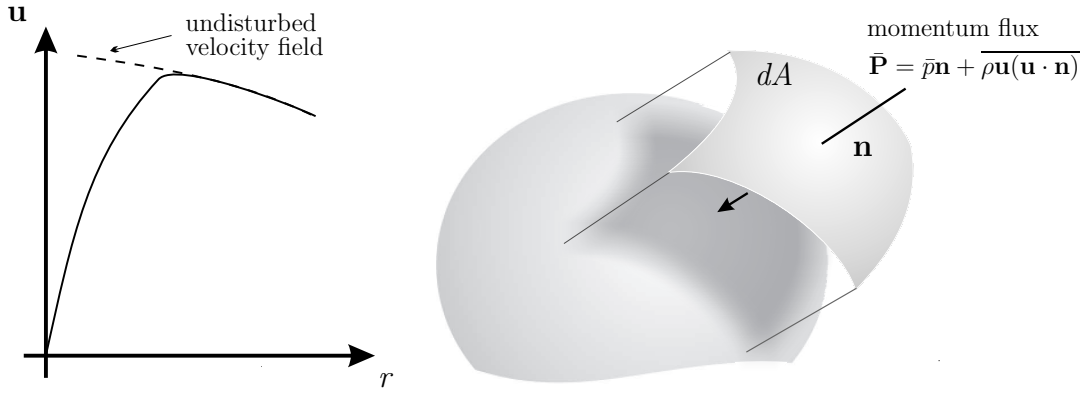

(a) (b)

Figure 3.5.: a) Schematic profile of the normal component of the relative velocity **u** inside the continuous phase versus the normal distance r to the interface $\Gamma(t)$.
b) Momentum flux through a face dA parallel to the interface.

Ultrasonic forces acting on the liquid surface are taken into account by a one-way coupling of the two numerical methods. For this purpose, additional interfacial source terms are incorporated into the momentum jump conditions, which model the flux of momentum into the liquid due to acoustic forces. Pressure and velocity fields needed for the computation of source terms are obtained from the compressible flow computations with *CFX* or *Fluent*, respectively. Initially, back-effects of the dispersed phase onto the sound field are neglected. More precisely, the following approach is used for calculation of the interfacial source terms (cf. Figure 3.5 a&b).

If the back-effects are small, the velocity inside the gas phase relative to the liquid phase will change within a thin boundary layer from zero at the interface due to no-slip conditions to values that equal those in an unperturbed situation at points close to the interface. Since dissipation inside the gas phase is negligible because of small viscosity, the momentum flux across the phase boundary is approximately given by the flux of momentum through the slightly shifted face that is situated in the gas phase parallel to the original one. Thus, he resulting momentum flux is given by the acoustic pressure

$$\mathbf{P} = p\mathbf{n} + \rho(\mathbf{u} \otimes \mathbf{u}) \cdot \mathbf{n} = p\mathbf{n} + \mathbf{u}(\mathbf{u} \cdot \mathbf{n}) \,.$$

Because of the high inertia of the liquid phase compared to the gas phase, droplets do not instantaneously react on every oscillation within the gas phase. Therefore, the force density can be calculated by taking time-averages over an acoustic cycle, i.e.

$$\bar{\mathbf{P}} = \bar{p}\mathbf{n} + \overline{\rho\mathbf{u}(\mathbf{u} \cdot \mathbf{n})} \tag{3.7}$$

with the mean value of a quantity ϕ given by $\bar{\phi}(t,x) := \frac{1}{T}\int_t^{t+T} \phi(s,x)\, ds$, with appropriate $T > 0$. These time-averaged pressure and velocity values are calculated during the CFD simulations of the sound field with *CFX* or *Fluent*, respectively. The average density of the momentum flux is then incorporated as a source term on the right-hand side of the second formula in (2.13). Furthermore, because of different grid resolutions, the flow fields obtained in two dimensions assuming rotational symmetry are interpolated and transformed to Cartesian coordinates, before being read as source terms into *FS3D*.

3.5.2. Numerical Implementation of the Interfacial Source Terms

The assumptions derived in Section 3.5.1 characterize the impact of the ultrasonic field on the disperse phase as an averaged momentum flux through a face parallel to the phase boundary. Therefore, the ultrasonic force needs to be added onto the overall balance of forces at the interface. Hence, surface forces need to be transformed to volume forces acting inside the transition area of the phase boundary.

According to eq. (3.7) the term $\overline{\rho\mathbf{u}\otimes\mathbf{u}}$ displays a symmetric matrix with entries for the three coordinates in space:

$$\overline{\rho\mathbf{u}\otimes\mathbf{u}}\cdot\mathbf{n}=\left\langle\begin{pmatrix}\rho uu & \rho uv & \rho uw\\ \rho uv & \rho vv & \rho vw\\ \rho uw & \rho vw & \rho ww\end{pmatrix}\right\rangle\begin{pmatrix}n_x\\ n_y\\ n_z\end{pmatrix},$$

where u,v and w denote the components of the velocity vector $\mathbf{u}$ with respect to the Cartesian coordinates in space x,y,z and $\langle\cdot\rangle$ the time average. The components required for the calculation of the symmetric matrix are derived in conjunction with the pressure $\overline{p}$ inside the *CFX* and *Fluent*-code, respectively. Since ultrasonic fields are calculated assuming rotational symmetry, averaged data fields $\overline{\rho u_x u_x}$,$\overline{\rho u_x u_r}$ and $\overline{\rho u_r u_r}$ need to be transformed to Cartesian coordinates, before being read as source terms into *FS3D*. For the simulation of droplet deformation and strand disintegration the coordinate system is chosen in such way that the x-axis of *CFX* or *Fluent*, respectively, are congruent with the setup in *FS3D*. Further, the calculation domain of the droplet is made up of two symmetry planes (xy- and xz-plane), whereas the simulation of the continuous strand disintegration requires one symmetry condition as the xz-plane. Therefore, the center of a simulated droplet is located on the x-axis (cf. Figure 3.6).

In case of droplet deformation and strand disintegration the chosen symmetry causes the six entries of the symmetric matrix to be

$$\begin{aligned}
\overline{\rho uu} &= \overline{\rho u_x u_x}\\
\overline{\rho uv} &= \overline{\rho u_x u_r}\cdot\tfrac{y}{r}\\
\overline{\rho uw} &= \overline{\rho u_x u_r}\cdot\tfrac{z}{r}\\
\overline{\rho vv} &= \overline{\rho u_r u_r}\cdot\tfrac{y^2}{r^2}\\
\overline{\rho vw} &= \overline{\rho u_r u_r}\cdot\tfrac{yz}{r^2}\\
\overline{\rho ww} &= \overline{\rho u_r u_r}\cdot\tfrac{z^2}{r^2},
\end{aligned}$$

with $r=r(y,z)=(y^2+r^2)^{1/2}$.

The force $\mathbf{f}_{\mathrm{st}\,i,j,k}$ due to surface tension is calculated in *FS3D* inside the center of a grid cell (Section 3.4.2). Likewise the calculation of the source terms is done for the cell's center. Therefore, according to Figure 3.4 the normal vectors need to be interpolated from the corners of the grid cell to its center. Thereby, the normal

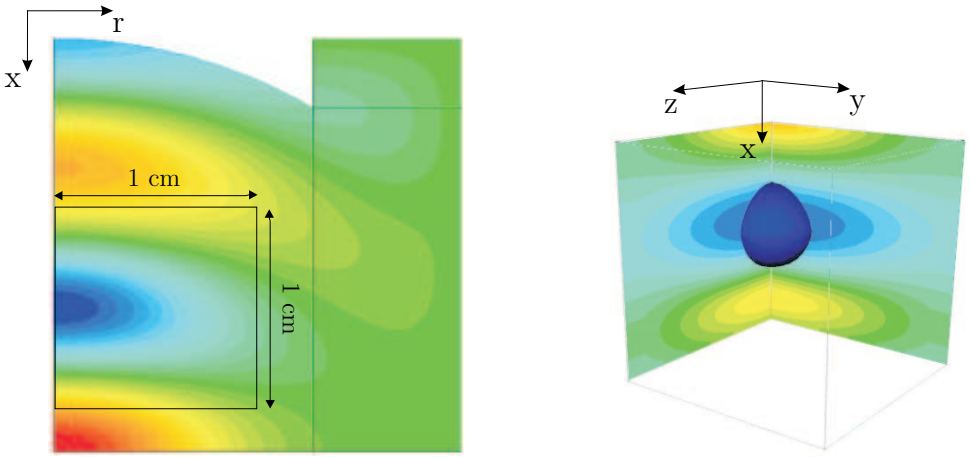

(a) *CFX / Fluent* (b) *FS3D*

Figure 3.6.: Position of the interpolation and symmetry areas in *CFX/Fluent* and *FS3D*.

vectors point in the direction of the phase with $f = 1$. Therefore, in case of the simulation of the disperse phase in air these vectors point into the liquid phase. Concluding, the source terms f_Q inside the cell's center of the grid cell i, j, k for the three coordinates result as:

$$\begin{aligned} f_{Q_x} &= \overline{p}\, n_{cx} |\nabla f| + (\overline{\rho u u}\, n_{cx} + \overline{\rho u v}\, n_{cy} + \overline{\rho u w}\, n_{cz})\, |\nabla f| \\ f_{Q_y} &= \overline{p}\, n_{cy} |\nabla f| + (\overline{\rho u v}\, n_{cx} + \overline{\rho v v}\, n_{cy} + \overline{\rho v w}\, n_{cz})\, |\nabla f| \\ f_{Q_y} &= \overline{p}\, n_{cz} |\nabla f| + (\overline{\rho u w}\, n_{cx} + \overline{\rho v w}\, n_{cy} + \overline{\rho w w}\, n_{cz})\, |\nabla f| \,. \end{aligned}$$

The mandatory transformation of surface forces into volume forces is done by multiplication with $|\nabla f|$. The values of $n_c |\nabla f| = \nabla f$ with respect to the required grid cell are also needed for the calculation of the normal vector. Therefore, they are already calculated in a subroutine of *FS3D*. Finally, the source terms are added to the corresponding surface force of each local coordinate. In case of the x-coordinate for cell (i,j,k) it results:

$$f_{\mathrm{st}\,x} = f_{\mathrm{st}\,x} + f_{\mathrm{Q}\,x}$$

For the y- and z-coordinate corresponding equations occur.

4. Ultrasonic Standing Wave Fields

The acoustic denotes the propagation of local density fluctuations in a medium as sound. Thereby, it is does not matter if this medium is a fluid, specifically meaning gas or liquid systems, or a solid. According to the frequency spectrum sound is separated into:

subsonic noise:	frequency domain of 0.01 Hz - 15 Hz
acoustic noise:	frequency domain of 16 Hz - 20 kHz
ultrasound:	frequency domain of 20 kHz - 10 GHz
hypersound:	frequency domain of 10 GHz - ∼10 THz

The propagation of sound waves occurs in solid media as longitudinal or transversal waves. Instead, elastic thrusts are missing in fluids which are necessary for the transfer of transversal waves. Therefore, in liquids and gases only longitudinal waves are found (Meyer & Neumann, 1979).

Ultrasound is generated by mechanical sound generators like whistles, sirens, electro-magnetic, and piezo electric transducers. Because of ultrasound having of comparable short wave length - smaller than 20 mm in air - focusing of its energy is relatively easy. This leads to high local sound intensities including magnificent energy densities. The technical benefit of ultrasonic fields is based on especially this high energy density.

The applications of the ultrasonic technique are principally subdivided into three parts:

- ultrasonic gas atomizer
- ultrasonic capillary wave atomizer
- ultrasonic standing wave atomizer

The ultrasonic gas atomization is known since the beginning of the 20th century and successfully used in industry. The process is based on Hartmann's shock wave generator. A gas is exited to high frequency oscillations in a resonance chamber while exposing it to high pressure. Afterwards, the gas is conducted to a molten strand of the required material resulting in the disintegration of the strand into droplets. Although the process is highly efficient, it is also characterized by a huge consumption of gas (Meng, 1997).

During ultrasonic capillary wave atomization an ultrasonic field is generated by the means of mechanical movements of a piezo ceramic. The liquid to be atomized is directly placed on the surface of the oscillation unit, leading to a thin liquid film on the sonotrode's face. Subsequently, capillary waves are formed on the liquid's surface caused by Langevin's acoustic radiation pressure. Due to this pressure the film will then disintegrate into single droplets causing an atomized spray (Pohlmann & Stamm, 1965; Lang, 1962; Gießhammer & Lierke, 1968). Hence, the process is limited to low viscose liquids or melts having a low melting point.

Ultrasonic standing wave atomizers (SWA) are based on the containerless disintegration of liquids in the central pressure node of a resonant ultrasonic field. Therefore, they are even summarized as "containerless processing". Their use is wide spread in industry e.g., as ultrasonic nozzles, humidifier in households, for the atomization of metals, or the disintegration of polymers. In general, the SWA-technique is only used for very specific tasks and mainly not optimized for that application. The ultrasonic field generated in an SWA, which acts on the inserted liquid and leads to its disintegration, is subsequently discussed in more detail.

4.1. Previous Investigations

The beginning of the SWA-technique is based on levitator experiments extensively investigated by the European and American Space Agencies, ESA and NASA. They were interested in containerless processing of samples under microgravity conditions (Lierke, 1996). In a single-axis standing wave levitator (SWL) acoustic forces balance an inserted sample against gravity between a sound source and a reflector, if the applied sound field is strong enough. Using a liquid as the investigated sample, an increase of the sound amplitude causes flattening and final breakup of the fluid

(Danilov & Mironov, 1992; Andersen, 1996).

Lierke & Ruckdeschel (1976) realized that this technique could evenly be used for the continuous disintegrations of melted, liquid metals to produce powders and pellets. At this early stage of the SWA-technique, Lierke and Ruckdeschel describe their disintegration process of a continuous liquid strand based on one active, oscillating transducer and an opposite static reflector corresponding to an SWL. In later patents Lierke *et al.* (1978, 1987) extends this technique to the general use of arbitrary fluids and additionally converted the static, plane reflector into a second oscillating transducer unit. This approach further more has the advantage of the sonotrodes being self-cleaning by the vibrational movements of both sonotrodes.

Based on these perceptions systematical investigations and developments were done at the *Institut für Werkstofftechnik* (*IWT*) in Bremen. The research group of Bauckhage *et al.* focused on the investigation of metals and glasses (see Reich, 1995; Li, 1996; Andersen, 1996; Meng, 1997), but also expanded the SWA-technique from liquid metals to highly viscous materials. For this purpose, the acoustic energy density inside a central pressure node was increased by the application of concave sonotrode end faces during the 1990th resulting in an improved disintegration of liquids (Bauckhage, Schreckenberger & Vetters, 1989).

Especially Li (1996) extensively characterized the ultrasonic field in an SWA qualitatively and quantitatively. Using the non-linear wave theory Li (1996) was able to explain the appearance of sound waves: For waves having an finite amplitude the propagation velocity depends on the instantaneous velocity $\mathbf{u}(x,t)$ and on the medium (characterized by isentropic exponent κ). Therefore, it might happen that the wave front having a positive particle velocity - propagating faster - passes the one with a negative particle velocity. Thus, a deformation of the wave front results which itself depends on the distance to the sound source. Sutilov (1984) characterized this typical form as tooth-like and the corresponding wave as a shock-wave.

The deformation of sound waves caused by higher harmonic oscillations is equivalent to the description of Li (1996). Beside the fundamental frequency ω, depending on the sonotrode movement, higher harmonics occur. These intensify

during the propagation process at the expense of the fundamental noise. Li (1996) stated that there is a broad theory about the appearance of shock waves to predict their occurrence. Instead, an explicit mathematical solution of these shock-waves based on sound characteristics is so far not possible. Li (1996) was able to approve these theoretical approaches by measuring the pressure field in an SWA regarding the non-linear effects of the sound field. He found almost sinusoidal oscillations near the sonotrodes face having the exiting frequency of the transducer. Increasing the distance to the sonotrode leads to a strong deformation of these waves with higher harmonics getting more dominant. Concluding, Li (1996) described the ultrasonic wave field as the sum of two standing waves depending on the fundamental frequency ω_1 and the frequency ω_2 of the first higher harmonic wave:

$$p = p_1(x) \sin \omega_1 t + p_2(x) \sin 2\omega_2 t$$

However, Li (1996) only used this perception for a better understanding of the SWA-technique instead of deriving models describing the disintegration process.

4.2. Theory on Sound Acoustics

Acoustic sound fields are of strong non-linear nature. Their sound waves are rather divergent having a finite width with the amplitude varying over the acoustic beam cross section and continuously decaying on the beam edges. Instead, the ultrasonic piston of an acoustic resonator is often theoretically simplified to generate plane waves. These are assumed to be an uniform "top hat" wave with abruptly decaying amplitudes at the edges of the wave. This approach is mainly used in literature and subsequently presented in more detail.

4.2.1. Linearization of the Wave Equation

Sound waves are characterized by spatial and temporal fluctuations of the density ρ, the particle velocity $\mathbf{u}$, and the pressure p around a constant value:

$$\begin{aligned} \rho &= \rho_0 + \rho_\sim \\ \mathbf{u} &= \mathbf{u}_0 + \mathbf{u}_\sim \\ p &= p_0 + p_\sim \ . \end{aligned} \tag{4.1}$$

Here, ρ_0, $\mathbf{u}_0$, and p_0 denote the constant values of the fluid in equilibrium. The

variable quantities of the sound field are indicated as excess density $\rho_\sim$, velocity $\mathbf{u}_\sim$, and pressure $p_\sim$. Notice also, that the sound-particle velocity needs to be distinguished from the sound-propagation velocity of the ultrasonic field. The latter one depends on the specific propagation medium and, therefore, the sound speed in air becomes 343 m/s at standard conditions. The fundamentals of sound propagation are the transport equations of mass (2.5) and momentum (2.7) previously discussed in Chapter 2.

For linearization of these basic equations fluctuations of the physical quantities are assumed to be small compared to the quiescent state (Meyer & Neumann, 1979). Therefore,

$$\triangle p << p_0 \quad \text{and} \quad \triangle \rho << \rho_0$$

needs to be valid. In this case the non-linear terms of the transport equations can be neglected, if further more losses caused by dissipation are unconsidered. Hence, the viscosity stress tensor T, the convective acceleration $(\mathbf{u}\nabla)\mathbf{u}$ as well as the non-linear fraction of the local acceleration cancel out. Inserting eq. (4.1) into the resulting transport equations leads to the following expressions:

$$\frac{\partial}{\partial t}\rho_\sim + \rho_0 div\mathbf{u} = 0 \ ,$$
$$\rho_0 \frac{\partial \mathbf{u}}{\partial t} + \nabla p_\sim = 0 \ .$$

The vector of the velocity can be expressed by a scalar quantity, introducing a velocity potential as $\mathbf{u} = \nabla\varphi$. Therefore, the continuity equation becomes

$$\frac{\partial}{\partial t}\rho_\sim + \rho_0 div(\nabla\varphi) = 0 \ , \quad \triangle\varphi = \frac{1}{\rho_0}\frac{\partial \rho_\sim}{\partial t} \ , \tag{4.2}$$

and the momentum equation can be displayed as

$$\nabla p_\sim = \rho_0 \frac{\partial}{\partial t}(\nabla\varphi), \quad p_\sim = \rho_0 \frac{\partial \varphi}{\partial t} \ .$$

In order to solve the mathematical system, a correlation is necessary describing the interrelationship between pressure and density. Assuming state changes in an ultrasonic wave proceeding very fast and, therefore, temperature adjustments with

the environment not taking part, the isentropic equation can be used:

$$\frac{p}{p_0} = \left(\frac{\rho}{\rho_0}\right)^{\kappa} .$$

Here, the isentropic exponent $\kappa = c_p/c_v$ denotes the relationship between the specific heat capacity at constant pressure and constant volume. Because of the density being a function of pressure, the derivation $\partial\rho/\partial t$ can be expressed as follows in the mass balance:

$$\frac{\partial\rho}{\partial t} = \left(\frac{\partial\rho}{\partial p}\right)_0 \frac{\partial p}{\partial t} .$$

By differentiation of the impulse equation, the derivation $\partial p/\partial t$ results as

$$\frac{\partial p}{\partial t} = \rho_0 \frac{\partial^2\varphi}{\partial t^2} .$$

Inserting these two equations into the mass balance (4.2) leads to the fundamental wave equation in acoustics

$$\triangle\varphi = \frac{1}{c_0^2}\frac{\partial^2\varphi}{\partial t^2} , \tag{4.3}$$

having the propagation velocity of an infinite small amplitude

$$c_0^2 = \left(\frac{\partial p}{\partial\rho}\right)_S .$$

The speed of sound c_0 can finally be calculated using the ideal gas law, $p\mathrm{V}{=}R\mathrm{T}/M$, including the gas constant R and the molecular weight M as

$$c_0 = \sqrt{\kappa R T} .$$

If the velocity potential is only based on one coordinate, the wave equation mirrors the *plane wave solution* of an ideal, one-dimensional wave. This solution arises from the classical model of Kundt's tube. For this purpose, it is assumed that the diameter of the tube is clearly smaller than the exited wave length. This is the basic equation used for the description of propagating waves in acoustics.

Regarding specific boundary conditions one solution of eq. (4.3) is the sinus function. Therefore, problems based on the linearized approach can always be

ascribed to the sinus function. This is the attempt generally used in literature to calculate ultrasonic fields and, therefore, comparing results achieved during this project with data from different groups is difficult.

4.3. Plane Waves of Small Amplitude

Sound waves are assumed to be monochromatic waves whose quantities are entirely an ordinary function of time. If the sound generator is oscillating with an angular frequency ω, the velocity potential derives in a complex formulation,

$$\varphi(x,t) = \Re\left\{\varphi_0(x)e^{i\omega t}\right\} \ ,$$

with $\Re$ denoting the real part and φ_0 the amplitude of the velocity potential at $t = 0$. Inserting this term into the wave equation (4.3), the so called one-dimensional *Hemholtz* equation results:

$$\frac{\partial^2\varphi_0(x)}{\partial x^2} + k^2\varphi_0(x) = 0. \tag{4.4}$$

Here, $k = \omega/c_0$ denotes the wave number including the angular frequency ω. A special solution of eq. (4.4) for a wave propagating in positive x-direction and having an initial phase of zero is

$$\begin{aligned} &\varphi(x,t) = \varphi_{max}e^{i(\omega t - kx)} \quad \text{and} \\ &\varphi(x,t) = \varphi_{max}\sin(\omega t - kx) \ , \text{respectively,} \end{aligned} \tag{4.5}$$

with φ_{max} as the maximum amplitude of the velocity potential and x as the distance of the propagating wave from its source. Further, the angular frequency ω can be derived in dependency of the sound frequency f as $\omega = 2\pi f$. The local phase change of the wave of 2π proceeds on a distance of $\lambda = c/f$, with λ denoting the wave length.

Because of the linearization of the equation as described previously, it is only exactly valid in case of sound waves of infinitesimal small amplitude. Instead, real sound waves are of a finite amplitude which can build up due to resonance phenomena. As pointed out by Lierke & Großbach (1983), especially nonlinear effects have an important impact on the disintegration process in an ultrasonic field. According to Lierke & Großbach (1983), there is a strong influence of nonlinear effects

on the sound field for acoustic Mach numbers (Ma) $> 10^{-2}$, with Ma giving the ratio of linear velocity and sound velocity in a fluid (Ma $= \mathbf{u}_{max}/c_0$). As could be calculated in numerical simulations of a 45 μL droplet in an ultrasonic standing wave levitator, Ma $= 2.8 \cdot 10^{-2}$ at a transducer amplitude of 5.21 μm results (see Chapter 5 for more details). Therefore, non-linear effects do have an important impact on droplet deformation as well as on strand disintegration. Hence, mass and momentum balance have to be solved regarding the nonlinear terms of the sound field to quantitatively describe the atomization processes.

4.4. Plane, Standing Waves of Small Amplitude

If two plane waves propagate opposite to each other having the same amplitude and frequency in a *boundless* environment, a standing wave results. Mathematically, such a standing wave is defined as the sum of two waves propagating in positive and negative direction. In one dimension, the following equation results according to eq. (4.5):

$$\varphi(x,t) = \varphi_1 \sin(\omega t - kx) + \varphi_2 \sin(\omega t + kx)$$

A special aspect about standing waves is the temporal fluctuation of the acoustic properties with respect to their spatial position. These acoustic properties are subsequently discussed for plane, standing waves in a *restricted* area.

4.4.1. Oscillation-Reflection Unit

For experimental as well as numerical investigations of droplets in an ultrasonic wave field, ultrasonic standing wave levitators are used. This setup consists of an active, oscillating transducer and a reflector. As a first approximation this oscillation-reflection unit can be described by the classical model of Kundt's tube. Therefore, it is assumed that the reflector is made up of a sound inert material, i.e. having a huge sound resistance. Further, the transducer has to conduct a purely sinusoidal oscillation with an amplitude of Y_0 and the angular frequency ω. The generated sound waves are assumed to be plane waves and, therefore, in this specific case the diameter of the sonotrode has to be smaller than the wave length. In reality, the sonotrode employed is 35 mm in diameter, whereas the wave length of

the sound is about twice as small having approx. 17 mm.

For an ultrasonic standing wave in a restricted area the following boundary conditions apply in case of Kundt's tube:

$$\varphi_{(x=0)} = Y_0 \sin(\omega t) \quad \text{and } \varphi_{(x=L)} = 0 \ , \tag{4.6}$$

with L denoting the distance between the sonotrode's surface and the resonator, and Y_0 the oscillation amplitude in comparison to its rest position. According to Arsenin (1968), one solution of this set of equations is

$$\varphi(x,t) = \frac{Y_0}{\sin\ kL}\ \sin(L-x)\ \sin(\omega t) \tag{4.7}$$

using the boundary conditions as displayed in equation (4.6) on the fundamental wave equation (4.3). This latter equation (4.7) mirrors the typical shape of a standing wave having oscillation nodes and anti-nodes. But the sound amplitude $\frac{Y_0}{\sin kL}$ is not solely based on the acoustic source. It also depends on the distance L between sonotrode and reflector. For values of

$$kL\ = n\pi \quad \text{(n=1,2,3, ...)} \quad \text{or} \quad L = n\lambda/2 \ , \tag{4.8}$$

respectively, it gets infinite. This case is called the resonance condition or L being the resonance length L_r.

4.4.2. Twin-Oscillation Unit

The experimental setup used for the disintegration in an ultrasonic standing wave field consist of a second, active transducer instead of a reflector. Thereby, it can further be distinguished if both transducer units oscillate with the same frequency or if there is a frequency shift between them. Mathematically, the latter condition is a special case of the first one. Additionally, it is distinguished between sonotrodes which oscillate in phase or with a phase shift.

Sonotrodes Oscillate in Phase

If both transducer units oscillate without any phase shift, the following boundary conditions need to be employed:

$$\varphi_{(x=0)} = Y_1 \sin(\omega_1 t) \quad \text{and} \quad \varphi_{(x=L)} = Y_2 \sin(\omega_2 t) \ . \tag{4.9}$$

The solution of the wave equation (4.3) regarding the latter boundary conditions (4.9) will than result in

$$\varphi(x,t) = \frac{Y_1}{\sin k_1 L}\ \sin(L-x)\ \sin(\omega_1 t) + \frac{Y_2}{\sin k_2 L}\ \sin\left(k_2 x\right)\ \sin(\omega_2 t)\ . \tag{4.10}$$

Obviously, both addends mirror a single standing wave. This is based on the fact that a sound source acts as a rigid reflector for an opposite transducer unit, although it is itself performing constant oscillations. If the transducers are operated with a frequency shift, beats will occur resulting in a periodic oscillation of the amplitude of such beats. This amplitude varies between two extremes: zero (erasure) and $2 \cdot Y$ (summation), with an angular frequency of $\triangle\omega$. Therefore, the resonant lengths will be found at $L_{r,1} = n\lambda_1/2$ and $L_{r,2} = n\lambda_2/2$. Simplifying, the average wave length is used more generally to determine the overall resonance length of the system. Hence, the mean resonance length $\bar{L}_r$ implying a ceratin quantity of pressure knots N_k is calculated as

$$\bar{L}_r = N_k \cdot \left(\frac{\bar{\lambda}}{2}\right) = N_k \cdot \left(\frac{c}{2\bar{f}}\right)\ . \tag{4.11}$$

Further more, if both transducers oscillate with the same amplitude *and* frequency, equation (4.10) can be simplified as

$$\varphi(x,t) = \frac{Y}{\cos kL/2}\ \sin(\omega t)\ \cos\ k(\frac{L}{2} - x)\ .$$

For this special case, the condition for the resonance length can be derived as

$$L_r = (2N_k - 1) \cdot \left(\frac{\lambda}{2}\right) = (2N_k - 1) \cdot \left(\frac{c}{2f}\right)\ , \quad \text{with } N_k = 1, 2, 3, \ldots\ .$$

Therefore, only for distances between the sonotrodes' faces with an odd multiple of half the acoustic wave length, maximum pressure amplitudes are found. Further on it can be concluded, that only conditions having an odd number of pressure nodes and an even number of pressure anti-nodes, respectively, can be derived (cf. Figure 4.3).

Sonotrodes Oscillate with a Phase Difference

Instead, if both transducers oscillate with a phase shift of 2π, the following boundary conditions result:

$$\varphi_{(x=0)} = Y_1 \sin(\omega_1 t) \quad \text{and} \quad \varphi_{(x=L)} = -Y_2 \sin(\omega_2 t) \; . \tag{4.12}$$

The solution of the wave equation (4.3) regarding the latter boundary conditions (4.12) will than result in

$$\varphi(x,t) = \frac{Y_1}{\sin k_1 L} \sin(L-x) \; \sin(\omega_1 t) - \frac{Y_2}{\sin k_2 L} \; \sin(k_2 x) \sin(\omega_2 t) \; . \tag{4.13}$$

For the special case of equal amplitudes *and* frequencies of both transducers, equation (4.13) can be displayed as

$$\varphi(x,t) = \frac{Y}{\sin kL/2} \; \sin(\omega t) \; \sin \; k(\frac{L}{2} - x) \; .$$

Thus, the condition for the resonance length derives as

$$L_r = N_k \cdot \lambda = N_k \cdot \left(\frac{c}{f}\right) \; , \quad \text{with } N_k = 1, 2, 3, ... \; .$$

Concluding, maximal pressure amplitudes result for resonant distances of even multiples of the wave length. Consequently, just pressure fields with an even number of pressure nodes can be generated.

4.5. Experimental Measurement of the Ultrasonic Field

4.5.1. Experimental Setup of the Pilot Plant

The experimental investigations performed are done at a pilot plant of an ultrasonic standing wave atomizer of the *CTB* as established by Mattern (1998). The generation of the ultrasonic field is done via a frequency synthesizer of the *Branson* company. This synthesizer drives a piezo ceramic with an almost constant frequency of about 20 kHz. The piezo ceramic transforms electrical energy into mechanical movement. The generated amplitude at the ceramic is extended by a booster, attached to the piezo, and a following sonotrode. This overall system is called transducer unit generating amplitudes at the sonotrode's end face up to 125 μm. The maximum amplitude is adjusted by the synthesizer and is kept constant via capacity control. The resulting system made up by the generator and the transducer unit is limited to a certain frequency which can only be varied by exchanging the piezo ceramic.

To extend the sound intensity two opponent transducer units are used (Figure 4.1). Both transducer units oscillate at a fixed frequency and parallelly act as a reflector for the opposite sonotrode. According to eq. (4.11) resonance is achieved at distances L_r of 25.7 mm for a 3-node field and of 42.9 mm for a 5-node field assuming an average sound frequency of 20.05 kHz, a sound velocity of 343.71 m/s, and plane sonotrodes. Both transducers are operated with a distance of half the acoustic wave length in order to achieve an odd number of pressure nodes (see Section 4.4.1). This setup allows the injection of polymer melt into the central pressure node causing an almost circular lamella and less fouling of the sonotrodes' faces due to acoustic streaming (see Section 6.3). These calculated resonance lengths need to be corrected because of the nonlinear nature of the sound field and the concave shape of the employed sonotrodes.

To further more improve the energy density between the sonotrodes, concave sonotrode faces are used. These concave shaped surfaces cause focussing of the emitted sound waves and, therefore, an energy increase in the central pressure node. Empirical investigation of Gazka (1994) show an increase in the pressure am-

plitude inside the central pressure node of up to 100 %. This influence of sonotrode shape on the pressure distribution and, hence, on the disintegration process is discussed in Section 4.7 in more detail.

Finally, to impress an impulse on the trajectory of the generated particles in the sound field the sonotrode angle α is varied according to Figure 4.1. This impulse causes an acceleration of the generated particles out of the sound field in order to minimize fouling of the sonotrodes. Fouling generates bulky particles which separate from the sonotrode's face and, furthermore, an undesired shift in the sonotrode's amplitude due to building up an additional layer on the sonotrode's face.

Sonotrodes used for the operation of the pilot plant and subsequently used for experimental investigations do have a concave face with a diameter D of 35 mm. The concave shape is made of a countersink having a radius of curvature R_c of 35 mm resulting in a spherical calotte of 4.7 mm. Therefore, the adjusted optimal resonance distance X for a 3-node pressure field is experimentally found at 19 mm and at 38 mm for a 5-node pressure field (Mattern, 1998). This corresponds to an inner distance X_i of 28.4 mm and 47.4 mm, respectively. The same approach is used for deriving the optimal distance used for droplet levitation. For investigations in levitator experiments an optimal distance of $L_r = 25.7$ mm is calculated according to eq. (4.8) for a 3-node pressure field resulting in an adjusted distance of $X = 23.3$ mm and $X_i = 28$ mm, respectively.

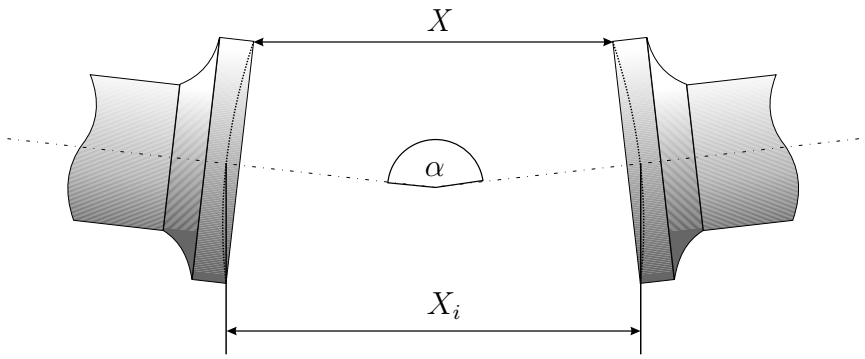

Figure 4.1.: Definition of the sonotrode distance X, the inner distance X_i, and the sonotrode angle α between two transducer units.

4.5.2. Interferometric Investigation of the Ultrasonic Field

Experimental measurements of the acoustic field between two sonotrodes have been performed with a Mach-Zehnder interferometer (Zeiss Com.) at the ITLR in Stuttgart. This tool detects the retardation of a light beam along an optical path crossing the acoustic field compared to a reference beam. Hence, this technique allows for the measurement of integral densities along optical paths in a non-invasive manner. In particular, Mach-Zehnder interferometry is useful for an efficient qualitative characterization of acoustic fields. Figure 4.2 shows several interferometric photographs of the acoustic field in an SWA with concave surface faces for different sonotrode angles and distances. Because density fluctuations in an ultrasonic sound field occur on very short time intervals, only averaged density differences are visualized if a continuous light source is used. The dark regions next to the sonotrodes are caused by high local temperatures. These hot spots occur because the sonotrodes heat up during operation. The photographs in the first row of Figure 4.2 show ultrasonic fields at an optimal resonance distance of $X = 19$ mm for 3 pressure nodes and of $X = 38$ mm for 5 pressure nodes with in-line oriented sonotrodes. Because of the concave shape of the sonotrodes' end faces, especially the outer pressure antinodes are deformed. What results for a 3-node field is an almost homogenous high pressure gradient inside the central pressure node. In radial direction this area of high gradient covers about three quarters of the sonotrodes. For a 5-node field, ellipsoidal contours of the central pressure antinodes between the sonotrodes reduce the region of high pressure gradients. Besides higher pressure field amplitudes, this might be responsible for the smaller size of the particles generated in a 3-node field at the same amplitudes and frequencies. Furthermore, the 3-node field leads to a larger residence time of the polymer in the area of high pressure gradients. This allows for higher flow rates of the liquid during disintegration. Increasing the sonotrode angle leads to larger deformations of the ultrasonic field and to a displacement in radial direction (cf. Figure 4.2). Thereby, the intensity of the ultrasonic field significantly decreases at larger angles. For this reason the angle is usually chosen to be less than 6 degrees.

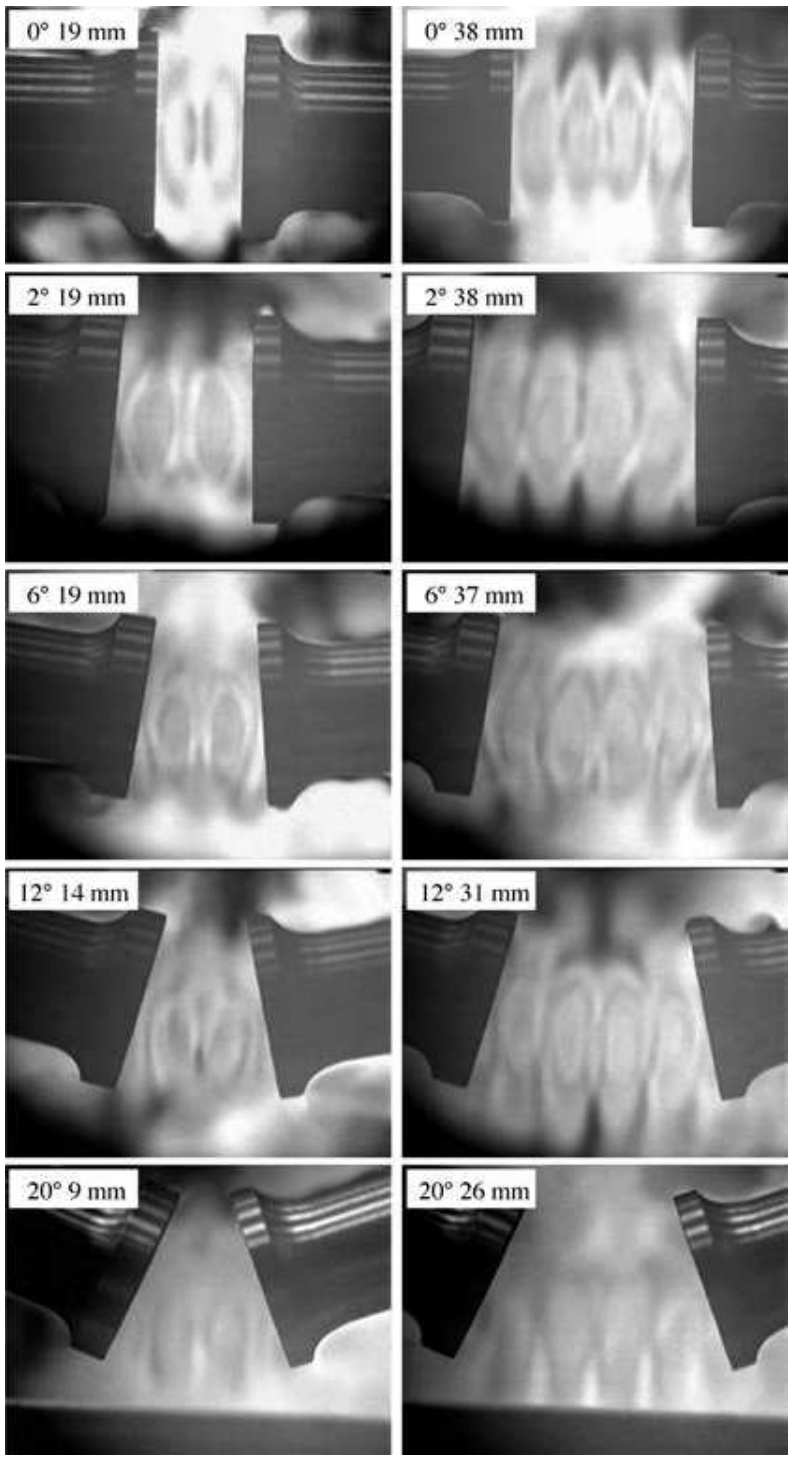

Figure 4.2.: Interferometric photographs of the acoustic field under variations of the sonotrode angles α and distances X (cf. Reipschläger (2002)).

4.6. Numerical Simulation of the Ultrasonic Field

In the experimental setup a twin-oscillation unit with transducer frequencies of 19.9 kHz and 20.13 kHz, respectively, is operated at sonotrode amplitudes of 80 μm. For this configuration numerical simulations were performed with resulting velocity and pressure distributions along the axial direction shown in Figure 4.3. In this case the optimal distance giving resonance with 5 pressure nodes is computed as 37.5 mm which matches the experimental value of 38 mm. Moreover, the simulation captures the complex nonlinear behavior of sound waves causing shifts in amplitudes at high pressure. Because of the increasing influence of higher harmonics, the flanks of the velocity and pressure profiles get strongly steepened leading to sawtooth-like profiles. Pressure nodes, which are sharp at low amplitudes, become wider and diffuse. The calculations are done in 2-D with cylindrical coordinates assuming rotational symmetry. Further more, all simulations performed regarding double oscillation units are performed with a sonotrodes angle of zero degrees.

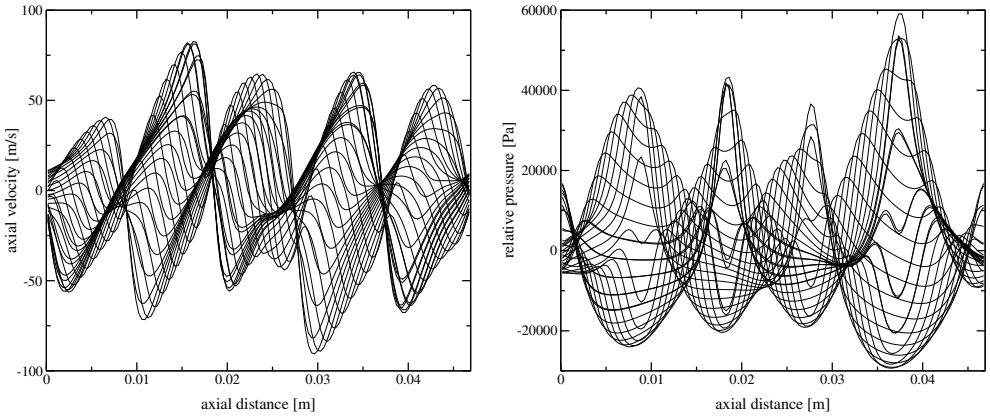

(a) velocity distribution (b) pressure distribution

Figure 4.3.: Numerically computed velocity and pressure distributions at equidistant time-steps for an SWA.

For acoustic levitation of drops much lower amplitudes are required in order to prevent the fluid from immediate disintegration. In case of a 20 kHz sonotrode as an ultrasonic generator and a glass plate as a reflector, resonance is experimentally found at a distance of 23.3 mm, consistent with numerical investigations. For

sonotrode amplitudes of 5.34 μm, the simulated velocity and pressure distributions are shown in Figure 4.4. Since the deformed levitated droplet is still rotationally symmetric, its influence can be taken into account during 2-D computations of the sound field. Thus, interactions between the liquid obstacle and the ultrasonic field can be investigated by means of 2-D axial symmetric simulations.

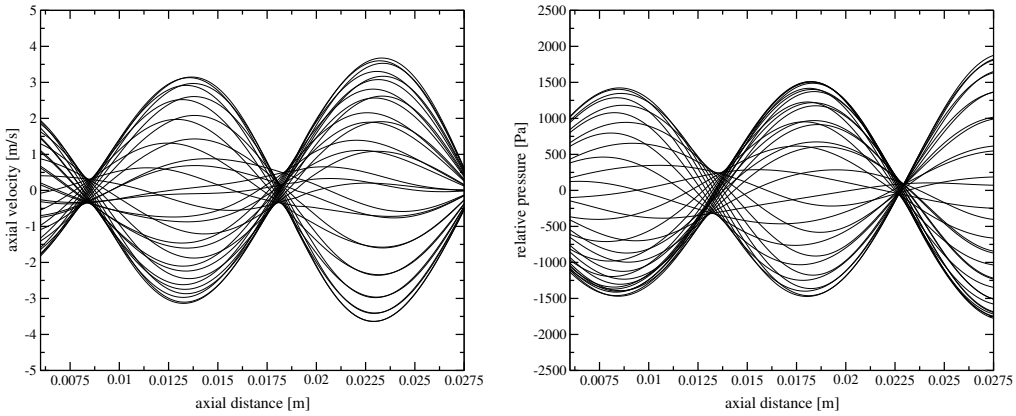

(a) velocity distribution (b) pressure distribution

Figure 4.4.: Numerically computed velocity and pressure distributions at equidistant time-steps for an SWL.

Figure 4.5 shows resulting pressure and velocity distributions caused by a 45 μL droplet placed into a pressure node as a spherical obstacle. As Figure 4.5 illustrates, the back-effect of a single drop on the ultrasonic field is closely localized around the droplet, i.e. perturbations of pressure and velocity are small away from a thin boundary layer. Inside the drop the velocity breaks down to almost zero because of the large density ratio between gas and liquid. Hence, strong velocity gradients close to the phase boundary occur. These phenomena coincide with the assumptions used above to model the gas-liquid momentum flux. This agreement justifies the chosen approach.

As can be seen in Figure 4.5, the pressure field is not that strongly affected by the liquid as it retains the same overall structure. The pressure amplitude is somewhat higher inside the droplet. This can partially be explained by the droplet's

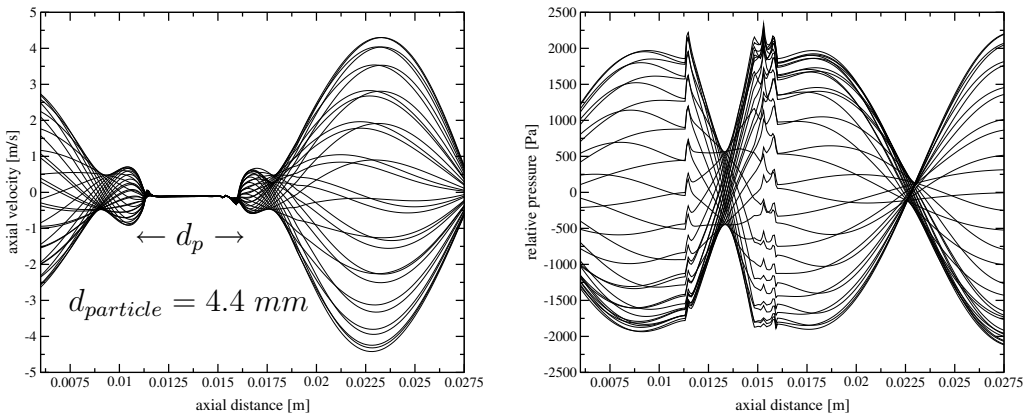

(a) velocity distribution

(b) pressure distribution

Figure 4.5.: Numerically computed velocity and pressure distributions at equidistant time-steps for an SWL disturbed by a levitated 45 μL drop.

surface tension, since the latter induces a pressure jump Δp at the interface of a stagnant droplet. The height of this jump is given by the Young-Laplace equation (2.14). Such a local influence of small obstacles on acoustic streaming was previously described in the literature (Lee & Wang, 1989; Yarin *et al.*, 1999). Further remarks on droplets in an acoustic sound field are given in Section 5.3.

4.7. Variation of Operational and Geometrical Parameters in Numerical Simulation

In general, variables influencing the ultrasonic field are subdivided into four categories: the ultrasonic generator, the state of the gas phase, the operating conditions, and the condition of the molten mass. The criteria of their impact is related to the refinement of the disintegration process since smaller particle do have a bigger surface while maintaining a constant energy intake into the system. Thus, the efficiency factor increases with smaller-sized particles (Li, 1996) at constant energy intake. Within this chapter, mainly the influence of parameter variations on the sound field itself is investigated and discussed. On the one hand, this will be done for the geometrical setup causing 5 pressure nodes due to the practical use of this

setup during experiments. On the other hand, ultrasonic fields of 3 pressure nodes will be investigated since they are described in literature. Thus, a direct comparison of these data with our numerical simulations of the ultrasonic field is possible. The influence of the condition of the molten polymer, e.g., viscosity or surface tension, on the disintegration process including resulting particle size distributions will be investigated in Chapter 6.

Since the frequency of a sonotrode is predetermined by its manufacturing, frequencies used for numerical simulation are identical with those of the pilot plant and are not altered. In the experimental setup a twin-oscillation unit with transducer frequencies of 19.9 kHz and 20.13 kHz, respectively, is used and, therefore, a beat of 230 Hz results. Such a frequency difference is recommended in literature (Li, 1996; Bauckhage *et al.*, 1996) to be at least 1% of the original frequency. According to Schädlich (2001), the maximum pressure amplitude inside a pressure antinode decreases with increasing frequency of the beat. Consequently, the pressure amplitude inside the pressure node growth. The impact of this behavior on particle size distribution was experimentally studied by Vestweber (2004) and will be discussed in more detail in Chapter 6.

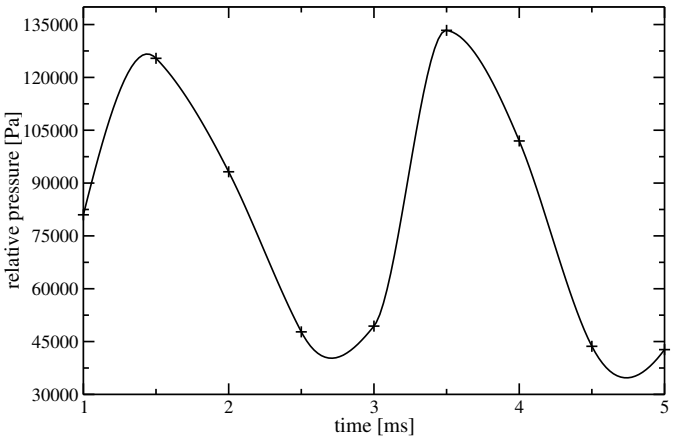

Figure 4.6.: Dependency of the maximum pressure amplitude on time.

The beat of an ultrasonic field is caused by swapping of oscillations having slightly different frequencies. Therefore, their overall phase shifts slowly resulting in maxima and minima which are called beat (Heywang *et al.*, 1992). The time necessary to pass a single beat period is calculated to be 4.3 ms according to

$T = 1/\triangle f$ (cf. Figure 4.6). Concluding, pressure amplitudes of different simulations to be compared have to be calculated at equidistant time-steps. Furthermore, since the ultrasonic field needs a distinct time to reach a quasi-stationary state, all pressure amplitudes numerically generated by simulation of the ultrasonic field are shown and compared at t = 1 ms.

4.7.1. Variation of the Sonotrode's Curvature

The concave shape of the sonotrodes presently used was empirically optimized for an ultrasonic field of 3 pressure nodes by slightly varying the sonotrodes curvature. For this purpose, various sonotrodes of different curvature were produced and resulting pressure fields were measured. Thereby, an optimal radius of curvature of 35 mm was found causing maximum pressure amplitudes. This procedure is expensive and time-consuming. In addition, if a 5-node pressure field is generated using such sonotrodes e.g., to reduce fouling of the surfaces, the previous geometry provokes no optimal focusing of the ultrasonic field and, therefore, lower pressure amplitudes. Thus, variations of the sonotrodes' curvature with respect to the resonant distance have been performed in order to improve the overall setup for a 5-node pressure field.

For the geometrical setup as described in Section 4.5.1, the optimal resonant distance is experimentally as well as in numerical simulations found to be $X = 37.5$ mm and $X_i = 46.9$ mm, respectively. First, the maximum pressure amplitude is determined by numerical simulation of the ultrasonic field under variation of the sonotrode's curvature keeping this distance constant. For a sonotrode amplitude of 80 μm maximum pressure amplitudes as illustrated in Figure 4.7 are found. As can be seen, maximum pressure amplitudes result for a sonotrode curvature of 2.13 mm^{-1} or a radius of curvature R_c of 47 mm, respectively.

This result mirrors phenomena known from linear wave theory for mirror-reflector configurations in optics. For a sonotrode's curvature of 47 mm the radius is almost identical to the sonotrodes inner distance ($R_{c,1} = R_{c,2} = X_i$). Therefore, this condition is stated to be a stable position according to Kneubühl & Sigrist (1991). The specific constellation is called confocal. Such type of resonator is most

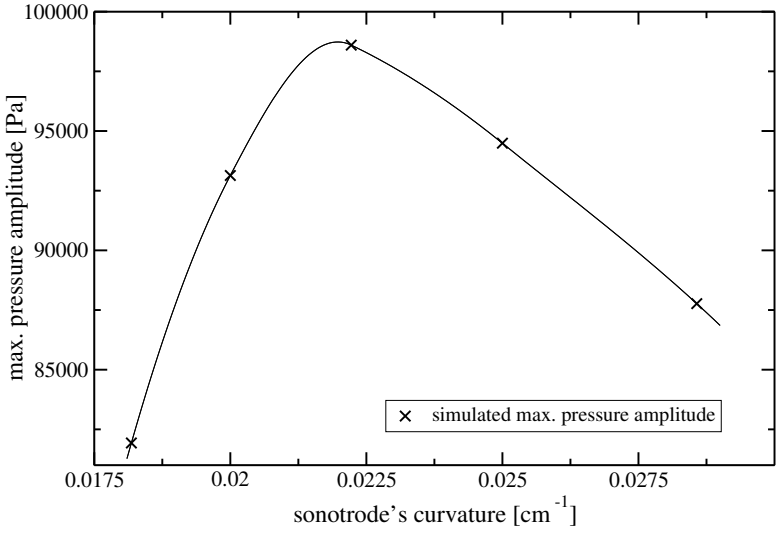

Figure 4.7.: Numerically simulated maximal pressure amplitude at 80 μm under variation of the sonotrode's curvature.

likely used since it is found to have least deflections compared to other reflection systems and, additionally, is less complicated during adjustment. Whether or not such a mirror-reflector unit is operated under stable conditions furthermore needs to be determined by stability criteria (Kneubühl & Sigrist, 1991). As a rough rule, the line between the two radii of curvature and their centers has to overlap in order to establish stable conditions. This is true for all investigations performed in numerical simulation of the system as well as in experiments with the pilot plant.

Further, the distance between the opposite sonotrodes is adjusted for each curvature to achieve the optimal distance, i.e. the distance causing the maximum pressure amplitude. As can be seen in Figure 4.8(a), the distance X_i is shifted inwards with decreasing curvature in order to obtain the maximum pressure amplitude (Figure 4.8(b)).

The observed trend is not congruent with effects known from optics, but justifies observations made by Gazka (1994) during the measurement of sound fields derived with different sonotrodes. If the radius of curvature is reduced, the focal length F will be reduced as well since

$$F = \frac{R_c}{2}.$$

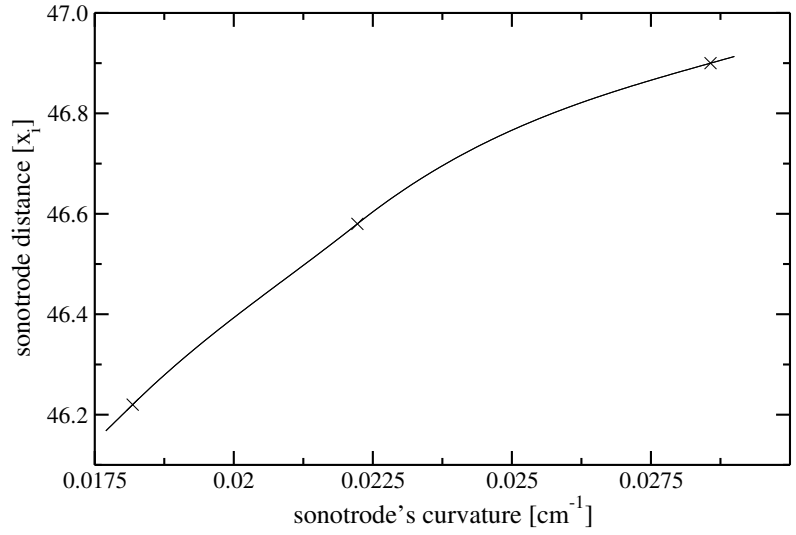

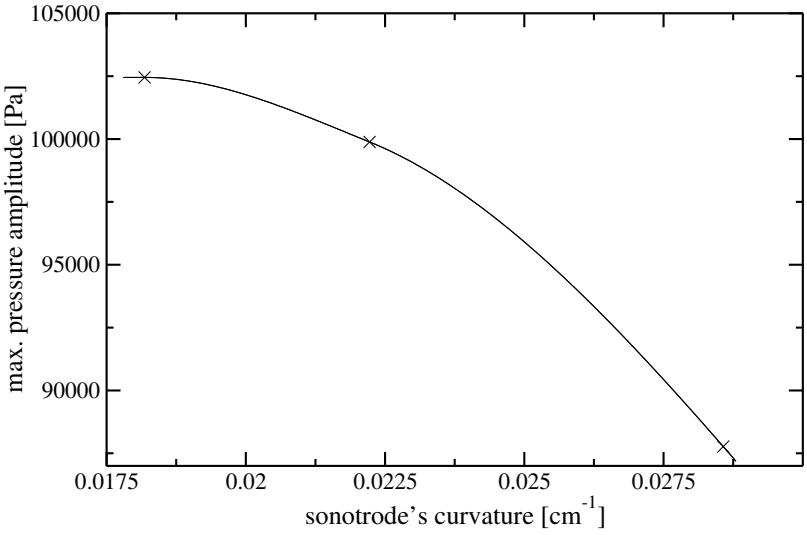

(b) Resulting max. pressure amplitudes at these distances.

Figure 4.8.: Dependency of max. pressure amplitude on curvature and resonant distance.

As the focal length is increasing linearly with decreasing curvature, the sonotrodes distance should increase as well to reach a new, optimal distance. Supposedly, two concurrent effects are observed here: Less curvature will cause a higher energy loss

due to scattering of the ultrasonic waves, whereas a decrease of the sonotrodes' distance will cause less energy loss. These two effects will superpose and cause the trend displayed in Figure 4.8. This points out that ultrasonic standing wave fields are not based on linear wave theory and, therefore, cannot entirely be explained by linear correlations.

4.7.2. Variation of the Sonotrode's Diameter

An extension of the sonotrodes diameter and, therefore, of the radiating surface should generally cause an increase in the overall pressure amplitude. However, the optimization of the sonotrodes geometry is limited due to technical feasibility since the emitted frequency correlates with the sonotrodes mass. Thus, an increase of the sonotrode's surface in order to achieve a better disintegration will commonly be associated with a lower frequency and a lower maximal oscillation amplitude of such a sonotrode. Nevertheless, numerical simulations are performed based on the original setup for an ultrasonic field of 5 pressure nodes (compare Section 4.6) under variation of the sonotrodes radiating surface. Therefore, the diameter of the sonotrodes has been extended from 35 mm to 50 mm and 60 mm keeping their curvature and distance constant.

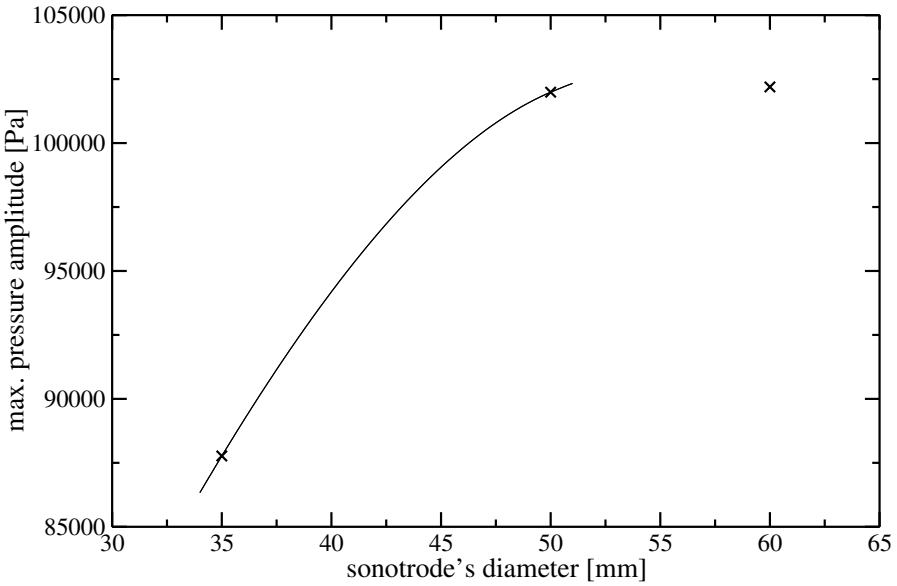

Figure 4.9.: Numerically simulated pressure amplitudes caused by different sonotrode diameters at a sonotrode amplitude of 80 μm.

As can be seen in Figure 4.9, a significant increase in the overall pressure amplitude can be observed in numerical simulation of the acoustic field with increasing sonotrode diameter. Since the acoustic field needs a longer time to reach a quasi-stationary state in case of extended sonotrode diameters, computed pressure amplitudes are compared at t = 2 ms. Additionally, the maximum pressure amplitude significantly increases at a diameter of 50 mm in comparison to the original setup, whereas less pressure difference is gained by a further increase of the sonotrode's diameter to 60 mm.

In order to operate the SWA with higher frequencies of about 30 kHz, the sonotrode's end face as the whole apparatus scale down by about 1/3. Figure 4.10 shows the schematic plot of a 30 kHz SWA in comparison to a 20 kHz oscillation unit as it is used during this work.

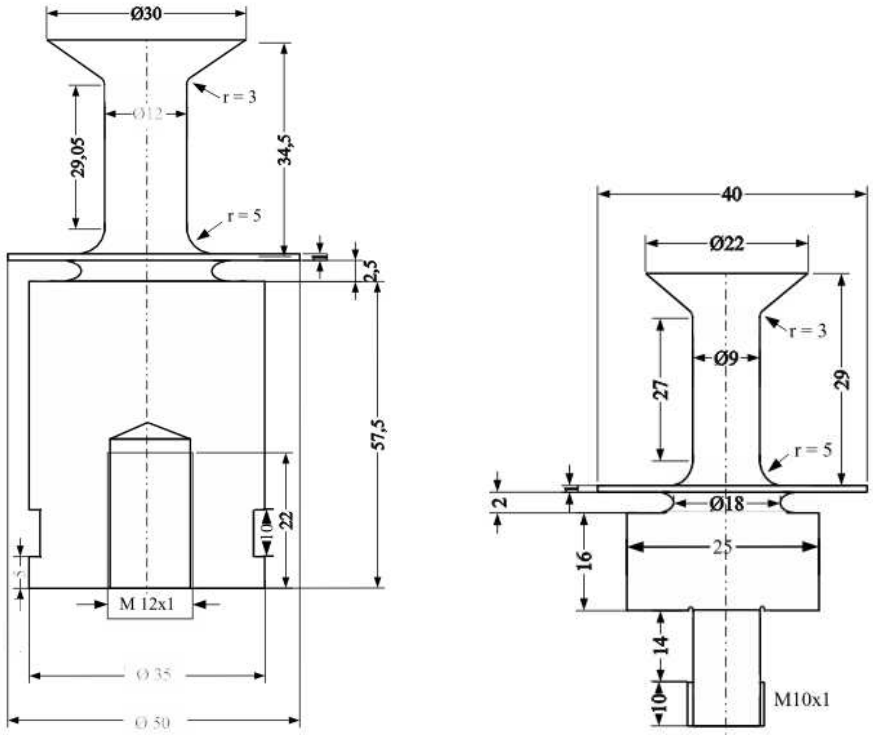

(a) 20 kHz oscillation unit (b) 30kHz oscillation unit

Figure 4.10.: Comparison of a 20 kHz and a 30 kHz oscillation unit used for atomization.

It is aspired to use transducers of smaller physical dimensions for desired direct applications. Further, higher oscillation frequencies do cause higher velocities inside the atomizer and, therefore, a better acceleration of the generated particles. This is an important feature if the atomized polymer strand disintegrates into droplets which do not cure fast enough. By increasing the frequency more air is ingested into the system from the environment causing the droplets to cool down and cure faster, respectively. Additionally, the beat of the ultrasonic field shall be vanished in further applications to avoid impacts on the particle size distribution caused by that effect. This is achieved by the construction of new electronic amplifiers, which are able to control the sonotrode's frequency (Hennig & Hemsel, 2004).

In order to compare results achieved by the 30 kHz transducer with the ones from the 20 kHz transducer, the mathematical product of the sonotrode's amplitude and its frequency is kept constant. Therefore, the SWA made up by two 30 kHz oscillation units is operated with a sonotrode amplitude of 53 μm unlike 80 μm for the 20 kHz transducer. The resonant distance X_i is found to be 32.5 mm by numerical simulation of the ultrasonic field. The resulting velocity and pressure distributions are shown in Figure 4.11.

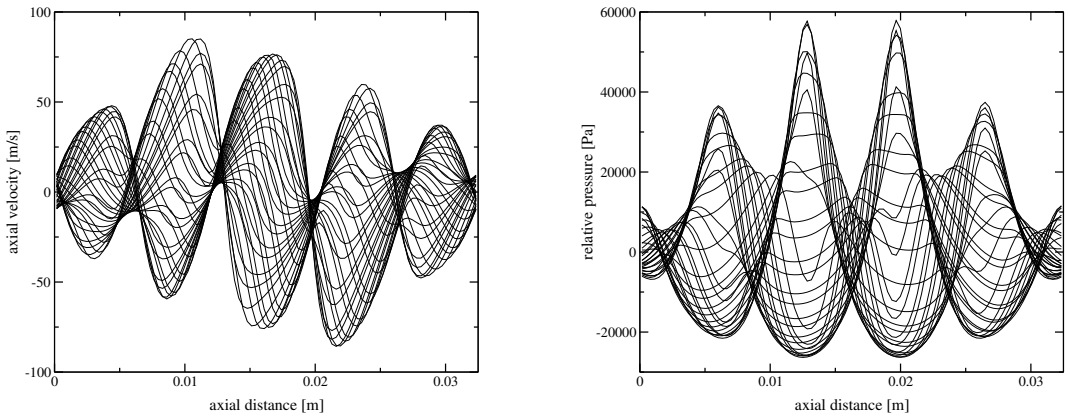

(a) velocity distribution

(b) pressure distribution

Figure 4.11.: Numerically computed velocity and pressure distributions at equidistant time-steps for an SWA generated by 30 kHz oscillation units.

As can be seen in Figure 4.11, the pressure field is equally distributed between

the inner pressure nodes. The generated pressure amplitude of those inner nodes is about 12 % higher than in the original setup (cf. Figure 4.3(b)) and, additionally, the velocity distribution inside the central velocity antinode outreaches the one from the 5-node pressure field shown in Figure 4.3(a) by about 20 %. The impact of these sound fields generated by a 30 kHz twin-oscillation unit without a frequency shift on the disintegration process need to be discussed in future projects.

4.7.3. Variation of the Gas Temperature

The operation of the transducers lead to heating of the sonotrodes and their surrounding as illustrated in Figure 4.2 by interferometric pictures. Therefore, the air between the two sonotrodes in an SWA will heat up as well causing a shift in e.g., viscosity and sound velocity. Further, large sound intensities appearing in an SWA itself lead to high temperature fluctuations inside the gas phase. Therefore, oscillating pressure and velocity distributions of the ultrasonic field are computed by solving the Navier-Stokes equations for compressible viscous flows (eq. (2.5),(2.7)) and the energy equation (3.1) since heat flux needs to be taken into account.

This heating of the air caused by operation of the plant is modeled during numerical simulation of the ultrasonic field by varying affected parameters. The specific variables are the particular temperature T, the viscosity μ, the thermal conductivity k, and the heat capacity c_p of the gas phase at a certain stage. These data are extracted from the "*Enzyclopedie de gas*" (Table 4.1) and implemented into the command file of the *CFX4*-solver.

The coefficient for temperature and thermal conductivity will directly be inserted into the energy equation (3.1), whereas the specific heat is affecting the total enthalpy h of the system. The total enthalpy is calculated inside the *CFX4*-solver by

$$h = h_{st} + \frac{1}{2}\, u^2 \ ,$$

with h_{st} as the static (thermodynamic) enthalpy. The transport equation has to be closed by supplying the constitutive equation, that is, the relationship between static enthalpy, temperature, and pressure, $h = h(t, p)$. The fluid is assumed

Table 4.1.: Parameters used to model temperature variations.

Temperature (T) $[K]$	viscosity (μ) $[Pa\ s \cdot 10^{-6}]$	conductivity (k) $[(J/m\ s\ K) \cdot 10^{-6}]$	specific heat (c_p) $[kJ/kg\ K]$
270	16.96	23.9397	1.005477
320	19.45	27.8536	1.006733
350	20.82	30.0722	1.008407
400	23.01	33.6345	1.011338
500	27.01	40.3782	1.013849

to be thermally perfect, hence, static enthalpy is a function of temperature only. Therefore, the constitutive equation is given uniquely by specifying the specific heat at constant pressure, as a function of temperature:

$$c_p(T) = \left(\frac{\partial h_{st}}{\partial t} \right)_p ,$$

with the reference temperature T_{ref}, where the static enthalpy is defined as zero. The enthalpy reference temperature T_{ref} is given the default value of 288 K in *CFX4*. The static enthalpy is then obtained by integrating

$$h_{st} = \int_0^T c_p(T')\ dT' \ - \ \int_0^{T_{ref}} c_p(T')\ dT' \ .$$

Inside *CFX4*, the constitutive equation is assumed to have the following analytic form:

$$h_{st} = \overline{c}_p(T)T - \overline{c}_p(T_{ref})T_{ref},$$

where $\overline{c}_p$ is an average specific heat, obtained by integrating

$$\overline{c}_p(T) = \frac{1}{T} \int_0^T c_p(T')\ dT' \ .$$

The specific heat is assumed to be a constant, independent of temperature, so that $\overline{c}_p = c_p$. This value can then be incorporated into the command file of *CFX4*. Finally, the gas viscosity is incorporated into the momentum balance (2.7) by means of the viscosity stress tensor (2.8).

The resulting maximal pressure amplitudes arising at each temperature for a 3-node pressure field are shown in Figure 4.12.

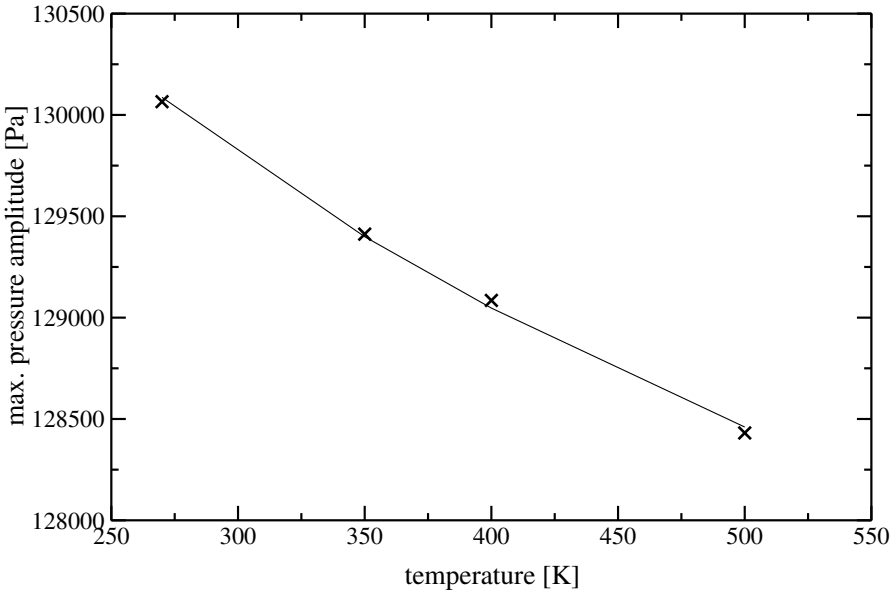

Figure 4.12.: Calculated maximal pressure amplitudes at different temperatures at a sonotrode amplitude of 80 μm.

As can be seen, the overall pressure amplitude decreases with increasing system temperature. This effect is mainly caused by the higher viscosity of a heated gas abating the maximal pressure amplitude. Instead, the resonant distance of the system does not change by variation of the temperature and its affected coefficients. In reality, even the transducer frequency shifts to higher frequencies with heating of the system. Therefore, the resonant distance between the sonotrodes need to be adjusted during operation of the pilot plant. Since this effect has not quantitatively been investigated in literature, it could not be accounted during numerical simulation of the ultrasonic field under variation of the temperature.

4.8. Acoustic Sound Pressure Level

For a qualitative impression of the obtained pressure fields, numerical simulations in *CFX* are compared to interferometric pictures as described in Section 4.5.2. Figure 4.13 shows several interferometric photographs of the acoustic field in an SWA at different sonotrode distances in comparison to pressure fields calculated

by *CFX*.

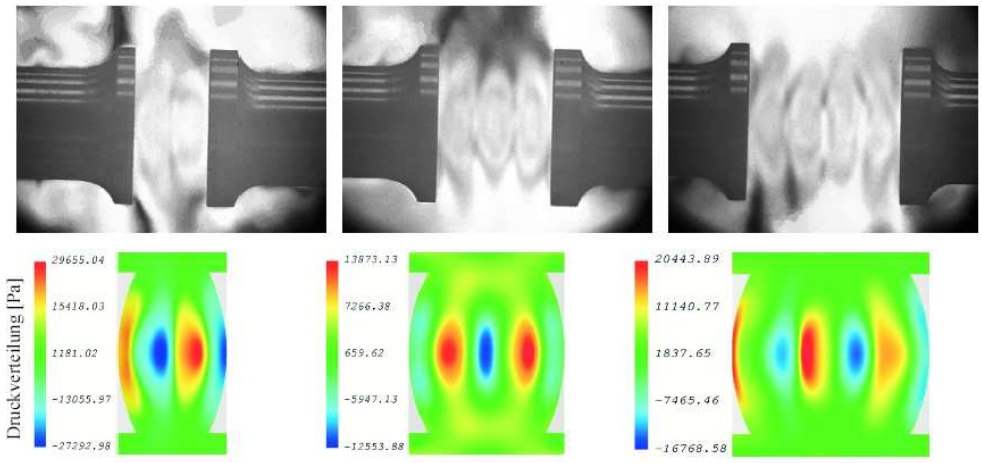

Figure 4.13.: Instantaneous pictures of pressure fields obtained in numerical simulation in comparison to interferometric shoots.

As can be seen, there is a good qualitative agreement between numerical simulation and experiment for identical operational conditions. Further, to quantitatively validate the derived pressure fields, numerical simulation of the pressure field need to be compared to specific data of experimental measurements of the acoustic field. For this purpose, the pressure distribution was determined by microphones taking measurements along the symmetry axis between the sonotrodes (Mattern, 1998). These microphones are made of piezo ceramics having a diameter of 1.5 mm. Hence, the measurement itself denotes an essential disturbance of the sound field. Therefore, Reipschläger (2002) found huge discrepancies between numerically determined sound pressure levels in comparison to Mattern's experimental data. Comparing the maximum sound pressure inside the pressure nodes, Reipschläger (2002) found pressure amplitudes derived by numerical simulations up to 36 % higher than in experiment.

Instead, Andersen (1996) and Meng (1997) used a conductor to derive the pressure level inside the sound field. In general, the technique is called thermoanemometry which is based on Wheatston's bridge circuit. In case of a CTA (*Constant Temperature Anemometer*), the temperature of a metal wire inside an SWA is kept constant. Due to the ambient gas flow of the ultrasonic field alter-

ing the temperature, electricity needs to be supplied to compensate temperature fluctuations. Therefore, a correlated electric current is measured determining the sound pressure level. This conductor is about 5 μm in diameter and hardly effects the sound field. In fact, Andersen (1996) found the deviation of a single set of data compared to the average value to be less then 5 %. Based on multiple experiments, Andersen (1996) finally developed a mathematical expression describing the effective sound pressure (p_{rms}) as the root mean square of the intrinsic pressure. For two active, concave sonotrodes with a radius of curvature of 32.5 mm, a sonotrode's diameter of 35 mm, and frequencies of 20 kHz Andersen (1996) derived the following equation:

$$p_{rms} = 0.056 \cdot p_0^{0.99} \cdot A^{0.71} \cdot N_k^{-0.64} \,, \tag{4.14}$$

with the static ambient pressure p_0 in 'bar' and the sonotrode amplitude A in μm.

According to Stamm & Purzel (1984), a correlation between an arbitrary pressure signal p_{rms} and the maximum sound pressure p_{max} of a sinusoidal function is found:

$$p_{rms} = \sqrt{\frac{1}{T}\int_0^T p^2(t)\; dt} = \frac{1}{\sqrt{2}} p_{max} \tag{4.15}$$

Hence, combining the correlations of Stamm & Purzel (1984) and of Andersen (1996) allows a prediction of the expected maximal pressure amplitude inside a pressure node under given operational conditions. According to eq. (4.14) and eq.(4.15), the maximal pressure amplitude can be calculated as 88779 Pa for a sound field of 3 pressure nodes and sonotrode amplitudes of 80 μm at standard conditions. Numerical simulations of the pressure field using *CFX* for sonotrodes with $R_c = 35$ mm and otherwise identical conditions results in a maximal pressure amplitude of 88702 Pa. Therefore, the theoretical prediction matches the numerically calculated pressure level very well.

5. Droplet Levitation

First investigations concerning levitator experiments were done by the European and American Space Agencies, ESA and NASA, in the early 1970th. For the containerless processing of samples under microgravity conditions, they balanced an inserted sample in an ultrasonic standing wave field against gravity (Lierke, 1996). Later on Hohmann *et al.* (1988) and Bending (1988) found similarities between the atomization of a levitated single liquid droplet inside an ultrasonic field and the continuous disintegration of a liquid strand. Therefore, results achieved by the investigation of single liquid droplets in an ultrasonic standing wave levitator (SWL) should allow for conclusions of the continuous disintegration process of polymer melts. Hence, because of the enormous complexity of the continuous disintegration process, atomization and deformation of single liquid droplets are investigated in the somewhat simpler system of an SWL. This approach allows for comparison between experimental data of the deformation process and numerical results.

5.1. Previous Investigations

The behavior of droplets in an ultrasonic sound field has been a field of interest for many years. Therefore, numerous experimental and theoretical investigations have been performed, aiming to understand phenomena and mechanisms occurring in processes of droplet deformation and breakup. First calculations on linear droplet deformations were done by Rayleigh (1879*a*,*b*) and Lamb (1932) for the inviscid and weakly viscid cases. More recently, nonlinear oscillation of non-viscous and viscous drops was analyzed by, e.g., Tsamopoulus & Brown (1983), Basaran (1992), Yarin *et al.* (1998) and Murray & Heister (1999). Basaran (1992) used the finite element technique to address nonlinear oscillation of viscous droplets. Based on the computation of the acoustic radiation pressure, Yarin *et al.* (1998) calculated the droplet's shape by means of the boundary element method. Finally, Murray

& Heister (1999) simulated the unsteady, nonlinear response of a liquid droplet to an imposed acoustic perturbation using the boundary element method. Lierke (1996) mainly focused on experimental aspects of droplet levitation. Calculations based on the linear wave theory were done by Lee *et al.* (1991, 1994), Trinh & Wang (1982) and Anilkumar *et al.* (1993). They recorded droplet deformation with high-speed cameras until breakup and compared the resulting experimental data to model calculation.

5.2. Mechanism of the Atomization Process

The dynamics of droplet flattening and breakup have been discussed in several papers, e.g. Danilov & Mironov (1992); Yarin *et al.* (1999); Lee *et al.* (1991); Anilkumar *et al.* (1993); Becker *et al.* (1991, 1994). This was done by theoretical studies as well as by experimental investigations. In general, three stages are described in literature including the flattening of the droplet, the growth of small-scale disturbances at its rim, and the parametric growth of capillary waves on its surface. In addition, during droplet flattening, two limiting scenarios are identified by Lee *et al.* (1991) and Anilkumar *et al.* (1993) while increasing the sound pressure level:

i) acoustically big drops ($kR_s \gtrsim 0.5$) sustain equilibrium beyond a point, by lowering the sound pressure level through frequency shift,

ii) acoustically small drops ($kR_s \lesssim 0.3$) cannot sustain equilibrium beyond a point, and expand horizontally suddenly to disintegrate,

where $k = 2\pi f_0/c_0$ (c_0: sound speed in air) is the acoustic wave number and R_s denotes the spherical radius of the droplet. Instead, for drops of intermediate size, sudden horizontal expansion can be observed but return to equilibrium. Regarding the size of a droplet with respect to kR_s, different geometries will occur during flattening to final breakup.

Large droplets of $kR_s \gtrsim 0.8$ will get unstable during levitation and finally collapse caused by "buckling" instability. First, the flattened drop will change its shape from convex to concave. A dimple will be formed in the middle which

eventually thins out into a membrane. While the area of the membrane will grow increasing the sound pressure level, the liquid is squeezed to the edges giving a donut-shaped periphery. Ripples may appear on the central membrane. This membrane will then suddenly bulge upward while being flattened. Since the thicker periphery is picking up speed some time later, it is contracted inwards to turn the flattened drop into a closed shell. The closing marks a violent collision forming liquid jets which move vertically in both directions. By the jet piercing the outer shell the complex will smash to pieces. This process is also called "buckling" instability (Lee *et al.*, 1991). Smaller droplets may stay stable while ripples appear and emit satellite drops in both directions perpendicular to the membrane. Therefore, they return to equilibrium in shifting their frequencies.

The investigation of the flattening and atomization of small drops ($kR_s \lesssim 0.3$) is most important throughout this study, since droplets generated in an SWA during continuous strand disintegration are of the size of a few μm. Therefore, the following discussion and investigation of breakup phenomena will focus on this type of droplets.

5.3. Deformation and Breakup Regimes

The deformation and breakup of droplets by aerodynamic forces can be characterized by the Weber and the Ohnesorg number. Here, the dimensionless Weber number is defined as

$$\mathrm{We} = \frac{\rho_g u_{rel}^2 d}{\sigma} \,, \tag{5.1}$$

where d denotes the spherical drop diameter, u_{rel} the amplitude of the relative velocity, and the index g gas phase. The Weber number describes the ratio of aerodynamic (drag) to surface tension forces. If a droplet is exposed to a gas flow of increasing velocity, deformation starts at Weber numbers of unity according to Hsiang & Faeth (1992). A further increase in the sound pressure level and aerodynamic forces, respectively, will lead to droplet breakup. With respect to the intensity of the aerodynamic forces, three different disintegration mechanisms are distinguished: The aerodynamic forces act against the viscose forces inside the droplet and the surface tension forces. With increasing relative velocity between

droplet and sound field, the aerodynamic forces affecting the droplet increase as well until breakup is initiated. The three distinct mechanisms are called bag, multimode, and shear-breakup.

Since Hinze (1955) found that progressive larger disturbances (i.e. larger We) were required for the onset of breakup as Oh increases, low Oh numbers are desired. This is because Oh represents the ratio of liquid viscous to surface tension forces:

$$\mathrm{Oh} = \frac{\mu_d}{\sqrt{\sigma \rho_d d}} \ ,$$

where μ_d denotes the viscosity of the disperse, liquid phase and the index d the disperse phase itself. Therefore, viscous forces in the liquid tend to inhibit drop deformation at high Oh. For a system of small water droplets levitated in air Oh becomes reasonable small, e.g., for a water drop of 45 μL Oh calculates as $\mathrm{Oh} = 1.8 \cdot 10^{-3}$. Therefore, viscous forces can be neglected during levitation and atomization of water drops. Instead, in case of the disintegration of polymers having a viscosity of 0.1 Pa s $< \mu <$ 2 Pa s much higher Oh numbers of Oh > 3 result for droplets in the desired range of 50 μm.

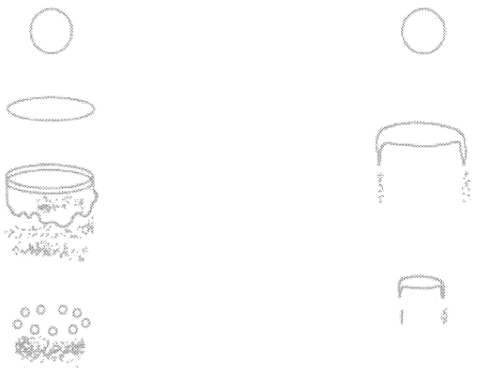

(a) bag breakup

(b) shear breakup

Figure 5.1.: Breakup mechanism for bag and shear breakup.

The critical Weber number We_{cr} defines the onset of *bag breakup*. This stage is generally found to be at We $\approx$ 10. The bag breakup regime is characterized by the formation of droplets which separate from a bag-like fluid film. This film

expands from the tutorial rim (cf. Figure 5.1(a)). For higher Weber numbers of We $\approx$ 20 *multimode breakup* occurs. This stage is characterized by a fluid column that remains in the center of an umbrella-like film structure. A further increase in the relative gas velocity leads to the *transitional breakup* regime which passes into the *shear breakup* regime. During the shear breakup mechanism ligaments are stripped of the rim of a disc shaped droplet. This mechanism is illustrated by Figure 5.1(b) for We $\approx$ 70.

In common levitation experiments, the range of large aspect ratios close to atomization tries to be avoided. Therefore, atomization in an SWL occurring at law We numbers is most commonly subject to the bag breakup mode. Instead, during continuous strand disintegration large We numbers are yielded in order to let the atomization process occur. Additionally, secondary breakup of fragments stripping of the lamella will be supported. Therefore, the shear breakup stage is commonly found during disintegration in an SWA. As Lierke (1998) pointed out, atomization of levitated droplets will be initiated if the Weber number exceeds a critical range of about $We_{cr} = 10$. Then, the drop will disintegrate by Bernoulli forces similar to gas jet atomizers. Even Hohmann *et al.* (1988) and Bending (1988) found similarities between the atomization of a levitated single liquid droplet inside an ultrasonic field and the continuous disintegration of a liquid strand. They point out, that the mechanism of disintegration is mainly dominated by the acoustic sound pressure and the Bernoulli stress.

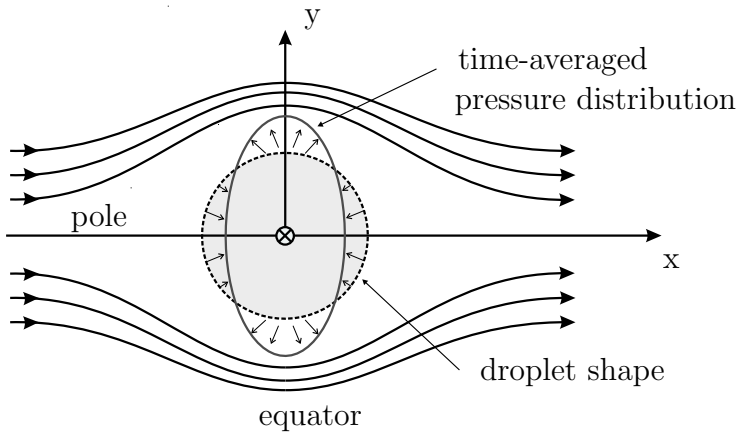

Figure 5.2.: Bernoulli effect on a levitated droplet.

5.3.1. Bernoulli Pressure - Qualitative Characterization

In the context of droplets flattening mechanism, Bernoulli pressure is often cited as one main reason for deformation: since the droplet acts as an obstacle forcing the gas flow to go around it, higher velocities at the droplet's equator lead to lower pressure here which pulls at the droplet (cf. Figure 5.2). This line of arguments is not strictly valid due to several reasons. First of all, Bernoulli's law in its most common formulation

$$\underbrace{\frac{1}{2}\rho\,||u||^2}_{\text{dynamic pressure}} + \underbrace{p}_{\text{static pressure}} + \underbrace{\rho g z}_{\text{hydrostatic pressure}} = \text{const} \tag{5.2}$$

is only valid for stationary potential flows, also neglecting dissipation of mechanical energy as well as density variations. Here gz denotes the body force due to gravity which acts perpendicularly to the symmetry axis in our situation.

In case of the ultrasonic sound field under consideration, time-averaged variations in density are negligibly small over an acoustic cycle according to numerical simulation. Despite of this, especially the strong time-dependence of the oscillating velocity field rules out the applicability of (5.2). Instead, the time-dependent version

$$\frac{\partial \phi}{\partial t} + \frac{1}{2}\,||u||^2 + \frac{p}{\rho} + gz = \text{const} \tag{5.3}$$

of eq. (5.2) has to be used. Here, the constant might in principle depend on time, but the fact that all flow variables are almost constant at a certain radial distance leads to the same constant for all t.

Now, Lierke (1998) argues that the *time-averaged* pressure and velocity fields act according to Bernoulli's prediction since the drop does not react on every oscillation of the ultrasonic field. Thus, the uniform velocity between droplet and gas flow needs to be replaced by the effective value of the periodically varying sound particle velocity in axial direction. In fact, in our numerical simulations we observe, firstly, that the rotation of the instantaneous velocity fields reaches only 4 % of the strength (measured in Euclidean norm) of the corresponding gradient such that the flow is close to potential flow and, secondly, that maximum gas velocities occur at the droplet's equator accompanied by minimal pressure there (cf. Figure 5.3), i.e.

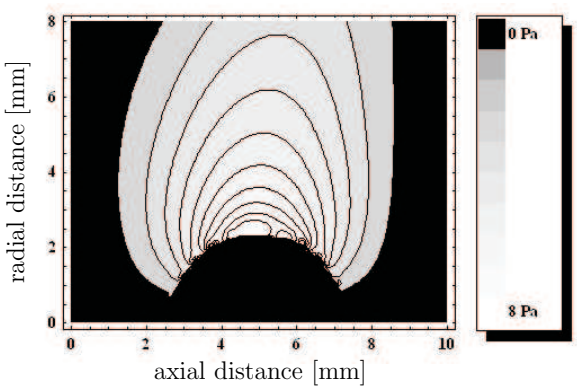

(a) dynamic pressure

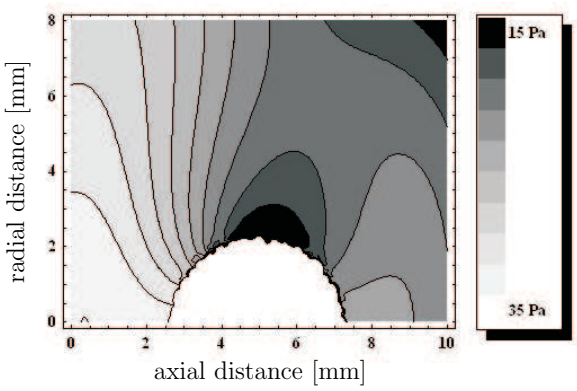

(b) static pressure

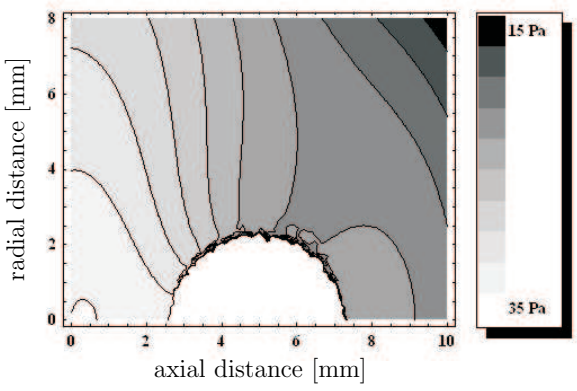

(c) total pressure

Figure 5.3.: Contour plot of averaged pressure distributions over an acoustic cycle for an SWL disturbed by a levitated 45 μL drop.

eq. (5.3) seems to apply for the time-averaged velocity field. A possible explanation relies indeed on the different time-scales involved, since integration of eq. (5.2) on $[0, T]$ leads to

$$\overline{\frac{1}{2}\,||u||^2 + \frac{p}{\rho}} + gz = \frac{\phi(t+T) - \phi(t)}{T} + \text{const}\ ,$$

a relation that closely resembles eq. (5.2) when T is large compared to the fluctuations of the velocity potential ϕ. The latter is reasonable if T is large compared to the ultrasonic time-scale.

These considerations are supported by our numerical results as illustrated by Figure 5.3. The contour plots show typical distributions of dynamic and static pressure, time-averaged over one acoustic cycle of 50 μs. In hydrodynamics the sum of dynamic and static pressure is called the total pressure as illustrated in Figure 5.3(c). Overall, pressure maxima correspond to white regions, whereas the minima are shown in black. Evidently, the static pressure is larger at the poles, and correspondingly, the velocities are larger at the equator of the drop. What results is an impact pressure (*Bernoulli pressure*) at the poles and a depression (*Bernoulli suction pressure*) at the equator. These cause flattening of the drop in the direction of the alternating gas flow. This effect is in turn intensified by the flattening, since the latter leads to a larger pressure difference between equator and poles. As the drop deforms the surface curvature at the equator increases continuously. This leads to a corresponding increase in surface tension forces that act against the deformation and, hence, Bernoulli pressure. Therefore, Bernoulli pressure and restoring forces have an enormous influence on droplet deformation and breakup. Whether the drop achieves an equilibrium state in which the Bernoulli pressure is balanced by the surface tension forces depends on the strength of the pressure forces.

Unlike the common form of Bernoulli's equation (5.2) the resulting total pressure may still depend on the position. In fact, as can be seen in Figure 5.3(c), the total pressure has an almost linear axial profile in the region around the droplet. Despite of this, the pressure minima and velocity maxima at the droplets equator balance each other locally. This behavior once more emphasizes the narrowness of the influence of droplets on the ultrasonic field.

5.3.2. Bernoulli Pressure - Quantitative Characterization

Beside such qualitative studies as performed in Section 5.3.1, numerical simulations of the correlated two-phase flow allow for quantitative investigations of the effect of Bernoulli pressure on droplet behavior. For example, for a levitator oscillating at an amplitude of 5.34 μm the maximum velocity of the gas in axial direction is computed to be u_{max}= 3.32 m/s (We = 0.77) for an unperturbed sound field, while it increases to a maximum of u_{max}= 17.4 m/s (We = 21.25) at the rim of a flattened, ellipsoidal 45 μL droplet (cf. Figure 5.4).

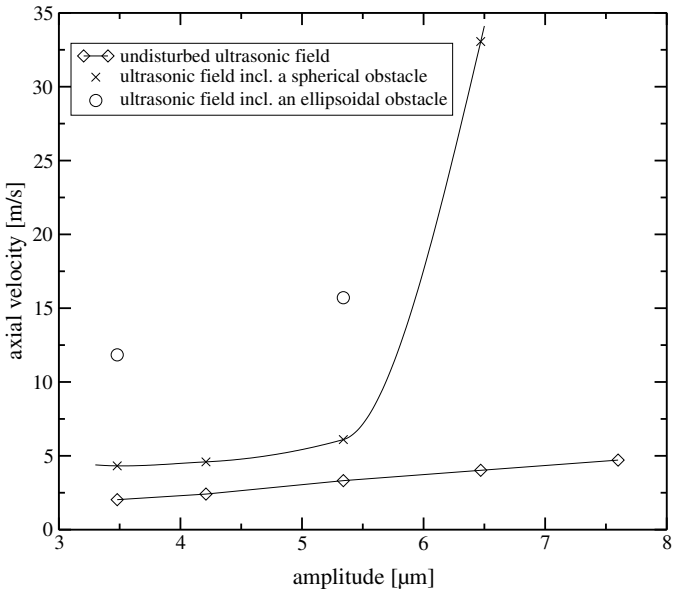

Figure 5.4.: Amplitude versus calculated axial velocity.

In fact, the Bernoulli pressure can lead to the onset of disintegration. For the investigated sonotrodes droplet breakup is observed experimentally at amplitudes above 5.34 μm, while numerical calculations based on the corresponding but unperturbed sound field predict a flattened drop. A threshold for breakup can be defined by means of a critical Weber number (We_{cr}) describing the ratio of aerodynamic to surface forces. According to Schmehl *et al.* (2000), the transition from deformation to breakup is calculated to occur at $We_{cr} = 12$ in case of a 45 μL water droplet with $Oh = 1.8 \cdot 10^{-3}$ (cf. Figure 5.5), corresponding to a relative velocity of the gas phase of u_{rel} = 13.1 m/s, respectively. Atomization occurs locally if

the relative velocity at the droplet's surface exceeds this critical value. In fact, although the maximum velocity of the gas in axial direction is computed to be $u_{max} = 17.4$ m/s (We = 21.25) at the rim of a flattened, ellipsoidal 45 μL droplet, the onset of breakup is already found for values of $u_{rel,cr} = 14.9$ m/s ($\mathrm{We}_{cr} = 15.66$). This value characterizing the transition from deformation to breakup mirrors the calculated We_{cr} of Schmehl *et al.* (2000) very well. Consequently, back-effects of droplets onto the sound field have to be taken into account in numerical simulations in order to quantitatively reproduce the deformation and disintegration of droplets.

Slightly higher sonotrode amplitudes of 6.47 μm already cause a relative velocity of the gas phase of $u_{rel} = 33.1$ m/s (We = 76.8) in numerical simulation of the disintegration process leading to a spontaneous atomization of an inserted droplet. These droplets are exposed to the shear breakup mode. Therefore, the transition regime from bag breakup to shear breakup is densely close to each other. Consequently, disintegration mechanisms observed in experiments (Section 5.4) as well as in numerical simulation (Section 5.5) are of the shear breakup type.

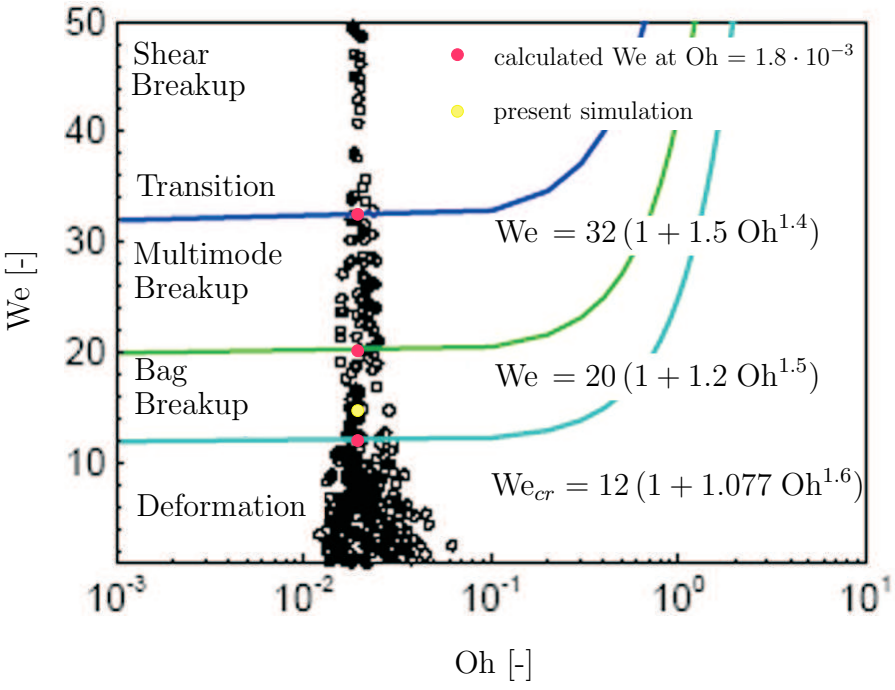

Figure 5.5.: Breakup regimes (based on Schmehl *et al.* (2000)).

5.4. Experimental Investigations of the Deformation Process

The experiments are conducted in a single-axis standing wave levitator (SWL), which allows to study the behavior of single liquid droplets in a sound field under simplified conditions (cf. Figure 5.4).

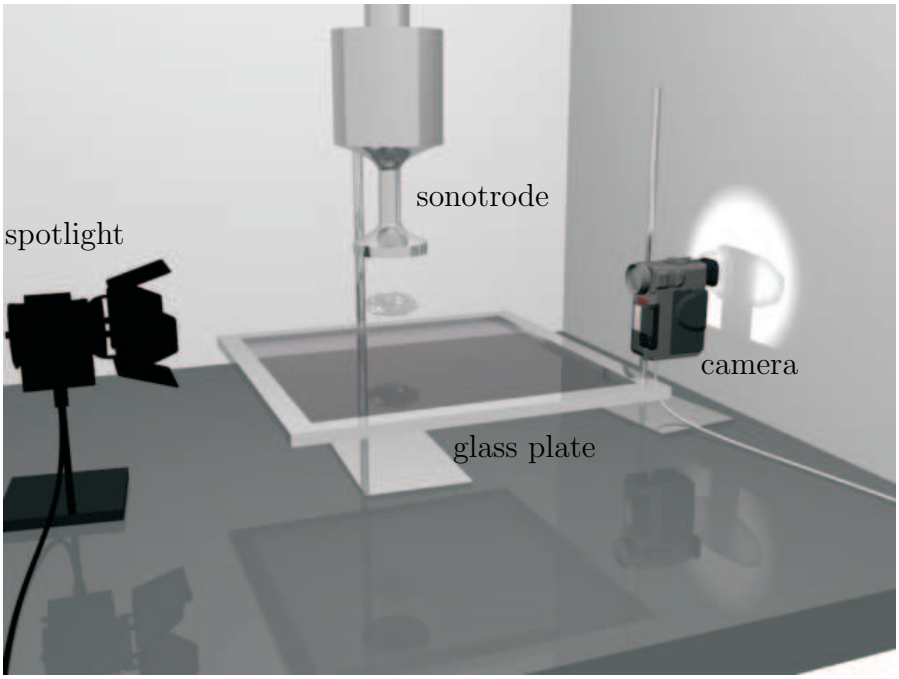

Figure 5.6.: Experimental setup for droplet levitation

This device is made up of an oscillator-reflector configuration at resonance conditions. A glass plate is chosen as a reflector whose distance to the oscillator can be varied by a micro-screw. Therefore, a distance of 23.3 mm resulting in a 3-node field is chosen for levitation (cf.F̃igure 4.4). Using this oscillation unit, droplets positioned in the central pressure node can be levitated against gravity. Increasing the sound amplitude leads to the disintegration of droplets, as shown in Figure 5.7 for an acoustically small one ($kR_s = 0.3$). Such a water drop is levitated at a fixed frequency of $f_0 = 19984$ kHz, and disintegrates due to a rapid increase of the sound intensity within a few milliseconds. This highly dynamic process is recorded with a high-speed video camera at 1000 frames/sec, showing a sequence of events from flattening via buckling to final breakup of the water drop. If the acoustic

amplitude increases rapidly, the drop is flattened into a thin lamella by the acoustic pressure acting on its surface. This lamella then becomes unstable at its rim, where cylindrical-like ligaments will be separated that immediately disintegrate into smaller droplets. These droplets will then move radially outwards from the center of the lamella. This process is similar to the continuous disintegration of liquid strands by SWA, for which a quasi-stationary lamella develops at the outlet of the nozzle. This lamella is oriented parallel to the sonotrodes' end faces, continuously separating fragments at its rim, which disintegrate into smaller particles.

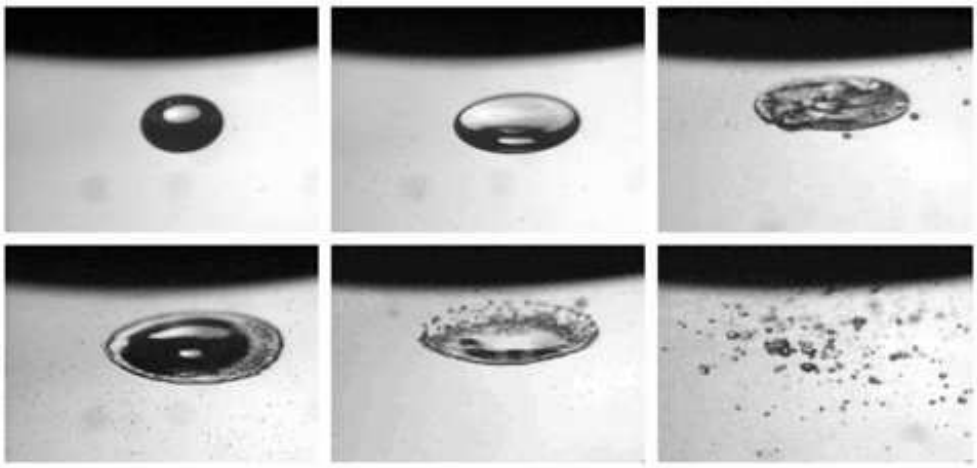

Figure 5.7.: Sequence of deformations of a water drop with $kR_s = 0.3$.

5.5. Numerical Investigations of the Deformation Process

In order to compare experimental data of the deformation process, recorded by means of a high-speed camera, and numerical results, simulations of levitated droplets in an SWL are conducted using identical conditions as in experiments. As mentioned in Section 3.2, time-averaged pressure and velocity fields of an unperturbed sound field are computed with *CFX*. To simulate droplet dynamics these fields are read into *FS3D* to account for source terms at the fluid interface. The calculations are done assuming two symmetry planes (cf. Section 3.4.2). The numerically obtained evolution of the disintegration of an acoustically small water

drop is displayed in Figure 5.8.

Figure 5.8.: Sequence of simulated deformations of a water drop with $kR_s = 0.3$mm.

The computational domain covers a cube of 0.125 cm^3 having 128 grid cells in each coordinate direction. The drop is exposed to a rapid increase of the acoustic amplitude by 50 kPa in order to mirror the droplet breakup conditions used to generate the pictures of Figure 5.7. Evidently, pictures obtained from the numerical simulation agree very well with the ones obtained during experimental disintegration of an acoustically small water droplet. The pressure drop from poles to the equator of the droplet causes flattening. Since the drop is exposed to gravity it is slightly buckled, developing an arched shape in its cross section, having a thin middle membrane and a surrounding large rim. If the drop is suddenly exposed to a high speed blast of air, it is deformed into a plano-convex lenticular body due to the acceleration of the drop (Anilkumar *et al.*, 1993) as is typical for the shear-breakup mode. With increasing flow velocity, the surface becomes more concave. In this case, the convex face of the body is facing the sonotrode. Droplets are then generated by stripping from the periphery of the droplet. Currently, it is believed by Anilkumar *et al.* (1993) that breakup is caused by the edges of the saucer-shaped body being drawn into a thin sheet by the strong viscous stress due to the high speed of the air flow. Equilibrium is lost when the viscous shear stress overcomes surface tension locally, whereby the edge is drawn out into a sheet. The generated sheet will then segregate into fine-scale fragments, which can break down further. Drops will exit at well-defined frequencies due to the rapid growth of capillary surface waves. This is the main mechanism responsible for disintegration (Anilkumar *et al.*, 1993). Instead, Danilov and Mironov (1992) found small-scale interfacial instabilities caused by the gas flow around the drop to be more impor-

tant for atomization than other acoustic processes. Small droplets are blown off the edge of the drop as a result of this instability. Yarin et al. (1999) emphasized that acoustic levitation causes acoustic streaming near the drop surface, hence triggers interfacial instabilities. When the droplet becomes considerably flat, oscillation of the droplet establishes a mechanism for the parametric excitation and growth of capillary waves on the droplet's surface. These waves increase in amplitude until the drop collapses. Capillary waves on the droplet's surface can also be reproduced in numerical simulations of the disintegration process. Their impact on the atomization process in numerical computations can be strengthened by slightly perturbing the acoustic forces with white noise. This final collapse leads to rather large fragments, the size of which will decrease with increasing sound frequency.

5.6. Size Determination of the Deformation Complex

To quantitatively compare and furthermore validate the developed approach, the flattening of drops in an ultrasonic field has been studied and resulting drop diameters have been determined. For this purpose, a sequence of experiments producing deformed droplets under various sound field amplitudes (A) has been performed. Measured diameters are compared with data obtained by numerical simulations under identical conditions.

The response of a drop to changes in the sound pressure level can be elegantly represented in terms of the acoustic Bond number

$$\mathrm{B_a} = \frac{\mathrm{A^2 R_s}}{\sigma \rho \mathrm{c}^2} \ ,$$

as the ratio of hydrostatic and capillary pressure. As the sound field amplitude, maximal pressure in the pressure antinode are taken for an undisturbed ultrasonic field. Figure 5.9 displays the relationship between the acoustic Bond number and the non-dimensional equatorial radius $\mathrm{R^*=R/R_s}$ (R: equatorial Radius) of a 45 μL droplet. As can been seen, a large deviation is found between experimental and numerical results if back-effects of the droplet on the ultrasonic field are neglected. This discrepancy is especially significant for experiments performed with an SWL because the generated pressure amplitudes are relatively small and, therefore, the drop causes a rather strong perturbation of the ultrasonic field. If the sound field

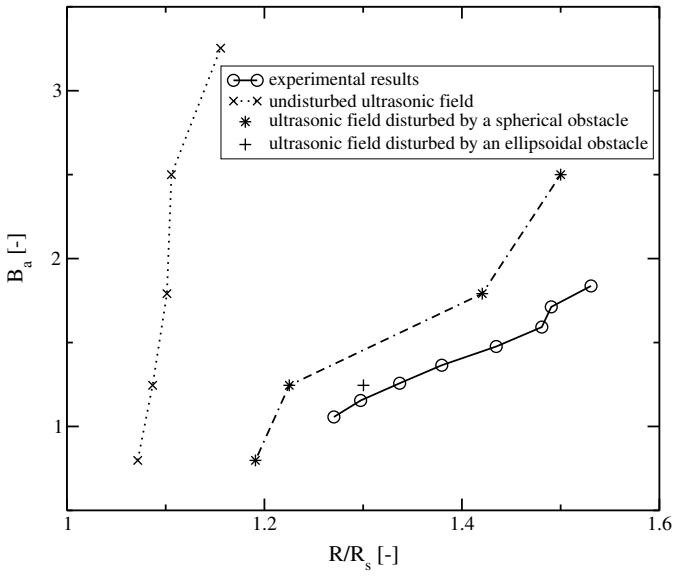

Figure 5.9.: Normalized radius R^* versus acoustic Bond number.

is perturbed by a spherical water drop, pressure and velocity fields result as shown above in Figure 4.5. These simulations of a two-phase flow with compressible gas phase are performed with *Fluent* using the VOF-method. After time-averaging and interpolation, these data are transferred into *FS3D* for calculation of the deformation process. Resulting droplet diameters mirror experimental results far better. Results are even almost identical, if the sound field is calculated for an appropriate ellipsoidal droplet as an obstacle. Hence, Bernoulli stress and local velocity peaks near the liquid surface are the main quantities determining droplet deformation and breakup. In particular, pressure and velocity increments caused by the Bernoulli effect can exceed acoustic effects of the applied sound field by several orders of magnitude.

6. Strand Breakup

The production of fine droplets from liquids in a surrounding gas phase is called disintegration. Thereby, the density ρ_g of the surrounding gas phase is explicitly smaller than the one of the droplets forming liquid. This is the main argument found in literature to explain the disintegration process as an aerodynamic problem (Andersen, 1996; Reitz & Bracco, 1982). Hence, the mechanism of liquid disintegration especially at high fluid velocities significantly differs from the dispersion mechanism at low density differences.

Table 6.1.: Width of the particle size distribution for different disintegration mechanisms.

Mechanism	$d_{v.0.5}/d_{32}$	$d_{max}/d_{v.0.5}$
dripping	1	1.1
natural laminar strand disintegration	1.05-1.1	1.4
lamella nozzle	1.1-1.3	1.5-2.5
turbulent nozzle	1.3-1.5	2.5-3.5
pneumatic atomizer	1.1-1.5	2.5-3.5
rotational atomizer		
ligament state	1.05-1.1	1.4-2.0
lamella state	1.1-1.4	2.5-3.5
capillary wave atomizer	1.05-1.4	1.5-2.5

The production of such fine droplets is mainly done by the disintegration of lamellae. In this case three different mechanisms are distinguished (Walzel, 1990):

1. boundary contraction
2. aerodynamic wave creation
3. turbulent disintegration

These three disintegration mechanisms are mainly superposed and, therefore, cannot be treated separately. In contrast to liquid filaments or strands the lamella is stable. Each deformation of a lamella will then cause an increase in its surface and, therefore, result in reversed forces (Bond, 1935; Tayler, 1959; Squire, 1953). To characterize the created droplets the Sauter diameter d_{32} is generally used as the mean particle diameter. It has the same surface/volume ratio as the overall particle size distribution (*PSD*). Typical values for the width of particle size distributions for different types of breakup mechanisms are given in Table 6.1.

During the dripping state surface forces are dominant leading to particles of almost the same size (cf. Figure 6.1). With increasing velocity of the liquid strand or the surrounding gas phase friction forces get more important and the particle size distribution gets more diffuse. Aiming to keep the *PSD* tight and to inhibit oversized grain is the overall goal of the following investigations during the disintegration process in an SWA.

6.1. Previous Investigations

The first patent using ultrasonic standing waves for the disintegration of fluids is dated back to 1976 (Lierke & Ruckdeschel, 1976). This specification describes a method for the disintegration of fluids and powders based on ultrasound waves producing droplets between an ultrasonic piston and a reflector. A later patent from Lierke *et al.* (1980) states fluids, molten metals, suspensions, emulsions, and agglomerated powders as a field of application.

Focussing on molten metals Hohmann *et al.* (1988) and Bending (1988) published papers describing the production of metal powders by an SWA. To overcome the high surface tension of these molten metals, the surrounding pressure was increased to 5.5 bar using a pressure chamber. Thereby, the Bernoulli force is said to have been increased, which was accounted to be the main force for the disintegration mechanism. They used tin for disintegration and obtained mass medians between 60 and 100 μm for the atomized metal in dependence on different sonotrode amplitudes.

Schreckenberg (1991) and Bauckhage (1992) predicted a semi-empirical in-

terrelationship between the mass median ($d_{50,\dot{3}}$) of a particle size distribution and several process parameters:

$$d_{50,\dot{3}} = \alpha\sigma\sqrt{\frac{c_0}{p_g\, I}}\ \mathrm{We}^{1/7}\ , \tag{6.1}$$

with the surface tension σ, p_g denoting the gas pressure, and I the capacity based on the sonotrode's cross-sectional area. The factor α empirically determined influencing parameters like the number of pressure nodes or the geometry of the nozzle, which had not been explicitly characterized. Therefore, according to Bauckhage (1992) the particle size distribution rarely depends on the viscosity of the molten metal itself. Further investigation of basic procedures and aspects of material science related to the disintegration of metals in an SWA was done by Bauckhage & Schreckenberg (1994); Bauckhage *et al.* (1995, 1996); Andersen *et al.* (1995) and Andersen (1996).

Beside the investigation of metals in an SWA, Reich (1995) focused on molten glass and Hansmann (1996) disintegrated highly viscose fluids. For the prediction of particle size distribution Hansmann (1996) placed a static, circular disk into the sound field and observed the sound forces acting on this disk. The approach was used as a starting point for the qualitative description of the disintegration process.

Since the beginning of the 1990th the institute of *"Chemie und Technologie der Beschichtungsstoffe (CTB)"* from the University of Paderborn used the SWA-technique on powder coatings. It was found that powders generated in an SWA exceed other coatings in terms of an improvement in their optical performance (Holmann, 1994; Goldschmidt *et al.*, 1998; Vestweber, 1999). The influence of different material and process parameters regarding the particle size distribution was investigated by Mattern (1998). Therefore, he measured the sound field using a sensitive sonsor under variation of the sonotrodes' setup, geometry, distance, and angle. Vestweber (1999) investigated the impact of the molecular structure of the employed polymers on the disintegration process. As could be shown, non-Newtonian and visco-elastic behavior of the molten polymer influenced the disintegration process. Therefore, retardation and relaxation of polymers needed to be adjusted with their residence time inside the pressure node of the ultrasonic field in order to achieve small particles. To support the application of polymers on a

surface, the SWA was extended to electrostatically charge the plant. Further, hot air was used to direct the liquid flow (Goldschmidt *et al.*, 1993; Vestweber, 2004).

Although the ultrasonic field has been investigated by sensors as well as the influence of material and process parameters on the generated particle size distribution, little is known about the disintegration mechanism itself. Therefore, an optimization of the process based on an empirical approach is difficult. Thus, Reipschläger (2002) visualized the disintegration of polymer melts in an SWA by means of numerical simulation of the process. He qualitatively found a good agreement between experiment and simulation, but was not able to quantitatively detect the numerically calculated particles in terms of particle size distribution. Since back effects of the liquid on the ultrasonic field have not been accounted, little is said about the disintegration mechanism itself.

6.2. Mechanism of the Disintegration Process

In case of the SWA a lamella is formed between the two sonotrode plates. Therefore, this lamella is antiparallel to the flow direction of the gas phase decreasing with increasing nozzle distance. The product of lamella thickness δ and distance X_l from the nozzle outlet is constant after a certain distance behind the nozzle. It is a parameter for the thickness of the lamella: $\mathrm{K} = \delta X_l$ (Dombrowsi *et al.*, 1960; Fraser *et al.*, 1962). If K is related to the cross-sectional area of the outlet, the lamella number results: $\chi = \delta X_l$ / A. In case of a spherical nozzles $\chi = 4\delta X_l / \pi {d_n}^2$. For experimental as well as for numerical investigations of the disintegration mechanism a nozzle of $d_n = 1.5$ mm is used. Finally, employing a mass flow of 100 g/min and a sonotrode amplitude of 120 μm results in lamellae as shown in Figure 6.4.

Figure 6.4 shows screen shots of simulations of a continuously disintegrating strand of alkydal solution having a viscosity of 10 mPas and 114 mPas. The pictures are focussing on the lamella to emphasize on the procedures around the rim. As can be seen in numerical simulations as well as in experiments, the size of the lamella increases with increasing viscosity. Further, surface waves are observed on the lamellaes' surfaces whose wave lengths increase with increasing distance to the outlet. In case of a viscosity of 114 mPas, the parameter K is calculated as 0.059 cm^2 with a lamella thickness of 220 μm at the outer rim having an axial distance of

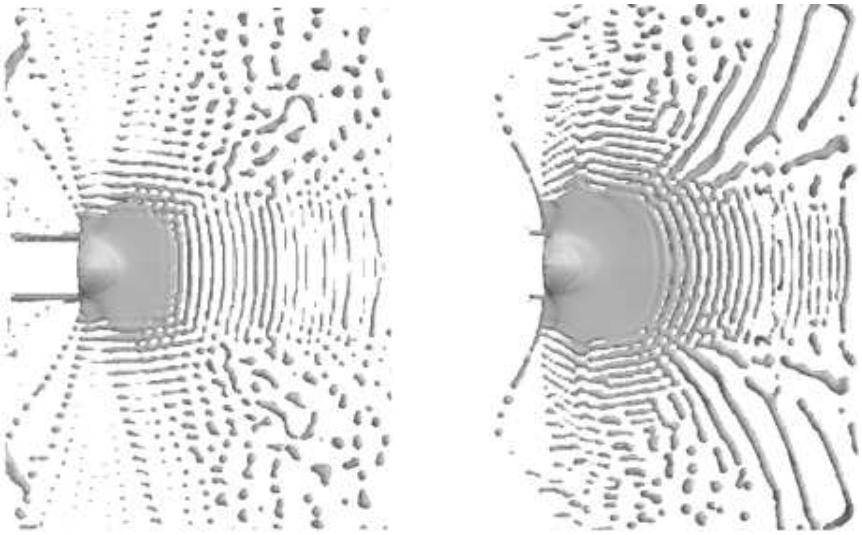

(a) $\mu = 10$ mPas (b) $\mu = 114$ mPas

Figure 6.1.: Numerically generated lamellae at equidistant time-steps in an SWA.

2.7 cm to the outlet. Therefore, χ calculates as 0.034 and $\chi \cdot$ We = 113 regarding eq. (5.1) to calculate We for amplitudes of the axial gas velocity of 205.5 m/s using the nozzle diameter as the characteristic length.

For values of $\chi We < 220$, the lamella is bordered by a bulge at its outer part disintegration into relatively big droplets. For $\chi We > 220$, the lamella will start to oscillate because of the gas forces acting on the lamella's surface. The amplitudes of oscillation rapidly increase with increasing distance to the nozzle and initiate the disintegration of the lamella. This case is called the aerodynamic corrugation. The fragments leaving the lamella form liquid ligaments, which will then break down further by e.g., Rayleigh breakup (Walzel, 1990). Walzel (1990) based his investigations on the breakup of lamellae generated by e.g., hollow cone, deflector, or flat spray nozzles. Instead, in numerical simulation of the continuous disintegration process both mechanisms can be observed: A bulge is formed at the outer rim of the lamella separating ligaments which break down further. This is because not solely aerodynamic forces are responsible for strand disintegration in an SWA. Whereas in common pneumatic atomizers particles of 50 μm are formed not until gas velocities u_g of 300 m/s are reached, an SWA already generates such

particles at, e.g., 200 m/s in case of sonotrodes oscillating at 120 μm. Concluding, the disintegration mechanism of a lamella in an ultrasonic field is not entirely congruent to pneumatic atomizers.

According to Lierke (1995) the disintegration mechanism in an SWA correlates to the aerodynamic atomization of free falling drops. Walzel (1990) compares the disintegration mechanism to a two-phase injector. Instead of the uniform relative velocity u_0 between the droplet and the gas flow, the rms-value u_{max} of the periodically varying sound particle velocity in axial direction needs to be used in case of a continuous disintegration. Since the lamella builds up and disintegrates inside the pressure node, Walzel (1990) used the sound velocity of the corresponding velocity node for his investigations. For the characterization of the continuous disintegration mechanism in an SWA, Lierke (1998) used an altered Weber and the Mach number. As the Weber number he defined

$$\mathrm{We}_{Lierke} = \frac{8 p_B}{p_\sigma} = \frac{\kappa}{\sigma}\, d_d\, P_0\, \mathrm{Ma}^2 \,, \tag{6.2}$$

with p_B denoting the Bernoulli pressure, p_σ the capillary pressure, and P_0 the static pressure at standard conditions. Further, Lierke (1998) assumed the disintegration mechanism to start in terms of instabilities on the liquid surface at $\mathrm{We}_{\mathrm{Lierke}} \approx 8$ for a water drop. As the resulting critical Mach number (Ma_{cr}) for small mass flow rates he calculated

$$\mathrm{Ma}_{cr} \approx 1.69 \sqrt{\frac{\sigma}{P_0\; d_{str,0}}} \,,$$

with $d_{str,0}$ as the initial strand diameter. For a nozzle of 1.5 mm in diameter and a resulting water strand of the same value, the disintegration should start at $\mathrm{Ma}_{cr} = 0.039$ at standard conditions. This mirrors a sound level of 168.8 dB or $u_{max} = 13.4$ m/s, respectively. For the disintegration of polymer strands this approach needs to be altered. As explained previously in Section 5.3, the critical Weber number depends on the Ohnesorg number. Therefore, for a polymer strand having a viscosity of 0.1 Pas, a surface tension of about 0.03 N/m, and a density of 1100 kg/m^3, the dimensionless Ohnesorg numbers calculates as $\mathrm{Oh} = 0.449$ resulting in a critical Weber number of $\mathrm{We}_{cr} = 15.59$. Using this value on eq. (6.2), the critical Mach number for such a polymer results as:

$$\mathrm{Ma}_{cr} \approx 2.34 \sqrt{\frac{\sigma}{P_0\; d_{str,0}}} \,.$$

Therefore, for a polymer strand of 1.5 mm in diameter the disintegration should start at $\mathrm{Ma}_{cr} = 0.033$ at standard conditions. This mirrors a sound level of 166.7 dB or $u_{max} = 11.3$ m/s, respectively. In case of an SWA like the one used during the experiments, such velocities are found in numerical simulation of the oscillating sound field for sonotrode amplitudes of 20 μm. This confirms the results achieved during experimental investigations of the disintegration process as the ones shown in Figure 6.2.

After initiating the disintegration process, small filaments are separated from the rim of the lamella. These liquid ligaments are unstable due to central symmetric waves occurring on their surfaces. These surface waves will grow quite quickly in case of the wave length being $\lambda > \pi d_{lig}$. According to Rayleigh (1879*b*), the fastest growing perturbation has an optimal wave length of

$$\lambda_{opt} = \pi d_{lig} \sqrt{2 + 6\ \mathrm{Oh}}$$

in case of laminar strand disintegration. The resulting particles shall have a diameter of

$$d_p = d_{lig} \sqrt[6]{44 + 6\ \mathrm{Oh}}\ , \tag{6.3}$$

with a narrow particle size distribution. Separated ligaments observed in numerical simulation of the disintegration process do have diameters between 180 and 240 μm. Therefore, according to eq. (6.3) particles with diameters bigger than that should result by secondary breakup of such ligaments. A detailed investigation on generated particles and the particle size distribution obtained in an SWA is done experimentally in Section 6.5 as well as by means of numerical simulation of the disintegration process in Section 6.6.

6.3. Experimental Investigation of the Strand Disintegration

For the disintegration of a continuous liquid strand in an SWA, the liquid is inserted via a nozzle into a pressure node of a high-amplitude resonant sound field. Thus, a quasi-stationary lamella is generated at the top of the nozzle disintegration into ligaments and droplets at its outer sphere. Thereby, discrete droplets with a particle size distribution in the range of 5 to 100 μm are generated. Since the particle size significantly determines the performance of powder coatings, the overall aim is to optimize such a disintegration process in terms of narrow particle size distribution.

Figure 6.2 displays various forms of lamellae at different sonotrode amplitudes. The pictures are taken with a digital camera using a strobe flash ($\sim$ 8 nanosec flash exposure) as back light. For optical reasons, an angle of approximately 40 degrees had to be chosen which leads to an ellipsoidal form of the lamella on the photograph. A solution of alkydal in xylol is used as a model liquid, since alkydal is a common feedstock in the coating industry. This solution has a viscosity of 0.1 Pas, a surface tension of about 0.03 N/m and a density of 1100 kg/m^3. The mass flow rate is adjusted to be 100 g/min.

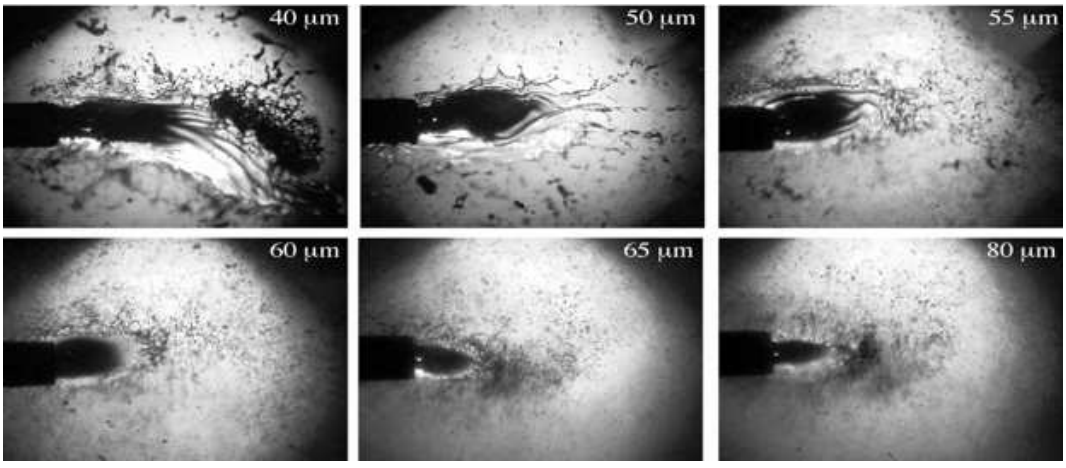

Figure 6.2.: Disintegration of a continuous liquid strand of an alkydal solution at various sonotrode amplitudes.

At small sound amplitudes relatively big, unsteady lamellae result which dis-

integrate mainly outside the pressure node. Therefore, the flattened liquid strand intensively acts as a reflector for the impinging sound waves. This destroys resonance and results in poor disintegration with a considerable amount of large liquid ligaments. Not until a minimum amplitude is reached depending on the fluids properties and on process parameters, a continuous disintegration with a considerable small quasi-stationary lamella is achieved. This small lamella is situated inside the pressure node and, therefore, hardly effects the sound field. Thus, for sonotrode amplitudes above 60 μm particle size distribution in the desired range of 5 to 50 μm is obtained at the given flow rate. In case of an alkydal solution the generated particles are detected by a *LD* (Laser Diffraction) method and their size distribution is measured under the given operational and material conditions (see Section 6.5 for more details). This procedure enables a quantitative comparison between experimental data and numerical simulation of the disintegration process. In case of polymers used for the production of powder coatings, the generated particles are pre-sorted by a cyclone and measured later on.

During operation of the pilot plant, undesired fouling of the sonotrodes' faces occurs caused by advected liquid particles along the axial direction. In general, generated particles occupy the whole region between the sonotrodes in addition to their main flow direction. This effect is mainly caused by acoustic streaming appearing in sound fields of high intensity (Trinh, 1986; Lee & Wang, 1990). Focussing on outer acoustic streaming, in contrast to, e.g., near-boundary acoustic streaming (Lee & Wang, 1989), the effect can be generalized into two common types. The first mechanism is caused by friction between the gas phase and a solid wall if the former is vibrating in contact with the latter. This can be the case for, e.g., a standing wave in a resonant area. The second type happens due to the spatial attenuation of a plane wave in free space, e.g., a plane traveling wave. The mean energy density of a wave motion is decreasing due to absorption inside the medium. Since this energy is transformed into kinetic energy, a convective flux results affecting the particle track of droplets inside such sound fields. Thereby, the flow direction of such outer acoustic streams coincides with the propagation direction of the sound wave. Trinh (1986) quantitatively investigates outer acoustic streaming by means of an oscillation-reflection unit. The resulting flow profile shows two adjacent swirls rotating in opposite direction. The velocities of such

swirls are found to be in the range of 0.003 m/s for small sound field amplitudes. Since for the disintegration in an SWA much higher amplitudes are applied, higher velocities of the corresponding acoustic streaming result causing the transport of particles along the axial direction.

6.4. Numerical Investigation of the Strand Disintegration

For numerical simulation of the disintegration process of a continuous liquid strand, the nozzle was implemented as a cylindrical patch into the computational domain of *FS3D* with no-slip conditions at its lateral walls. The inlet boundary condition is a Poiseuille flow with parabolic velocity profile. Calculations were done assuming symmetry with respect to the xz-plane (cf. Figure 6.4). For accurate approximation of the free liquid surface during strand disintegration, the computational domain covers a rectangle of $0.5 \times 1 \times 1$ cm along the x,y,z directions containing up to 16 million grid cells.

Figure 6.4 shows a screen shot of a simulation of a continuously disintegrating strand of alkydal solution, as it was used in previous experiments (cf. Figure 6.2). The nozzle has a length of 2 mm, an inner diameter of 1.5 mm and is placed 2 mm ahead of the central pressure node in the radial direction. The mass flow rate is 100 g/min. As determined experimentally and confirmed by numerical simulation, the liquid outlet should be shifted by 1 to 2 mm in radial direction away from the sound field's axis in order to generate smaller polymer particles. This is because the liquid's residence time in the area of high pressure gradients is maximal then. After a short transient period quasi-stationarity is achieved. The liquid strand leaving the nozzle will then be flattened into a lamella by the ultrasonic forces. At the rim of the lamella ligaments and droplets are separated. The more viscous the polymer or the smaller the applied sonotrode amplitude is, the more ligaments occur (cf. Figure 6.1). On the left-hand side of the lamella shown in Figure 6.4 a liquid film is formed which wets the nozzle. Since the lamella expands to an almost circular disk, part of the liquid droplets move opposite to the inflow direction during disintegration. This negative effect is also observed in experiments at the pilot plant

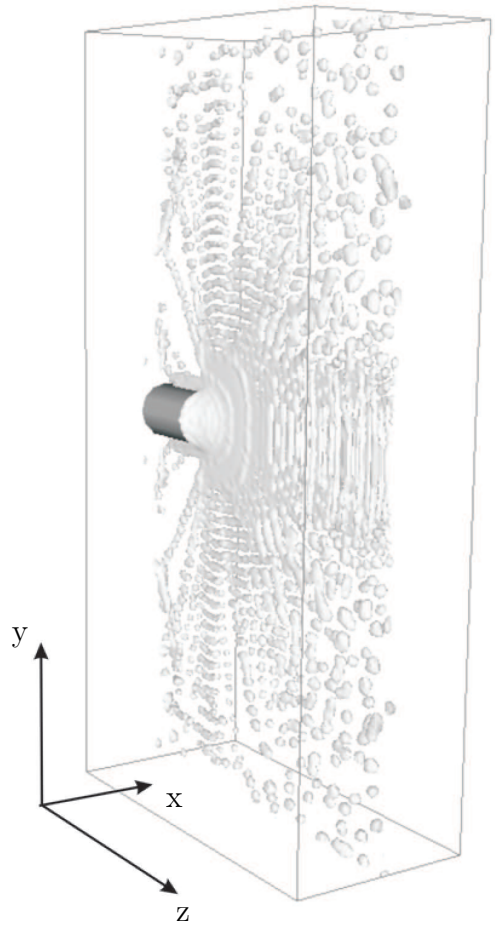

Figure 6.3.: Simulation of strand disintegration.

and causes material loss. When ligaments and droplets move away from the lamella after separation, secondary breakup will occur leading to the generation of smaller particles. This so-called Rayleigh breakup is caused by aerodynamically induced disturbances on the liquid's surface. It leads to contractions which finally result in the stripping of droplets, caused by capillary forces. To account for such disturbances during numerical simulation, white noise is added to the acoustic forces leading to smaller particles.

In contrast to experimental investigations as conducted in Section 6.3, the continuous strand disintegration as performed by numerical simulations takes place mainly along the xy-plane. Instead, in experiments outer acoustic streaming leads to undesired fouling of the sonotrodes' faces by advecting liquid particles along the axial direction. Here, particles move along in axial and tangential direction between

the sonotrodes occupying the whole region. This behavior is missing in numerical simulations due to inexistent acoustic streaming as described in Section 6.3. This effect causes convective fluxes which divert the particle track especially of small droplets. Since the effect of ultrasonic streaming takes place on a time scale of multiple oscillation cycles of the sound field (Lee & Wang, 1990), it cannot be taken into account during numerical simulation of the ultrasonic field. Due to limitation in the *CFX*-solver, the transient sound field is only calculated for real-times of up to 2 ms. Nevertheless, since acoustic forces of the superposed ultrasonic field exceed outer acoustic streaming by orders of magnitude, resulting forces caused by ultrasonic streaming are of no significance for the disintegration mechanism itself.

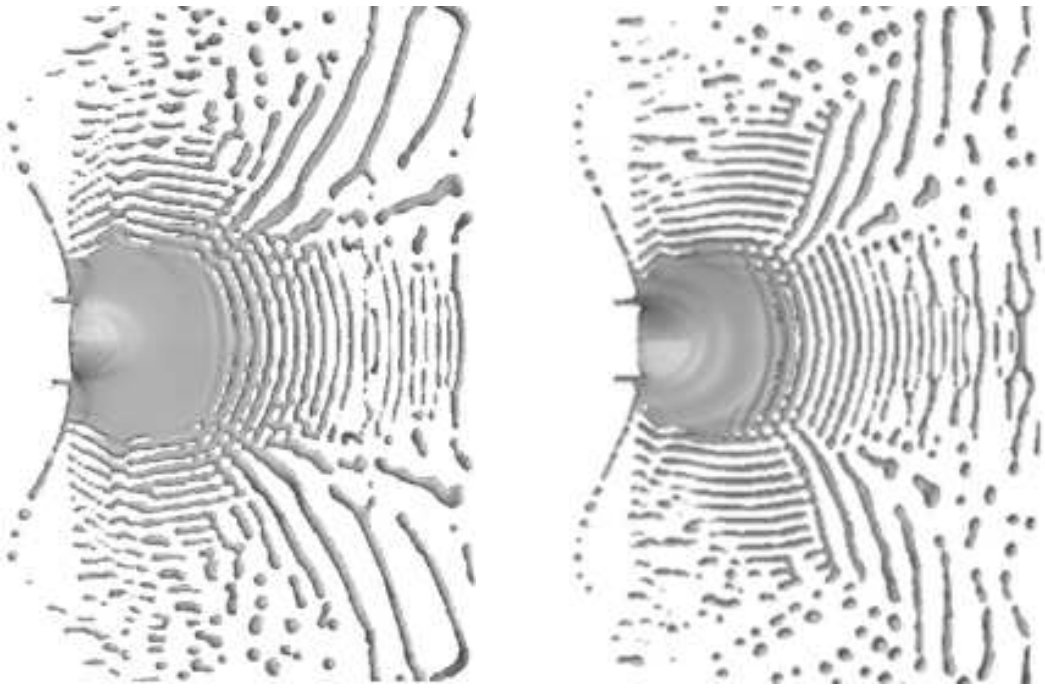

(a) Newtonian liquid (b) Non-Newtonian liquid

Figure 6.4.: Comparison between Newtonian and non-Newtonian fluids with $\mu = 114$ mPas at equidistant time-steps in an SWA.

The polymer melts for the production of powder coatings show a non-Newtonian flow behavior. A modified Carreau model is, therefore, employed to describe the concrete liquid (Appendix C). This model takes into account the shear thin-

ning behavior of polymers, i.e. the viscosity decrease caused by an increase in shear rate $\dot{\gamma}$:

$$\mu = \frac{\mu_0}{1 + \frac{\mu_o}{K}\,\dot{\gamma}^{1-n}} \,, \quad \text{with } \dot{\gamma} = \sqrt{2\text{tr}(\mathbf{D}^2)} \quad \text{and } D_{xy} = \frac{1}{2}\left(\frac{\partial u}{\partial y} + \frac{\partial v}{\partial x}\right) \,,$$

where $\mathbf{D}$ denotes the rate of deformation. A shear-thinning liquid attains lower viscosities during droplet collision. This leads to a larger maximum diameter of the generated collision complex compared to Newtonian droplet collision (Motzigemba *et al.*, 2002). During disintegration these lowered viscosities mainly lead to smaller particles due to a lower value of We_{cr}. As can be seen in Figure 6.4, the lamella calculated including the modified Carreau model significantly differs from the one without considering the shear shinning effect. The extension of the lamella in Figure 6.4(a) is considerably smaller than the one in Figure 6.4(b). Since the reduced critical We number supports the earlier stripping of droplets and ligaments from the periphery of the lamella, the circumference of the lamella will decrease. Similarly, Rayleigh breakup is supported as well appearing in shorter ligaments and an earlier collapse of these ligaments, respectively. Therefore, overall a better atomization of the disperse phase occurs.

6.5. Experimental Determination of the Particle Size Distribution

The probabilities of particle sizes analyze (*PSA*) in sprays including the advantages and disadvantages of the particular measurement method have been discussed in literature before (Lefebvre, 1989; Bachalo, 2000; Yule & Dunkley, 1994). Choosing the best method for the particular problem includes diverse considerations: The method needs to guarantee the measurement of a representative sample, the detected particle size has to be independent of the measurement angle or distance, and the measurement especially needs to be non-invasive. Thus, the method shall enable the measurement of the particle size distribution (*PSD*) without affecting either the disperse or the continuous phase. Hence, the disintegration process in general should not be altered by the measurement technique. Finally, the determination of the *PSD* has to be reproductive.

The laser diffraction (*LD*) technique is found to be the most reliable method for the measurement of *PSD* in powder coating technology (Hewitt, 1993; Scholz, 1998; Corbeels, Senser & Lefebvre, 1992). The idea of measuring particle size using this physical principle is based on the effect of particles interacting with light (Frauenhofer, 1817). Light of a laser beam is focused in the center of a multielement-detector. Thus, the scattering effect at the edges of a particle leads to signals on the non-central elements of the detector. Generally, the smaller the particles are the larger the resulting diffraction angles. Diffraction at small angles, however, can only be recognized by the system if the scattered light is not focussed to the central elements where all the unscattered light is collected. The optical setup used is referred to as Fourier-optics (Heuer & Leschonski, 1985).

The instrument applied for *PSA* is a *Helos-Vario/KF (Sympatec Co.)*. The device holds a 5 mW He-Ne-laser ($\lambda = 632.8$ nm) which can be expanded up to 13 mm in diameter. The diffraction pattern resulting during the measurement is pictured by a *Fourier* lens on the central detector. Using this specific type of lens, equally sized particles are recognized by the detector regardless their position in the measuring field. The lens has a focussing length of 500 mm and, therefore, detects particles between 4.5 and 875 μm.

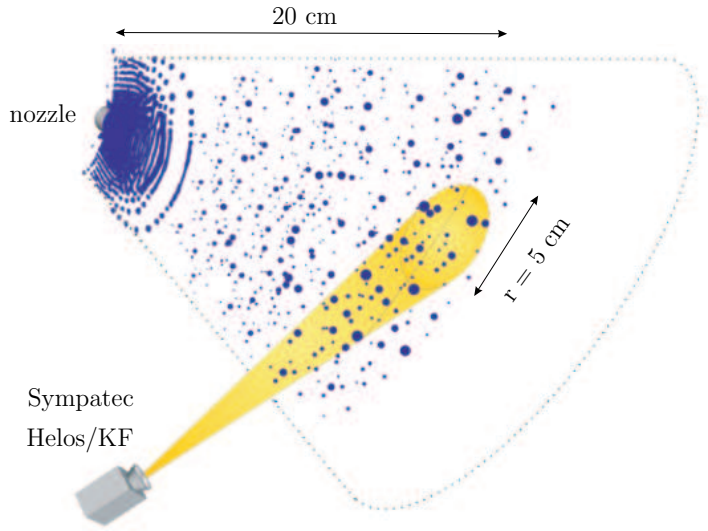

Figure 6.5.: Setup for detection of the particle size distribution in a *PSA* system.

For the detection of *PSD* the *LD* apparatus is placed approx. 20 cm in front

of the nozzle of the SWA, orthogonal to the lamella of the exiting polymer strand (cf. Figure 6.5).

For a sonotrode amplitude of 80 μm, a mass flow rate of 100 g/min, and a sonotrode angle of 2 degrees, the particle size distributions of different atomized alkydal solutions in xylol are investigated. The viscosity of each sample is altered by changing the mixing ratio of the same alkyd resin in xylol. Each data set is measured over a period of 200 ms and averaged over 20 cycles. The resulting particle size distributions for different viscosities are shown in Figure 6.6.

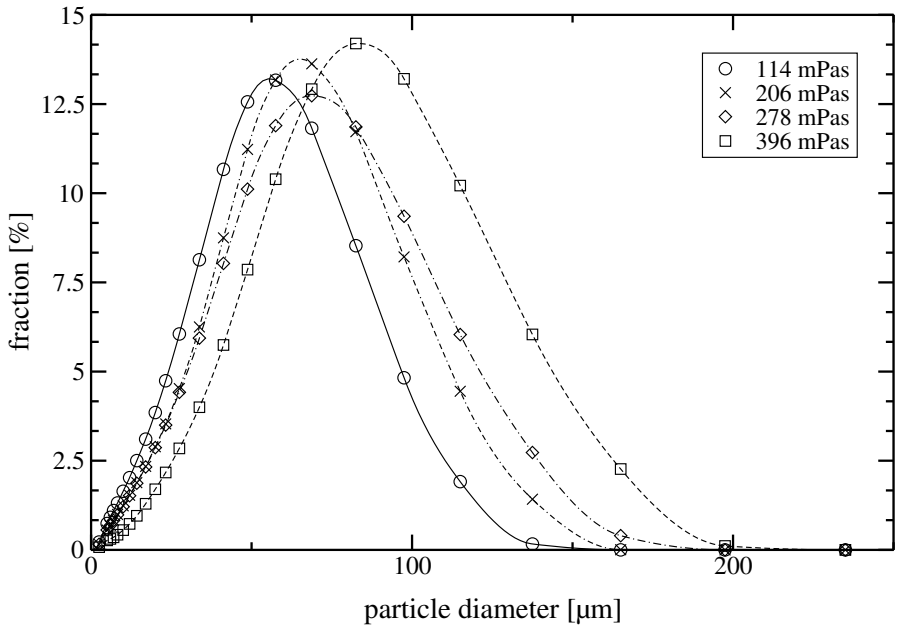

Figure 6.6.: Experimentally determined *PSD* at a sonotrode amplitude of 80 μm.

As can be seen in Figure 6.6, the particle size in general decreases with decreasing viscosity of the liquid. More specific, for a viscosity of $\mu = 114$ mPas averaged over multiple test series the following quantities are found during disintegration:

Table 6.2.: Characteristic values of an experimentally obtained *PSD* for a polymer of $\mu = 114$ mPas at 80 μm.

d_{32}	d_{RRSB}	$d_{v.0.5}$	d_{max}	$d_{v.0.5}/d_{32}$	$d_{max}/d_{v.0.5}$
23.32	54.95	45.97	135.43	1.97	2.95

In comparison to Table 6.1, physical dimensions of particles generated by an SWA are in the same range as droplets manufactured by other atomizers. Instead, particle size distributions obtained in an SWA are more disperse than e.g., generated in a rotational atomizer.

6.6. Numerical Determination of the Particle Size Distribution

To quantitatively analyze the disintegration of polymers in an SWA, particle size distributions of the disintegration process need to be calculated. Therefore, every single value of the VOF variable $f_{i,j,k} > 0$ characterizing the disperse phase needs to be detected and associated with a droplet. This is done by a recursive algorithm which is established and incorporated into the program code of *FS3D* (cf. Appendix B). The algorithm detects the value of an arbitrary cell. In case of $f_{i,j,k} > 0$ it recursively scans the surrounding cell volumes until it reaches an empty cell next to the boundary of a droplet characterized by $f_{i,j,k} = 0$. Since the algorithm works on the whole calculation domain scanning every cell, it detects all droplets present. The reconstruction of a single droplet is then done by combination of the adjacent cells of $f_{i,j,k} > 0$. Finally, the droplet volume is calculated as the sum of all cell volumes the particle is made of:

$$V_d = \sum_{i,j,k} f_{i,j,k} \cdot V_{cell}(i,j,k), \quad \text{with} \quad V_{cell}(i,j,k) = \triangle x_i \triangle y_j \triangle z_k \; . \tag{6.4}$$

Based on the calculated volume of the droplet the equivalent, spherical radius ($R_{d,s}$) is determined as

$$R_{d,s} = \sqrt[3]{\frac{3}{4}\pi V_d} \; . \tag{6.5}$$

As well the components of the velocity vector for each droplet are calculated. For the component u it follows

$$u = \frac{\sum_{i,j,k} u(i,j,k) \cdot f(i,j,k) \cdot V_{cell}(i,j,k)}{\sum_{i,j,k} f(i,j,k) \cdot V_{cell}(i,j,k)} \; , \tag{6.6}$$

denoting the mass-averaged velocity as the ratio of the momentum flux over the droplet's mass. The values for v and w are calculated alike u. For the exact

position of each droplet inside the calculation domain, the center of the droplet is determined as 3-D coordinates against x,y,z:

$$x = \frac{\sum_{i,j,k} x_i \cdot f(i,j,k) \cdot V_{cell}(i,j,k)}{\sum_{i,j,k} f(i,j,k) \cdot V_{cell}(i,j,k)} \ . \tag{6.7}$$

The values for y and z result equally. Concluding, the exact position, velocity, and volume of each droplet at every time-step in the calculation domain is known. Notice also, that the accuracy of these calculated values strongly depends on the discretization of the calculation domain. The PLIC algorithm (see Section 3.3) itself is not able to separate the particles. Two areas characterizing a droplet will be recognized as disconnected, independent volumes inside the VOF code not until a single cell of $f = 0$ does separate them (Figure 6.7). Hence, the more grid cells the computational domain is made of and the smaller the physical cell dimensions are, respectively, the more accurate the determination of the particle volume and, therefore, the *PSD* will be.

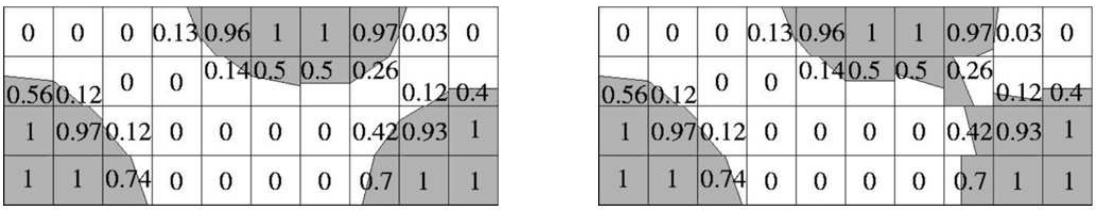

(a) droplets apparently separated

(b) droplets conjunction

Figure 6.7.: Failed separation of two droplets by the PLIC algorithm.

Based on this routine, the *PSD* for various alkydal solutions has been analyzed by numerical simulation of the disintegration process. The liquid system used for disintegration is an alkyd resin in xylol as described in Section 6.3. By varying the mass fraction of alkydal in xylol, the viscosity of the mixture is altered, whereas the surface tension of 0.03 N/m and the density of about 1100 kg/m^3 are roughly kept constant. As can be seen in Figure 6.8, less viscous materials result in smaller particles during disintegration consistent with experimental investigations (cf. Figure 6.6). Each data set is calculated over a period of 23 ms with particle sizes obtained every 1 ms. Comparison of these particle size distributions derived

by numerical simulations with experimental data for identical liquid systems and similar operational conditions reveals that particles generated by numerical simulations are larger than those obtained during experiments. On the one hand, this is due to the fact that during simulation the particle size is - in contrast to experimental measurement - detected near the boundary of the computational domain rather close to the lamella. At this early stage of the disintegration process secondary breakup is still not complete. On the other hand, polymer phase effects on the sound field have been neglected in numerical calculations.

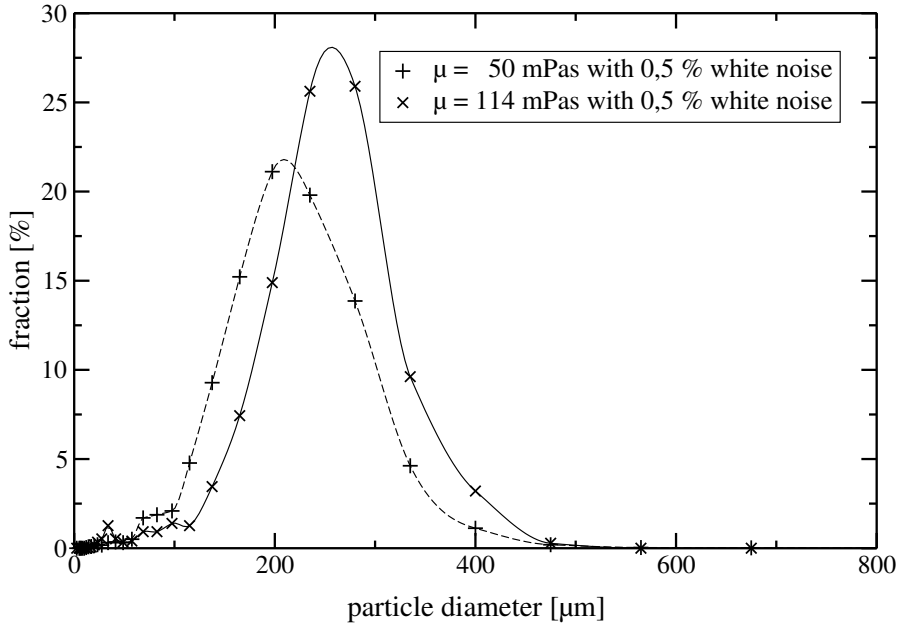

Figure 6.8.: Numerically determined *PSD* at a sonotrode amplitude of 120 μm.

In addition, due to the latter fact polymers of about $\mu = 0.1$ Pas easily disintegrate in sound fields generated by sonotrode amplitudes of 80 μm during experimental investigations of the atomization process. Instead, for numerical disintegration of a continuous liquid strand of molten polymer of $\mu = 0.1$ Pas, sonotrode amplitudes of 120 μm are necessary to let qualitatively similar atomization occur. If back effects of the polymer phase on the sound field are neglected, the Bernoulli effect causing local velocity peaks and an impact pressure at the lamella's pole are neglected as well. These have been identified in Section 5.3 as the main impact on the atomization process in an ultrasonic standing wave field beside the acoustic radiation pressure. Therefore, higher sonotrode amplitudes need to be applied

during numerical simulation to mirror experimental behavior.

Further, so far the effect of beats of ultrasonic fields on the *PSD* has been neglected as well. Such beats are caused by swapping of oscillations having slightly different frequencies (Section 4.7). Thus, their overall phase shifts slowly resulting in maxima and minima (Heywang *et al.*, 1992). As a result, the beat of an ultrasonic field causes enlarged particle size distributions. Since time-averaged pressure and velocity fields are read into *FS3D* to model the real gas-liquid jump conditions, effects of such beats of an ultrasonic sound field on the atomization process are vanished during numerical simulation. In contrast, experimental measurements of the *PSD* as performed in Section 6.5 capture the effects of such beats. The time necessary to pass a single beat period is calculated to be 4.3 ms according to $T = 1/\triangle f$. Since data are taken over a period of 200 ms and averaged over 20 cycles, multiple beats alter the general droplets size during data acquisition.

To quantitatively compare particle size distribution obtained during numerical simulation of the disintegration process and experiments, characteristic values for a alkydal solution in xylol having a viscosity of 114 mPas are listed in Table 6.3. These data correspond to a mass flow rate of 100 g/min, a surface tension of 0.03 N/m and a density of 1100 kg/m^3.

Table 6.3.: Characteristic values of a numerically obtained *PSD* for a polymer of $\mu = 114$ mPas at 120 μm.

d_{32}	d_{RRSB}	$d_{v.0.5}$	d_{max}	$d_{v.0.5}/d_{32}$	$d_{max}/d_{v.0.5}$
148.3	257.2	197.1	449.8	1.33	2.28

A detailed, quantitative comparison between characteristic values of a polymer with identical liquid parameters applied in experiments as well in numerical simulations approves earlier conclusion. Comparing quantities of Table 6.2 and Table 6.3 shows that particles generated in numerical simulations of the disintegration process are significantly bigger than those from experiments. In contrast to Table 6.2, the width of the *PSD* by numerical experiments is smaller, i.e. the ratio of $d_{v.0.5}/d_{32}$ is considerably closer to unity. This emphasizes the influence of beats of the ultrasonic field on the disintegration process which effect is missing in

numerical simulations. Thus, such an effect will cause an enlarged *PSD* in experiments as denoted by a ratio of $d_{v.0.5}/d_{32}$ close to two (cf. Table 6.2).

During disintegration ligaments moving away from the lamella are subject to secondary breakup (see Section 6.2). Due to instabilities on the ligaments surface (Rayleigh, 1879*b*), such objects will break down further. Separated ligaments observed in numerical simulation of the disintegration process do have diameters between 180 and 240 μm. Therefore, according to eq. (6.3) particles with diameters bigger than that should result by secondary breakup of such ligaments. Using these values of ligament diameters on eq. (6.3), a potential range of resulting particle diameters between 341.6 to 455.4 μm calculates. As can be seen, the diameter of $d_{Rayleigh} = 455.4$ μm mirrors the maximum diameter of particles found during numerical simulation of the disintegration process with $d_{max} = 449.8$ μm very well. Since d_{max} is defined to match 99.7 % of all generated particles (Vestweber, 2004), outliers are specifically excluded in statistics which are even closer to $d_{Rayleigh}$. As a matter of fact, secondary breakup due to Rayleigh effects is one mechanism during strand disintegration influencing the overall process. As stated by Walzel (1990), aerodynamically induced disturbances accounting for Rayleigh breakup are superposed by other mechanisms. Therefore, a wide range of droplets results in an SWA, especially since the acoustic radiation pressure generated by the ultrasonic standing wave field permanently acts on the liquid's surface.

7. Conclusions and Future Perspective

> *"The known is finite, the unknown is infinite; intellectually we stand on an islet in the midst of an illimitable ocean of inexplicability. Our business in every generation is to reclaim a little more land."*
>
> Thomas Henry Huxley (1825-1895)

A mathematical/computational approach is developed that allows for the numerical simulation of the atomization of polymer melts in ultrasonic standing wave fields. The main difficulties lie in the largely different time and length scales of the ultrasonic sound field and the liquid dynamics on the one hand and the highly nonlinear behavior of the interface including topological changes on the other hand. The model involves a one-way coupling between a compressible single-phase gas flow, corresponding to the resonant sound field, and the droplet dynamics given by a free surface flow. Ultrasonic forces acting on the fluid surface are computed as time-averaged momentum fluxes through a face situated in the sound field that coincides with the gas-liquid phase boundary. The use of time-averages is necessary to reduce computational effort and is justified by the different time scales of ultrasonic field and liquid deformation. The model and the numerical simulations are validated by means of levitator experiments. The simulations allow a qualitative description of droplet deformation and atomization in a single axis standing wave levitator. Taking into account back-effects of a droplet on the ultrasonic field, quantitative predictions of droplet radii with respect to sonotrode amplitude are possible, mirroring the real behavior very well. Because of the much higher complexity, numerical simulation of liquid strand disintegration in an SWA cannot take into account effects of the liquid phase on the ultrasonic field. Therefore, so far simulations only allow for a qualitative description of the disintegration process. Nevertheless, significant trends in strand disintegration can be observed as it is demonstrated by particle size distributions. The latter are important for industrial

use, reflecting the correlation between variations in operational parameters, material properties, and particle sizes. Thus, based on these results optimizations of our laboratory plant and the process itself are now possible.

An advantage of the decoupling of the simulation process into non-linear acoustic sound field and free fluid surface is the ability of applying specialized numerical methods which fit the particular needs. As a result, detailed investigations on the sound field have been performed which allow precise predictions about sound field behavior under variation of operational parameters as sonotrode angle, distance, or curvature. This is an import fact due to other investigation techniques e.g., inserting microphones into the sound field, being invasive and therefore, falsify the results of measurement. Although the impact of the sound field on the disintegration process is still not totally understood, it offers the possibility of predicting trends in particle size distribution. Since the variations in sonotrode geometry and operational conditions are the main time-consuming and costly part of the overall atomization process, it is a significant improvement in optimization of the continuous liquid strand disintegration.

In addition, detailed investigations on the deformation and disintegration mechanism of single liquid droplets as well as continuous strands in an ultrasonic standing wave field have been performed. As could be shown, the mechanism of disintegration is mainly dominated by acoustic forces (e.g., sound pressure and Bernoulli pressure) and aerodynamic forces (e.g., Rayleigh breakup) closely localized around an obstacle. Therefore, ultrasonic forces acting on the fluid surface are computed as fluxes through a face situated in the sound field that coincides with the phase boundary. On the one hand, acoustic forces as the Bernoulli effect cause higher velocities at the droplet's equator corresponding with a lower pressure here which pulls at the droplet. A suction results improving the rate of deformation and disintegration. On the other hand, aerodynamic forces induce disturbances on the liquid surface. If a liquid drop becomes considerably flat, oscillation establishes a mechanism for parametric excitation and growth of capillary waves on the droplets surface. Further, during strand disintegration surface waves are found on the lamella as well. Especially the impact of aerodynamically induced disturbances on secondary breakup can be observed in the strand disintegration process.

Future Perspective

Numerical simulations of the overall disintegration process show significant trends as demonstrated by particle size distributions. Thus, based on these results optimizations of our laboratory plant is started in close cooperation with the mechanical engineering and the electrical engineering group. In a first step, the transducer unit has been modified and a new electronic amplifier has been made. As a result of numerical simulations of the ultrasonic field, frequency shifts due to heating and the beat of the ultrasonic field due to frequency differences of the transducers shall be avoided. Therefore, the new equipment allows a direct control of the system during operation of the pilot plant to vanish these undesired effects. In addition, due to perceptions made during simulation of the ultrasonic field with different sonotrode curvature, sonotrodes with less curvature are produced to generate a 5-node pressure field. Such a geometry leads to an increase in pressure amplitude in numerical simulations. The implementation of these potential optimizations on the disintegration process are in progress.

To quantitatively describe the numerical simulation of liquid strand disintegration in an SWA, back-effects of the disperse phase on the ultrasonic field need to be considered. Due to the enormous complexity of the strand disintegration, numerical simulations of the overall process cannot take into account effects of the disperse phase on the ultrasonic field. Therefore, a simplifying model needs to be established mirroring the back-effect of a liquid on the sound field during numerical simulation of the free fluid flow. For it, a precise understanding of the overall deformation and disintegration mechanism is essential. This thesis gives a first impression of such mechanisms close to the lamella to gain the knowledge needed.

So far, ultrasonic forces acting on the fluid surface are computed as time-averaged momentum fluxes. The use of time-averages is necessary to reduce computational effort and is justified by the different time scales of ultrasonic field and liquid deformation. Nevertheless, although the disperse phase does not react on every oscillation of the ultrasonic field, its particle size distribution depends on the overall beat of the ultrasonic field. To mirror this behavior in numerical simulation of the disintegration process, multiple time-dependent sound fields need to be read into *FS3D* which may still be averaged over an acoustic cycle. Thereby, the shift in

pressure amplitude due to beats is considered with respect to the reaction time of the liquid phase. Thus, the impact of such an effect on the particle size distribution can be included in numerical simulations.

A. Mathematical Supplement

A.1. Stokes Theorem

Consider an arbitrary smooth surface A enclosed by the boundary curve C. Using *Stokes* theorem transfers the line integral over C of the vector field to a surface integral of a vector field:

$$\oint_C d\mathbf{s} \times \sigma\mathbf{n} = \int_A (\mathbf{n} \times \nabla) \times \sigma\mathbf{n}\, dA \; .$$

A.2. Gaussian Divergence Theorem

Gauss's divergence theorem states that if V is a volume with surface A and if ϕ is a differentiable vector field then

$$\int_V \nabla \cdot \phi \, dV = \int_A \phi \cdot \mathbf{n} \, dA \; .$$

Here $\mathbf{n}$ is the outward normal to the surface of the volume at a given point on the surface and $\nabla \cdot \phi$ the divergence of ϕ denoting the source density inside the volume V.

A.3. Delta Distribution

The one-dimensional delta distribution δ can, e.g., be defined as the limit of a function:

$$\delta(x) = \lim_{\alpha \to \infty} \sqrt{\frac{\alpha}{\pi}}\, e^{-\alpha x^2} \; .$$

Here the limiting value is not meant pointwise but understood as follows:

If a continuous function $f(x)$ is multiplied with the delta distribution δ, an integration over the real part of the axis results in the value of that function at $x = 0$.

i.g.

$$\int_{-\infty}^{+\infty} f(x)\delta(x)dx = f(0) \; . \tag{A.1}$$

The delta function is no function in the common sense since for all $x \neq 0$ eq. (A.1) the limit becomes zero. Nevertheless, for the integral of the function it arises

$$\int_{-\infty}^{+\infty} \delta(x)dx = 1 \; .$$

Dirac's delta distribution results by derivation of Heavyside's jump condition H:

$$H(x) = \begin{cases} 0 & x < 0 \\ 1 & x \geq 0 \end{cases} \quad .$$

B. Recursive Algorithm

B.1. Definition

A recursive algorithm is an algorithm which calls itself with "smaller (or simpler)" input values, and which obtains the result for the current input by applying simple operations to the returned value for the smaller (or simpler) input. More generally if a problem can be solved utilizing solutions to smaller versions of the same problem, and the smaller versions reduce to easily solvable cases, then one can use a recursive algorithm to solve that problem. For example, the elements of a recursively defined set, or the value of a recursively defined function can be obtained by a recursive algorithm.

If a set or a function is defined recursively, then a recursive algorithm to compute its members or values mirrors the definition. Initial steps of the recursive algorithm correspond to the basis clause of the recursive definition and they identify the basis elements. They are then followed by steps corresponding to the inductive clause, which reduce the computation for an element of one generation to that of elements of the immediately preceding generation.

In general, recursive computer programs require more memory and computation time compared with iterative algorithms. Instead they are simpler and for many cases a natural way of thinking about the problem. To reduce computational time and memory usage the recursive algorithm explained subsequently has also been turned into an iterative approach. Since it is much more complex, it is forbeared here from going into more detail.

B.2. Structure

The determination of single droplets inside the calculation domain is done by the routine **'droplet'**. The code for the determination of single droplets takes as input parameters the grid structure in three dimensions as the number of grid cells in each direction (*nk*, *nj*, *ni*) and the VOF-values inside the domain with respect to the cell index ($f_{i,j,k}$).

ROUTINE **'droplet'**
INPUT (ni, nj, nk, f)

By looping over the whole calculation domain cells which $f_{i,j,k} > 0$ are predetermined by the Boulian operator *B=.true.* versus *R=.false.* for $f_{i,j,k} = 0$. These variables (*B,R*) are incorporated into the code as logical operators:

```
1  B=.true.
2  R=.false.
3       for  i ← 1 to ni
4       for  j ← 1 to nj
5       for  k ← 1 to nk
6         if  f(i,j,k) > 0   then
7           B(i,j,k) = .true.
8         else  R(i,j,k) = .false.
9         endif
```

After characterizing each cell by B or R, respectively, the loop is starting all over but checking for the logical operator instead. In case of B being true, the subroutine **'merge'** is called as a recursive algorithm who analyzes the cells around the previously investigated grid cell (*i,j,k*):

RECURSIVE SUBROUTINE **'merge'**

INPUT (i, j, k, f, B, R)

```
 9    for  ii ← (i − 1) to (i + 1)
10    for  jj ← (j − 1) to (j + 1)
11    for  kk ← (k − 1) to (k + 1)
12         if   B(ii, jj, kk) = .true.
13              call → 'Calculation'
14              call → 'merge'
15         else  R(ii, jj, kk) = .false.
16              exit → termination condition
```

As long as *B=.true.* the algorithm calls itself and calculates (**'Calculation'**) the demanded values according to eq. (6.4), (6.5), (6.6) and (6.7). Therefore, all grid cells (*i,j,k*) having adjacent cells of $f_{i,j,k} > 0$ are merged. In case of $f_{i,j,k} = 0$ and *R=.false.*, respectively, the algorithm terminates the loop and leaves the RECURSIVE SUBROUTINE **'merge'**. Therefore, it goes back to its initial position and continuous the previous loop inside the ROUTINE **'droplet'** until all grid cells in the calculation domain are scanned. Finally, every VOF-variable with $f(i, j, k) > 0$ will be associated with an area denoting a droplet. Further, the coordinates of the center of the droplet, the corresponding components of the velocity vector (*u,v,w*), the and its spherical radius ($R_{d,s}$) are quantified and read out.

OUTPUT $(x, y, z, u, v, w, R_{d,s})$

C. The Modified Carreau Model

The viscosity of a fluid represents the material's internal resistance to deform. It is mathematically defined as the ratio of shear stress τ and shear rate $\dot{\gamma}$:

$$\eta \equiv \frac{\tau}{\dot{\gamma}} \tag{C.1}$$

In general, fluids can be classified as either Newtonian if the relation of eq. (C.1) is linear or non-Newtonian. In the first case η is a constant independent of $\dot{\gamma}$. Viscosity is a fluid property easily measured by, e.g., extrusion viscometers, capillary or parallel plate rhometers.

For polymeric liquids the viscosity depends on the shear rate. Therefore, the viscosity curves depend on the following properties:

1. $\lim_{\dot{\gamma}\to 0^+} \eta = \eta_0$ with η_0 denoting the zero shear viscosity.

2. $\eta(\dot{\gamma})$ is a decreasing function of $\dot{\gamma}$. This behavior is called "pseudo-plastic" or shear-thinning.

3. The experimental measurement of zero shear viscosity is not possible for the employed polymers using available tools.

Viscosity measuring provides experimental data at a given temperature consisting of several data points on the viscosity curve. These data are then fitted to the viscosity model of Carreau

$$\mu = \frac{\mu_0}{1 + \frac{\mu_o}{K}\,\dot{\gamma}^{1-n}}\ , \tag{C.2}$$

with K denoting the critical shear stress roughly characterizing the transition shear stress from Newtonina to the pseudo-plastic region. Further, n represents the shear rate sensitivity with $0 < n < 1$.

Therefore, the overall aim of data fitting is to derive the three parameters η_0, K, and n according to eq. (C.2). For this purpose, a solution of alkydal in xylol (percent by weight: 45 %) is used with a surface tension of about 0.03 N/m and a density of 1100 kg/m^3 at standard conditions. The fitting of the experimental data under consideration of eq. (C.2) leads to $\eta_0 = 0.114$ Pas, $K = 9.83329$, and $n = 0.898479$.

Applying these data to *FS3D* quantitatively leads to smaller particles during disintegration (see Section 6.4 for more details). Qualitatively, using the modified Carreau model causes reduced lamella extension in comparison to the Newtonian approach with a constant viscosity set to $\eta = 114$ mPas. Further, the viscosity inside the lamella changes with the lamella radius. As can be seen in Figure C, the viscosity decreases with increasing distance of the lamella from the nozzle. Since shear rate correlates with the ultrasonic forces acting on the fluid surface, the shielded liquid inside the lamella is found to have higher viscosities. Corresponding phenomena are found for droplets and ligaments moving away form the lamella. In addition, the bulge formed at the rim of the lamella can clearly been seen in Figure C for $r = 0.2$ mm due to higher viscosities inside such a bulge in contrast to the flattened lamella.

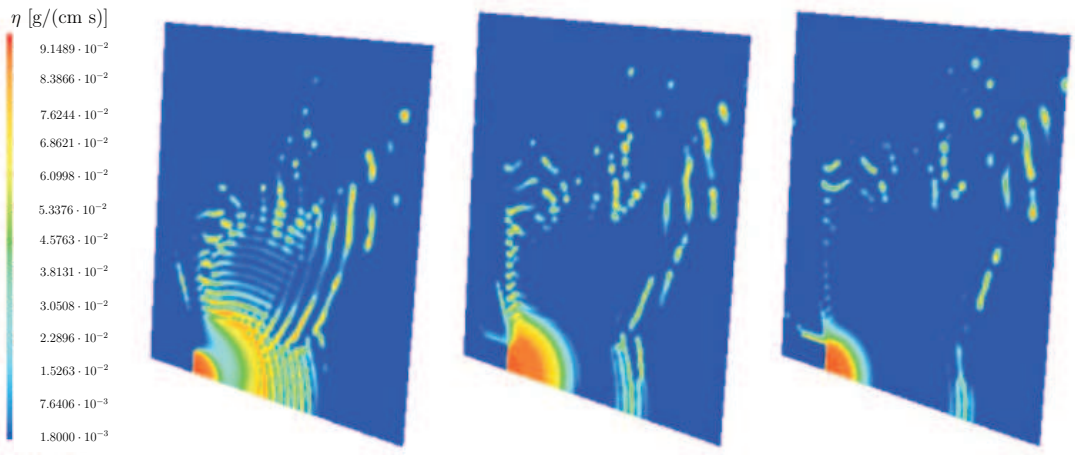

Figure C.1.: Contour plots of viscosity with respect to the distance r from the nozzle's center.

List of Tables

List of Figures

Bibliography

AEA Technology GmbH 2001 *CFX 4.4 User Guide*. AEA Technology.

Akima, H. 1972 *Algorithm 474: Bivarite interpolation and smooth surace fitting local procedures*. U.S. Department of Commerce.

Andersen, A. 1996 Feinzerstäubung von Metallschmelzen mittels Ultraschall-Stehwellen-Zerstäubung am Beispiel von Zinn. PhD thesis, University of Bremen.

Andersen, O., Bauckhage, K. & Schreckenberger, P. 1995 Production of fine metal powders by ultrasonic standing wave atomizers. *Int. J. of Powder Tech.* **31** (5), 341–349.

Anilkumar, A. V., Lee, C. P. & Wang, T. G. 1993 Stability of an acoustically levitated and flattened drop: An experimental study. *Phys. Fluids* **5** (11), 2763–2774.

Arsenin, V. Y. 1968 *Basic equations and special functions of mathematial physics*. London: ILIEFFE Books Ltd.

Bachalo, W. D. 2000 Spray diagnostics for the twenty-first century. *Atomization and Spray* **10**, 439–474.

Basaran, O. A. 1992 Nonlinear oscillation of viscous liquid drops. *J. Fluid Mech.* **241**, 169.

Bauckhage, K. 1992 Das Zerstäuben metallischer Schmelzen. *Chem. Ing.-Tech.* **64** (4), 322–332.

Bauckhage, K., Andersen, O., Hansmann, W., Reich, W. & Schreckenberger, P. 1996 Production of fine powders by ultrasonic standing wave atomization. *Powder Technology* **86**, 77–86.

Bauckhage, K. & Schreckenberg, P. 1994 Erzeugung von Pulvern durch Zerstäubung und Schnellabschreckung von Schmelzen mittels Ultraschall - Teil 1. Aufbau und Funktion der USZ. *Härterei-Technische Mitteilungen* **50** (4), 331–339.

Bauckhage, K., Schreckenberg, P. & Uhlenwinkel, V. 1995 Erzeugung von Pulvern durch Zerstäubung und Schnellabschreckung von Schmelzen mittels Ultraschall - Teil 2. Aufbau und Funktion der USZ. *Härterei-Technische Mitteilungen* **50** (4), 245–253.

Bauckhage, K., Schreckenberger, P. & Vetters, H. 1989 Verfahren zum Zerstäuben von flüssigen und festen Stoffen, vorzugsweise geschmolzenes Metall. *Deutsche Patentschrift DE 3939178 A1, Branson Ultraschall* .

Becker, E., Hiller, W. J. & Kowalewski, T. A. 1991 Experimental and theoretical investigation of large-amplitudeoscillations of liquid drops. *J. of Fluid Mech.* **231**, 189–210.

Becker, E., Hiller, W. J. & Kowalewski, T. A. 1994 Nonlinear dynamics of viscous droplets. *J. of Fluid Mech.* **258**, 191.

Bell, J. B., Colellla, P. & Glaz, H. M. 1989 A second-order projection method for the incompressible Navier-Stokes equation. *J. of Comp. Phys.* **85**, 257–283.

Bending, L. 1988 New developements of ultrasonic atomizers. *Proc. of the 4th Int Conf of Liquid Atomization and Spray System (ILASS)* **2-3**, 133–138.

Bond, W. N. 1935 In *Phys. Soc. London*, *4*, vol. 47, pp. 549–558.

Bothe, D. 2002 *Lecture notes: Computational fluid dynamics. Modellierung und Anwendung*. University of Paderborn, Chemical Engineering.

Brackbill, J. W., Kothe, D. B. & Zemach, C. 1992 A continuum method for modelling surface tension. *J. Comp. Phys.* **100**, 335–354.

Broch, J. T. 1990 *Principles of experimental frequency analysis*. Elsevier Applied Sciences.

Corbeels, P. L., Senser, D. W. & Lefebvre, A. H. 1992 Atomization characteristics of a high-speed rotary-bell paint applicator. *Atomization and Spray* **2**, 87–99.

Danilov, S. D. & Mironov, M. A. 1992 Breakup of a droplet in a high intensity sound field. *J. Acoust. Soc. Am.* **92** (5), 2747–2755.

Dombrowsi, N., Hasson, D. & Ward, D. E. 1960 *Chem. Eng. Sci.* **12**, 35–50.

Ferziger, J. H. & Peric, M. 2002 *Computational Method for Fluid Dynamics*. Springer Verlag.

Floryan, J. M. & Rasmussen, H. 1989 Numerical method for viscous flows with moving boundaries. *Appl. Mech. Rev.* .

Fluent Inc. 2000 *Fluent Post Processor*, flpost 1.2.6 edn. Fluent Deutschland GmbH.

Fluent Inc. 2003 *FLUENT 6 User Guide*. Fluent Deutschland GmbH.

Fraser, R. P., Eisenklamm, P., Dombrowski, N. & Hasson, D. 1962 *AJChE J.* (8), 672–680.

Frauenhofer, J. 1817 Bestimmung des Brechungs- und Farbstreuungsvermögens verschiedener Glasarten. *Gilberts Annalen der Physik* **56**, 193–226.

Gazka, M. 1994 Formeinfluß der Sonotroden auf die gemessenen Schallwechseldrücke bei der Erzeugung eines stehenden Ultraschallfeldes. *Tech. Rep.*. University of Bremen, studienarbeit.

Giesshammer, G. & Lierke, C. P. 1968 Metallpulvergewinnung durch Ultraschallzerstäubung metallischer Schmelzen. *VDI-Zeitschrift* **110** (9), 343–348.

Goldschmidt, A., Hohmann, G., Bauckhage, K. & Schreckenberger, P. 1993 Verfahren zum Beschichten von Werkstücken mit organischen Beschichtungsstoffen. *Deutsche Patentschrift DE 4328088 A1* .

Goldschmidt, A., Reiter, J. & Mattern, R. 1998 Einsatz der Ultraschall-Stehwellen-Zerstäubung in der Pulver-Lackiertechnik. *DFO e.V. Tagungsband Pulverlackpraxis* .

Griebel, M., Dornseifer, T. & Neunhoeffer, T. 1995 *Numerische Simulation in der Strömungsmechanik: Eine praxisorientierte Einführung*. Vieweg Verlag.

Hansmann, S. 1996 Einfluss von stoff- und betriebsparametern auf die Zerstäubung hochviskoser Flüssigkeiten im Ulraschall-Stehwellenfeld. PhD thesis, University of Bremen.

Harlow, F. H. & Welch, J. F. 1965 Numerical calculation fo time-dependent viscous incompressible flow of fluid with free surface. *Phys. Fluids* **8**, 2182.

Hennig, C. & Hemsel, T. 2004 Herstellung von Pulerlack durch Ultraschall: Interdisziplinärer Ansatz zur technologischen Optimierung der Stehwellenzerstäubung. *Tech. Rep.*. University of Paderborn.

Heuer, M. & Leschonski, K. 1985 Results obtained with a new instrument for the measurement of particle size distribution from diffraction patterns. *Part. Charact.* **2**, 7–13.

Hewitt, A. J. 1993 Droplet size spectra produced by air-assisted atomizers. *J. Aerosol Sci.* **24** (2), 155–162.

Heywang, Treiber, Herberg & Neft 1992 *Physik für Fachhochschulen und Technische Berufe*, 30th edn. Verlag Handwerk und Technik GmbH.

Hinze, J. O. 1955 Fundamentals of the hydrdynamic machanism of splitting in dispersion processes. *AIChE Jl* **1**, 227–239.

Hirt, C. W. & Nicols, B. D. 1981 Volume of Fluid (VOF) method for the dynamics of free boundaries. *J. Comp. Phys.* **39**, 201–225.

Hohmann, M., Jönsonn, G. & Lierke, E. G. 1988 *Metal Powder Producition by Ultrasonic Capilary or Standing Wave Technique*, *Modern Developement in Powder Metallurgy*, vol. 20, pp. 159–167.

Holmann, G. 1994 Beschreibung und Beeinflussung der Filmbildung von Pulverlacken durch chemische und verfahrenstechnische Massnahmen. PhD thesis, University of Paderborn.

Hsiang, L.-P. & Faeth, G. M. 1992 Near-limit drop deformation and secondary breakup. *J. of Multiphase Flow* **18** (5), 635–652.

Hyman, J. M. 1984 Numerical method for tracking interfaces. *Physica D* **120**, 396.

Ishii, M. 1975 *Thermo-Fluid Dynamic Theory of Two-Phase Flow*. Eyrolles, Paris.

Jacqmin, D. 1996 An energy approach to the continuum surface tension method. *AIAA paper 96-0858, 34th Aerospace Science Meeting and Exhibit* .

Jamet, D., Torres, D. & Brackbill, J. U. 2002 On the theorie and computation of surface tension: The elemination of parasitic currents through energy conservation in the second-gradient method. *J. Comput. Phys.* **182**, 262–276.

Kneubühl, F. K. & Sigrist, M. W. 1991 *Laser*. Stuttgart: B. G. Teubner.

Koebe, M. 2004 PhD thesis, University of Paderborn.

Kothe, D. B. & Mjolsness, R. C. 1992 RIPPLE: A new method for incompressible flows with free surface. *AIAA Journal* **30** (11), 2694–2700.

Lafaurie, B., Nardone, C. N., Scardovelli, S., Zaleski, S. & Zanetti, G. 1994 Modelling merging and fragmentation in multiphase flows with SURFER. *J. Comp. Phys.* **113**, 134–147.

Lamb, H. 1932 *Hydrodynamics*, 6th edn. Cambridge University Press.

Landau, J. D. & Lifshitz, E. M. 1959 *Fluid Mechnics*. New York: Pergamon.

Lang, R. J. 1962 Ultrasonic atomization of liquids. *J. Acoust. Soc. Am* **34** (1), 6–8.

Laskey, K. J., Oran, E. S. & Boris, J. P. 1987 Approaches to resolving and tracking interfaces and discontinuities. *Tech. Rep.*. Naval Research Laboratory Report, Arlington, VA.

Lee, C. P., Anilkumar, A. V. & Wang, T. G. 1991 Static shape and instability of an acoustically levitated liquid drop. *Phys. Fluids* **3** (11), 2497–2515.

Lee, C. P., Anilkumar, A. V. & Wang, T. G. 1994 Static shape and instability of an acoustically levitated drop with wave-drop interaction. *Phys. Fluids* **6** (11), 3554–3566.

Lee, C. P. & Wang, T. 1989 Near-boundary streaming around a small sphere due to two orthogonal standing waves. *J. Acoust. Soc. Am.* **86** (3), 1081–1088.

Lee, C. P. & Wang, T. G. 1990 Outer acoustic streaming. *J. Acoust. Am.* **88** (5), 2367–2375.

Lefebvre, A. H. 1989 *Atomization and Sprays*. New York, Hemisphere.

Li, Z. 1996 Der Beitrag von Schallwellendruck und Schallschnelle zur Fluid-Zerstäubung im Stehwellenfeld des Ultraschalls. PhD thesis, University of Bremen.

Lierke, E. G. 1995 Akustische, aerodynamische und elektrostatische Positionierung. *Forsch. Ing. Wes* **61** (7/8), 201 ff.

Lierke, E. G. 1996 Akustische Positionierung - Ein umfassender Überblick über Grundlagen und Anwendungen. *Acta Acoustica* **82** (3), 220–237.

Lierke, E. G. 1998 Techniken und Anwendungen der Ultaschall-Zerstäubung - Ein Rückblick auf 35 Jahre Forschung und Entwicklung. *CIT* **7**, 815–826.

Lierke, E. G. & Grossbach, R. 1983 Acoustic positioner for mirror furnace. *Tech. Rep.* Contract No. 4494080. ETEC.

Lierke, E. G., Grossbach, R. & Flögel, K. 1980 Verfahren und Vorrichtung zum Zerstäuben von Flüssigkeiten, Suspensionen und Emulsionen, agglomierten Stäuben bzw. Pulvern sowie Mischungen. *Deutsche Offenlegungsschrift* (2842232).

Lierke, E. G., Grossbach, R. & Flögel, K. 1978 Verfahren und Vorrichtung zum Zerstäuben von Flüssigkeiten, Suspensionen und Emulsionen, agglomerierten Stäuben bzw. pulvern sowie mischungen derselben. *Deutsche Patentschrift DE 2842232 C2, Batelle-Inst. e.V.* .

Lierke, E. G., Lümhann, K., Jönsson, S., Hohmann, M., Bendig, L., Hofmann, F. & Gaa, F. 1987 Vorrichtung zum Zerstäuben eines flüssigen Mediums mit Hilfe von Ultraschall. *Deutsche Patentschrift DE 3732325 A1, Batelle-Inst. e.V.* .

Lierke, E. G. & Ruckdeschel, E. W. 1976 "verfahren und vorrichtung zur herstellung von pulvern oder granulaten aus metallen und legierungen". *Deutsche Patentschrift DE 2656330 C2, Batelle-Inst. e.V.* .

Lock, N., Jaeger, M., Medale, M. & Occelli, R. 1998 Local mesh adaption technique for front tracking problems. *Int. J. Numer. Meth. Fluids* **28**, 719–736.

Mattern, R. 1998 Chemische und Verfahrenstechnische Maßnahmen zur Verbesserung des optischen Eigenschaftsprofils von Pulverlacken. PhD thesis, University of Paderborn.

Meier, M., Yadigaroglu, G. & Smith 2000 A novel technique for including surface tension in PLIC VOF methods .

Meng, R. 1997 Untersuchung zum Wärmeübergang in unterschiedlichen Konfigurationen von Ultraschallfeldern, u.a. zur Zerstäubung metallischer Schmelzen. PhD thesis, University of Bremen.

Meyer, E. & Neumann, E. G. 1979 *Physikalische und Technische Akustik*. Braunschweig: Vieweg.

Motzigemba, M., Roth, N., Bothe, D., Warnecke, H.-J., Prüss, J., Wielage, K. & Weigand, B. 2002 The effect of non-newtonian flow behaviour on binary droplet collision: VOF-simulation and experimental analysis. *In Proc. 18th Annual Conf. Liquid Atomization and Spray Systems ILASS-Europe'02* pp. 559–564.

Murray, I. F. & Heister, S. D. 1999 On a droplet response to acoustic exitation. *Int. J. Mult. Flow* **25**, 531–550.

Noh, W. F. & Woodward, P. 1976 ŚLIC simple line interface construction: In *Lecture notes in physics* (ed. van der Vooren & P. J. Zandbergen), pp. 330–340. Spinger Verlag.

Osher, S. & Sethian, J. A. 1988 Fronts propagating with curvature dependent speed: algorithms based on Hamilton-Jacobi formulations. *J. Comp. Phys.* **79**, 12.

Patankar, V. S. 1980 *Numerical heat transfer and fluid flow*. New York, USA: McGraw Hill.

Pohlmann, R. & Stamm, K. 1965 *Untersuchungen zum Mechanismus der Ultraschall-Vernebelung an Flüssigkeitsoberflächen im Hinblick auf technische Anwendungen*. Westdeutscher Verlag Köln/Opladen, forschungsbericht des Landes NRW.

Puckett, E. G., Almgren, A. S., Bell, J. B., , Marcus, D. L. & Rider, W. J. 1997 A high-order projection method for tracking fluid interfaces in variable density incompressible flows. *J. Comp. Phys.* **130**, 269–282.

Rawshaw, J. D. & Trapp, J. A. 1976 A numerical technique for low-speed homogenous two-phase flow with sharp interfaces. *J. Comp. Phys.* **21**, 438.

Rayleigh, J. W. S. 1879*a* On the capillary phenomena of jets. *Proc. R. Soc. London* **29**, 71–97.

Rayleigh, J. W. S. 1879*b* On the instability of jets. *Proc. London Math. Soc.* **10**, 4–13.

Reich, W. 1995 Die Ultraschall-Stehwellen-Zerstäubung als kontinuierliches Disintegrationsverfahren für die Feinstpulvererzeugung aus Glasschmelzen. PhD thesis, University of Aachen.

Reipschläger, O. 2002 Desintegration von Fluiden im Ultraschallfeld: Modellierung, Simulation, Experiment. PhD thesis, University of Paderborn, Germany.

Reipschläger, O., Bothe, D., Broeker, H.-C., Monien, B., Prüss, J., Warnecke, H.-J. & Weigand, N. 2001 Modellierung und Simulation zur Optimierung des Zerstäubungsprozesses in einem Ultraschall-Stehwellenfeld. *ASIM Fortschrittsberichte Simulation* (15. Symposium), 563–568.

Reipschläger, O., Bothe, D., Monien, B., Prüss, J., Weigand, B. & Warnecke, H.-J. 2002 Modelling and simulation of the disintegration process

in ultrasonic standing wave atomizers. *In Proc. of 18th Annual Conf. on Liquid Atomization and Spray Systems, ILASS-Europe'02* pp. 449–454.

Reitz, R. D. & Bracco, F. V. 1982 Mechanism of atomization of a liquid jet. *Phys. Fluids* **25** (10), 1730–1742.

Rider, W., Kothe, D. B., Mosso, S. J. & Cerutti, J. H. 1995 Accurate solution algorithms for incompressible multiphase flows. *In Proc. of 33rd Aerospace Meeting and Exhibit* .

Rider, W. J. & Kothe, D. B. 1998 Reconstructing volume tracking. *J. Comp. Phys.* **141**, 112–152.

Rieber, A. 2004 Numerische Modellierung der Dynamik freier Phasengrenzflächen in Zweiphasen Strömungen. PhD thesis, University of Stuttgart, Germany.

Rieber, A. & Frohn, A. 1999 A numerical study on the mechanism of splashing. *Int. J. Heat and Fluid Flow* **20**, 455–461.

Rieber, M. & Frohn, A. 1997 Navier-Stokes simulation of droplet collision dynamics . *Proc. of 7th Int. Symp. on Computational Fluid Dynamics* .

Rieber, M. & Frohn, A. 1998 Numerical simulation of splashing drops. *Proc. of 14th Int. Conf. on Liquid Atomization and Sprays* .

Rieber, M., Graf, F., Hase, M., Roth, N. & Weigand, B. 2000 Numerical simulation of moving spherical and deformed droplets. *Proc. of ILASS-Europa 2000* .

Rosin, R. & Rammler, E. 1933 The laws governing the fineness of powder coal. *J. Inst. Fuel* **7**, 29–36.

Rudman, M. 1998 A volume-tracking method for incompressible multi-fluid flows with large density variations. *Int. J. Numer. Meth. Fluids* **28**, 357–378.

Scardovelli, R. & Zaleski, S. 1999 Direct numerical simulation of free-surface and interfacial flow. *Annu. Rev. Fluid Mech.* **31**, 567–603.

Schädlich, S. 2001 Untersuchung von Schallfeldkenngrößen bei der Ultraschall-Stehwellenzerstäubung unter Berücksichtigung der Differenz in der Eigenfrequenz der Schallquellen. *Tech. Rep.*. University of Bremen, studienarbeit.

Schmehl, R., Maier, G. & Wittig, S. 2000 CFD analysis of fuel atomization, secondary droplet breakup and spray dispersion in the premix duct of a LPP combustor. *In Proc. of 8th Int. Conf. on Liquid Atomization and Spray Systems, Pasadena, CA, USA* .

Scholz, T. 1998 *Experimentelle Untersuchungen zur Mehrphasenströmung im Sprükegel eines elektrostatisch unterstützten Hochrotationszerstäubers*, nr. 346 edn., *Reihe 7*, vol. VDI-Fortschrittsberichte. Düsseldorf: VDI-Verlag.

Schreckenberg, P. 1991 Wirkungsweisen unterschiedlicher Ultaschall-Stehwellen-Zerstäuber. *IWT-Bericht* **91/1**.

Silhavy, M. 1997 *The Mechanics and Thermodynamics of Continuous Media*. Springer Verlag, Berlin/Heidelberg.

Slattery, M. 1999 *Advanced Transport Phenomena*. Cambridge University Press, Cambridge.

Squire, H. B. 1953 *Br. J. Appl. Phys.* **4**, 167–169.

Stamm, H. & Purzel, R. 1984 *Elektronische Meßverfahren*. VEB Verlag Technik, Berlin.

Sutilov, V. A. 1984 *Physik des Ultraschalls*. Springer Verlag, Wien, New York.

Tau, E. Y. 1994 A second - order projection method for the incompressible Navier-Stokes equations in arbitrary domains. *J. Comp. Phys.* **115**, 147–152.

Tayler, G. J. 1959 In *Phys. Soc. London*, *A*, vol. 253, pp. 313–321.

Trinh, E. H. 1986 Measurement of physical properties of materials using acoustic levitation. *Tech. Rep.* 112 (A). 115th TMS Annual Meeting.

Trinh, E. H. & Wang, T. G. 1982 Large amplitude free and driven drop-shape oscillations: experimental observations. *J. Fluid Mech.* **122**, 315–288.

Truggvason, G., Bunner, B., Ebrat, O. & Tauber, W. 2001 A front-tracking method for the computations of multiphase flow. *J. Comput. Phys.* **169**, 708–759.

Tsamopoulus, J. A. & Brown, R. A. 1983 Nonlinear oscillation of inviscid drops and bubbles. *J. Fluid Mech.* **127**, 519–537.

Versteeg, H. K. & Malalasekera, W. 1995 *An Introduction to Computational Fluid Dynamics: The Finite Volume Method*. Reading, MA: Adison-Wesley.

Vestweber, J. 1999 Untersuchung des Filmbildeverhaltens mittels Ultraschallstehwellenzerstäubung hergestellter Pulverlacke. Master's thesis, University of Paderborn, Germany.

Vestweber, J. 2004 Einsatzmöglichkeiten der Ultraschallstehwellenzerstäubung in der Lackiertechnik - Vergleich der Tropfengrößenverteilungen mit pneumatischer- hydraulischer- und Hochrotationszerstäubung. PhD thesis, University of Paderborn.

Walzel, P. 1990 Zerstäuben von Flüssigkeiten. *Chem. Ing. Tech* **62** (12), 983–994.

Welch, J. E., Harlow, F. H., Shannon, J. P. & Daly, B. J. 1966 The MAC method: a computing technique for solving viscous, incompressible, transient fluid-flow problems involving free surfaces. *Tech. Rep.* LA-3425. Los Alamos Scientific Laboratory Report.

Wesseling, P. 1992 *An Introduction to Multigrid Methods*. Chichester: John Wiley & Sons.

Yarin, A. L., Brenn, G., Kastner, O., Rensink, D. & Tropea, C. 1999 Evaporation of acoustically levitated droplets. *J. Fluid Mech.* **399**, 151–204.

Yarin, A. L., Pfaffenlehner, M. & Tropea, C. 1998 On acoustic levitation of droplets. *J. Fluid Mech.* **356** (65), 65–91.

Youngs, D. L. 1992 Time-dependent multi-material flow with large distortion. *Numerical Methods for Fluid Dynamics* pp. 273–285.

Yule, A. J. & Dunkley, J. J. 1994 *Atomization of Melts*. Oxford, Clarendon Press.